

# Vectorial Physical-Optics Modeling of Microscopy Systems

with Inclusion of Micro-/Nano-Structures

*A dissertation submitted for the academic title*

**Doktor Rerum Naturalium (Dr. rer. nat.)**

*Author:*

**M.Sc. Rui Shi**

Institute of Applied Physics

Friedrich-Schiller-Universität Jena



*Supervisor:*

Prof. Dr. rer. nat. habil. Frank Wyrowski

*Submitted to:*

**the Council of the Faculty of Physics and Astronomy  
of Friedrich-Schiller-Universität Jena**

**Supervisor:** Prof. Dr. Frank Wyrowski, Friedrich-Schiller-Universität Jena

**Reviewer:** Prof. Dr. Alois Herkommer, Universität Stuttgart

**Reviewer:** Prof. Dr. Jürgen Jahns, FernUniversität in Hagen

**Date of the Disputation:** 23rd February 2021

**Dissertation, Friedrich-Schiller-Universität Jena, 2021**

## ABSTRACT

---

Optical microscopy is one of the most important techniques for modern science. As the microscopy technology has developed in recent decades, the microscopy system becomes more and more complex. The accuracy of the results obtained by the microscopy systems is more easily to be influenced by the imperfections of the system in the real-life experiment. Therefore, the modeling and analysis of the complex microscopy systems in details, like the tolerance of the misalignment of the lenses, are on demand to improve the research efficiency. The widely used modeling technique: ray tracing, is limited by the absence of various optical effects, e.g. the diffraction, polarization, coherence, etc. Therefore, the vectorial physical-optics modeling of the microscopy system was proposed and developed. However, it was restricted to aplanatic lens models, or to the presumed aberrations. The vectorial physical-optics modeling of the microscopy system based on the real lens has not been investigated in the literature to the best of the author's knowledge. Furthermore, the modeling of the real-lens-based system with inclusion of the micro-/nano-structures has also not been investigated.

In this work, the author does the vectorial physical-optics modeling of microscopy systems with inclusion of the micro-/nano-structures in the framework of field tracing. The full modeling techniques are formulated by the connection of different solvers of Maxwell's equations, e.g. solvers for the lenses and solvers for the micro-/nano-structures. The accuracy and limitations of these solvers are investigated in details. Then, three types of microscopy systems are modeled and analyzed: 1) a system of focusing through a micro-/nano-particle, 2) a Fourier microscopy system, 3) a microscopy system with the structured illumination.

Besides microscopy systems, the modeling techniques in this work by the connection of different solvers can also be applied for other systems which consist of both lens systems and micro-/nano-structures, e.g. grating based lightguide for augmented reality, dots projection system with diffractive optical element for face identity, diffractive optical element based LiDAR system for autonomous driving, etc.





## ABSTRACT

---

This page is left blank intentionally.



## ZUSAMMENFASSUNG

---

Die optische Mikroskopie ist eine der wichtigsten Techniken für die moderne Wissenschaft. Mit dem Voranschreiten der Technologie in den letzten Jahrzehnten sind die Aufbauten der Mikroskope immer komplexer geworden. Die Genauigkeit der Ergebnisse, die sich aus diesen Aufbauten ergeben, wird deswegen mehr von den Ungenauigkeiten des Aufbaus im Experiment beeinflusst als zuvor. Aus diesem Grund ist die Modellierung und Analyse des komplexen mikroskopischen Aufbaus in all seinen Details, wie z. B. die Toleranz der Verschiebung der Linsen, ein aufkommendes Thema, um die Effizienz der Forschung zu verbessern. Die bisher weit verbreitete Simulationstechnik des „Ray Tracings“ hat Limitationen in verschiedenen Bereichen, z. B. sind Diffraktion, Polarisierungseffekte und Kohärenz nicht inkludiert. Deswegen wurde eine auf der vektoriellen, physikalischen Optik basierende Technik vorgeschlagen und entwickelt. Allerdings war diese auf die Modellierung von aplanatischen Linsen, welche Abbes Sinusbedingung erfüllten, oder auf die Annahme von Aberrationen beschränkt. Die vektorielle, physikalisch-optische Modellierung von Mikroskopen basierend auf realen Linsen wurde bisher - nach besten Wissen und Gewissen des Autors – noch nicht in der Literatur untersucht. Weiterhin wurde auch die Modellierung von Aufbauten mit realen Linsen und der Inklusion von Mikro/Nano-Strukturen bisher noch nicht untersucht.

In dieser Arbeit stellt der Autor ein Verfahren vor, dass die Modellierung basierend auf der vektoriellen, physikalischen Optik mit Inklusion von Mikro/Nano-Strukturen im Rahmen des „Field Tracings“ ermöglicht. Die Modellierungstechnik ist formuliert durch die Verbindung von verschiedenen Lösungsalgorithmen der Maxwell-Gleichungen, z. B. Lösungen für die Linsen oder die Mikro/Nano-Strukturen. Die Genauigkeit und Limitationen dieser Lösungsalgorithmen sind vollständig untersucht. Anschließend wurden drei Arten von mikroskopischen Aufbauten untersucht und analysiert: 1) Aufbau mit Fokussierung durch eine Mikro/Nano-Struktur 2) Fourier-Mikroskop 3) Mikroskop mit strukturierter Illumination.

Neben mikroskopischen Aufbauten kann die Modellierungstechnik des „Field Tracings“, die in dieser Arbeit verwendet wird, auch für andere Systeme, wie z. B. „Augmented Reality“ – Systeme basierend auf Lightguides mit Gratings, „Dot Projection“ – Systeme mit diffraktiven optischen Elementen zur Gesichtserkennung, auf diffraktiven optischen Elementen basierende LIDAR – System für automatisiertes Fahren und viele weitere Anwendungen genutzt werden.

## CONTENTS

---

1	INTRODUCTION	3
1.1	Background	3
1.1.1	Basic principle of microscopy systems	3
1.1.2	Application areas of microscopy systems	3
1.1.3	Selected applications	6
1.2	Problem statement	6
1.2.1	Motivation for modeling of microscopy systems	6
1.2.2	Current modeling techniques and limitations	7
1.2.3	Aim of this thesis	8
1.3	Structure of the thesis	8
2	THEORY	9
2.1	Field tracing concept	9
2.1.1	Vectorial fields	9
2.1.2	Source models	12
2.1.3	Operator for free space	13
2.1.4	Operators for components	13
2.1.5	Fourier transforms	15
2.1.6	Measured quantities	15
2.2	Operator for curved surfaces	17
2.2.1	Introduction	17
2.2.2	Problem statement	18
2.2.3	Coordinate transformation on curved surface	19
2.2.4	Local boundary condition on curved surface	22
2.3	Operator for micro-/nano-structures	26
2.3.1	Introduction	26
2.3.2	Periodic structure by Fourier modal method	28
2.3.3	Aperiodic structure by Fourier modal method	35
2.4	Summary and conclusion	38
3	EVALUATION OF THE OPERATORS FOR COMPONENTS	39
3.1	Introduction	39
3.2	Operator for curved surfaces	41
3.2.1	Real curved surface	41
3.2.2	Fictitious curved surface	50
3.3	Operator for micro-/nano-structures	52
3.3.1	Periodic structure	52
3.3.2	Aperiodic structure	53
3.4	Summary and conclusion	55
4	MODELING OF FOCUSING THROUGH A MICRO-/NANO-PARTICLE	57
4.1	Introduction	57
4.2	Modeling tasks and techniques	58

4.3	Focusing by ideal lens through a micro-/nano-particle . . . . .	60
4.3.1	Focusing only by ideal lens system . . . . .	60
4.3.2	Focusing through a micro-/nano-particle . . . . .	61
4.4	Focusing by real lens through a micro-/nano-particle . . . . .	65
4.4.1	Focusing only by real lens system . . . . .	65
4.4.2	Focusing through a micro-/nano-particle . . . . .	68
4.5	Summary and conclusion . . . . .	68
5	MODELING OF FOURIER MICROSCOPY SYSTEMS . . . . .	71
5.1	Introduction . . . . .	71
5.2	Modeling tasks and techniques . . . . .	72
5.3	Emission diagram of a single molecule . . . . .	74
5.3.1	Without lens vs. ideal lens vs. real lens . . . . .	75
5.3.2	Performance of different real lenses . . . . .	77
5.3.3	Propagation through photonic crystal . . . . .	78
5.4	Angular-spectral analysis of photonic crystal . . . . .	80
5.4.1	Fourier microscope . . . . .	82
5.4.2	Fourier microscope and spectrometer . . . . .	83
5.4.3	Entire system . . . . .	83
5.5	Summary and conclusion . . . . .	84
6	MODELING OF STRUCTURED ILLUMINATION MICROSCOPY . . . . .	87
6.1	Introduction . . . . .	87
6.2	Modeling tasks and techniques . . . . .	88
6.3	One photon and two dimensional . . . . .	90
6.3.1	Polarization . . . . .	90
6.3.2	Diffraction . . . . .	91
6.3.3	Inclined incidence . . . . .	92
6.4	Two photon and three dimensional . . . . .	93
6.4.1	Spatial distribution . . . . .	93
6.4.2	Temporal distribution . . . . .	94
6.5	Summary and conclusion . . . . .	96
7	CONCLUSION AND OUTLOOK . . . . .	97
	BIBLIOGRAPHY . . . . .	103

## INTRODUCTION

---

### 1.1 BACKGROUND

#### 1.1.1 Basic principle of microscopy systems

Optical microscopy is one of the most important techniques for modern science. In principle, optical microscopy systems are applied to have the structural information of the micro-/nano-samples using light, by a detector or via a detector plus post computing. The samples are generally acknowledged to be not self-luminous, or otherwise their luminance is very weak. Therefore, in order to carry the structural information to the detector, the illumination is needed. The basic work flow of optical microscopy, as shown in Fig. 1, is interpreted as: 1) illuminating the sample, 2) collecting the scattered or emitted light from the sample, 3) detecting the light or detecting the light and doing post computing.

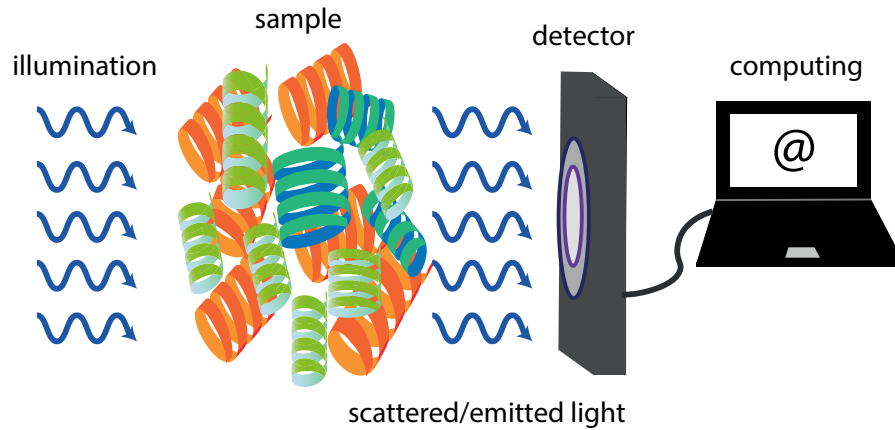


Figure 1: Illustration of the basic principle of an optical microscopy system.

#### 1.1.2 Application areas of microscopy systems

Based on the basic principle, optical microscopy systems are very often applied in scientific research, especially in material science and life science.

##### 1.1.2.1 Material science

In material science, the structural information of the sample is well modeled by the permittivity of the sample as:  $\Omega \propto \epsilon$ , where  $\Omega$  represents the structural information and

$\epsilon$  denotes the permittivity of the sample. The interaction of the illumination light with the sample is governed by Maxwell's equations. The information of the permittivity  $\epsilon$  is encoded in the scattered light, which is carried to the detector as indicated in Fig 1. High resolution is always a high demand in optical microscopy. According to Abbe's theory [1], the oblique incidence is used to achieve higher resolution compared to normal incidence. The high Numerical Aperture (NA) condenser lenses, e.g. oil, water, or solid immersion condenser [2], are also preferred to achieve high resolution [3]. Following the same principle for high resolution, confocal scanning microscopy [4–6] is widely used which applies a tightly focused field for the illumination. The tighter focused field used for illumination can be achieved by focusing the radially polarized field [7–9]. It can also be achieved by a dielectric microsphere [10, 11] which is often referred to as microsphere-based microscopy [12–14]. Another way to achieve high-NA illumination is to use the emitted light of the fluorescent molecule, which is referred to as ultra-thin condenser lens [15]. The near field scanning microscopy uses a tip on the surface of the sample [16, 17] to provide very tiny illumination spot. Therefore, the resolution is improved.

Besides the illumination, the collection of the light to the detector is also important. According to Abbe's theory [1], high-NA objective is needed, e.g. oil, water or solid immersion objectives [2, 18]. Furthermore, in order to achieve even higher resolution, a tip is applied to collect the evanescent wave in the near field which contains high spatial-frequency information [16, 17]. Another method is that a microsphere is used to collect the evanescent wave by transferring it into propagating wave to the detector [12–14].

In addition to the high resolution, the high contrast is also demanded to obtain clear image. Phase-contrast microscopy decodes the structural information which is encoded in the phase to the amplitude [19, 20]. Differential Interference Contrast (DIC) microscopy [21, 22] visualizes the derivative of the optical phase of the sample to improve contrast. Dark-field microscopy avoids the incident light from being collected by the objective lens [23]. Another demand is to have a high signal-to-noise ratio. It means the background noise, e.g. the out-of-focus light, should be as little as possible. The confocal microscopy applies a pinhole to block the out-of-focus light in order to achieve a high signal-to-noise ratio.

In recently years, the visualization of the spatial-frequency distribution of the electric field is on demand. Therefore, Fourier microscopy, which is also referred to back focal plane imaging, is proposed to achieve this demand [24–26]. Furthermore, in recent years, as the development of micro-/nano-fabrication technology [27–30], the size of the microscope can be reduced to the level of microns which is integrated into the micro-systems [31, 32].

The image at the detector is sometimes indirect to what is desired. Therefore, post computing is needed to retrieve the structural information of the sample. The followings are some examples: Holographic microscopy retrieves the phase which encodes the structural information by post computing via the hologram on the detector [33]. The so-called Fourier ptychography uses Fourier transform in the post computing combined with oblique incidence to achieve wide field of view as well as high resolution [34]. The so-called Fourier imaging microscopy uses post computing to retrieve the period of a photonic crystal via the image at back focal plane [35].

### 1.1.2.2 Life science

In life science for certain cases, the structural information of the sample can be modeled by the permittivity of the sample as in material science:  $\Omega \propto \epsilon$ . All of the above mentioned microscopy types in material science are applicable to life science with the same working principle. Furthermore, in recent decades, fluorescence microscopy [33, 36, 37] is widely used in most of the cases in life science. In these situations, the structural information can be well-modeled by the position distribution of the fluorescent molecules attached to the sample:  $\Omega \propto M^{\text{pos}}$ , where  $M^{\text{pos}}$  represents the position of the fluorescent molecules. The interaction of the illumination light and the sample is governed by quantum optics. As a result, the illumination light excites the emitted light from the fluorescent molecules.

The size of the emitted light depends on the size of the illumination light. When the size of the illumination light is larger than the resolution capacity of the light collecting systems, it does not play a role for the resolution improvement. Therefore, it is relatively flexible. The oblique illumination has no effect on resolution improvement as it has, in the case of material science [38]. Nevertheless, when the size of the illumination light is smaller than the resolution capacity of the objective lens systems, the smaller size illumination improves the resolution. For example, in the case of scanning microscopy system [4], e.g. tightly focused radially polarized illumination [7–9], microsphere-based microscopy [10], tip-based near field microscopy [16], smaller lateral illumination size provides higher lateral resolution. Following the same logic, the SaTurated-Emission-Depletion (STED) microscopy [39] uses an effective smaller size of the illumination to improve the lateral resolution. It means that an additional stimulated emission illumination of doughnut shape is applied to inhibit the fluorescence process in the outer regions of the excitation illumination. The higher spatial-frequency information of the sample can be encoded in the lower spatial-frequency of the emitted light by structured illumination [40–42]. By combining with post computing, the higher spatial-frequency information of the sample can be decoded. Therefore, the resolution is improved. The so-called PhotoActivated Localization Microscopy (PALM), which is also referred to as STochastic Optical Reconstruction Microscopy (STORM) [43, 44], uses serial of illuminations. First, the illumination activates the photoactivatable fluorescent molecules randomly. Then the illumination excites the emitted light from the activated fluorescent molecules. After collecting and detecting the emitted light, the illumination bleaches the activated fluorescent molecules. And these serial illuminations repeat until enough number of the groups of emitted light is recorded. By combining the post computing, the localized positions of the fluorescent molecules are imposed to achieve the so-called super-resolution image.

In addition to the lateral resolution, the so-called  $4\pi$ -microscopy [45, 46] and light-sheet microscopy [47–49] improve the axial resolution by using a smaller size of illumination in axial direction. In order to achieve a deeper penetration of the illumination together with the reduction of the out-of-focus light, two-photon microscopy is often used [50–52].

On the contrary to the complex engineered illumination as mentioned above, the collection of the emitted light from the fluorescent molecules attached on the sample is



straightforward. In the case that the size of the illumination light is larger than the resolution capacity by the collecting system, the resolution of the collecting system determines the entire resolution which is explained by Rayleigh criterion [53].

### 1.1.3 *Selected applications*

As it is mentioned above, in both material science and life science, the tiny focal spot for illumination is essential for the resolution improvement. Therefore, it is worthy to investigate the generation of tiny focal spot in more details.

In material science, Fourier microscopy system is in high demand in recently years due to the fact that it makes direct observation of the spatial-frequency distribution possible, as the spatial-frequency distribution is essential in nanooptics. Therefore, detailed analysis of the Fourier microscopy system is desired.

In life science, STED and PALM/STORM are widely used to provide nano-scale resolution. STED needs high illumination power which is detrimental to living cell. PALM/STORM has a low speed which restricts the usages for imaging living cell. However, SIM can provide nano-scale resolution with low power illumination as well as relatively fast imaging speed. It is the best candidates for imaging living cells. Therefore, more detailed analysis of the SIM is desired.

## 1.2 PROBLEM STATEMENT

### 1.2.1 *Motivation for modeling of microscopy systems*

Most of the real-life experimental microscopy systems possess a complex configuration which includes several lenses, e.g. objective lens, tube lens, collimating lens, ect. In some cases, e.g. the above-mentioned three selected applications, micro-/nano-structures as samples or components are also included in. The detected signal are the superposition of the optical effects of the samples and of the components of the systems, e.g. lenses and gratings. In order to predict and guide the experiment in advance, the influence from the sample and from the components of the systems should be clearly investigated. Furthermore, building of many complex configurations takes heavy effort in the experiment. The position parameters and the tolerance of the misalignment of the lens system are essential to guide the building of the systems in real-life experiments. The optical modeling provides the feasibility. It is flexible to analyze the effects from the sample and from the components of the system. Therefore, it provides a detailed interpretation of the optical properties of the sample and of the optical systems. Based on the above arguments, it is concluded that modeling of the real complex microscopy systems is essential for advanced research on microscopy, as it helps to predict the experiment results and guide the real-life experiment in the sense of digital twin.

### 1.2.2 Current modeling techniques and limitations

#### 1.2.2.1 Ray Tracing Model

Since the importance of the modeling of the microscopy systems is aware of, researchers very often apply ray tracing to analyze the entire lens systems [54–59]. It is fast and all the aberrations from the lens systems are included, some tolerance effects of the misalignment are also revealed. It is available in several commercial software, e.g. Optic-Studio [60] or CODE V [61]. However, the polarization, the amplitude, the diffraction, the coherence of the electric fields and the effects of the micro-/nano-structure are not included. These effects are important in microscopy systems modeling. Therefore, the physical-optics modeling should be taken into account.

#### 1.2.2.2 Vectorial Physical-Optics Model

As in most of the microscopy systems, a high-NA objective lens is included, the vectorial effect of the light is of great importance. Furthermore, the vectorial effect also plays an important role when the micro-/nano-structure is included. Therefore, a vectorial physical-optics modeling of the entire system is desired.

In order to perform the vectorial physical-optics modeling of the high-NA lens system, an ideal lens, which is aplanatic, is very often assumed. Debye-Wolf integral [62–68] or with its fast implementation [69] is widely used to model the high-NA focusing systems with considering all the vectorial effects. By combination with the back focal plane imaging of a dipole source based on an aplanatic lens [24, 70], the image of a dipole source is studied [65, 66]. While combined with the plane interface or stratified media modeling, the focused field through a plane interface or stratified media is studied [71–77]. Some authors study the high-NA lens system by presuming a certain aberration from a lens system [78–81]. However, the aberration from the real lens system which is included in the ray tracing model, is not included in the vectorial physical-optics model.

In order to perform the vectorial physical-optics modeling of the micro-/nano-structure which is included in the microscopy system, the rigorous Maxwell's solvers, e.g. Finite Difference Time Domain (FDTD), Finite Element Method (FEM) are applied [12, 82–84]. But they are modeled separately from the whole system because of the high numerical effort. In [85], the authors apply FEM to simulate the whole system including all the lens system. But the system is assumed very small compared to the reality.

The concept to model the whole microscopy systems with inclusion of micro-/nano-structures is proposed by connection of different field solvers [66, 86, 87]. But the application of the concept is limited. In [88], the authors combine Debye-Wolf integral with a dipole approximation of the scattered field to model the image of a small scatterer. In [89], the authors combine Debye-Wolf integral with Mie theory to model the image of a finite sized gold sphere. In [90], the authors combine Debye-Wolf integral with FDTD to model the image of a microshell. In [91, 92], the authors combine Debye-Wolf integral with Method of Moment (MoM) to model to image of, e.g. an annular ring. In [10] the authors combine Debye-Wolf integral with FEM or FDTD to model to the focused field interaction with microsphere. However all these applications are based on an ideal lens

system without considering the influence of the real lens system.

### 1.2.3 *Aim of this thesis*

In this thesis, to the best of the author's knowledge, it is the first time that the vectorial physical-optics modeling of the entire microscopy system with the real lenses and with inclusion of micro-/nano-structure is performed. It is performed in the framework of field tracing [86, 87] by connecting different field solvers. By applying to the three selected applications, the important phenomena of the vectorial physical optics of the entire systems are investigated and analyzed.

## 1.3 STRUCTURE OF THE THESIS

The thesis is organized as follow: In chapter 2, the concept and techniques of the modeling a entire microscopy system are formulated in the framework of field tracing with the Bidirectional (B) operators as illustrated in Fig. 2. In chapter 3, the B operators for modeling the lens systems and the micro-/nano-structures are validated and evaluated numerically. In chapter 4, the modeling is applied to investigate and analyze the focusing through a micro-/nano-particle as illustrated in Fig. 32 and Fig. 33. In chapter 5, the modeling is applied to investigate and analyze the Fourier microscopy system as illustrated in Fig. 48 and Fig. 49. In chapter 6, the modeling is applied to investigate and analyze the microscopy system with structured illumination as illustrated in Fig. 60, Fig. 61 and Fig. 62. Chapter 7 concludes the thesis and gives an outlook.

## 2.1 FIELD TRACING CONCEPT

In order to do the vectorial physical-optics modeling of the microscopy systems, the vectorial fields need to propagate through the entire optical systems. Rigorous Maxwell's equations solvers, e.g. Finite Difference Time Domain (FDTD), Finite Element Method (FEM), Fourier Modal Method (FMM) are not practical due to the heavy numerical effort [93]. Therefore, in the field tracing concept, the entire optical system is tear into regions [86]. In each region, the customized Maxwell's equations solver is applied in different domains rigorously or approximately with high accuracy. Then the solutions of different regions are interconnected sequentially or non-sequentially [87]. By this manner the full modeling of the entire system is achieved with high accuracy and relatively fast speed.

In order to demonstrate the field tracing concept more clearly, a fictitious microscopy system with inclusion of micro-/nano-structures is taken for example as shown in Fig. 2 (a). The collimated laser beam illuminates the grating to generate diffraction orders. The  $\pm 1$  orders are collected by the first tube lens and focused by the first objective lens on a photonic crystal. The transmitted fields are collected by the second objective lens and then focused by the second tube lens at the image plane which is the focal plane of the second tube lens.

In this thesis of modeling of microscopy systems, the sequential connection of different optical components, e.g. lens system, micro-/nano-structures is assumed. Therefore, the whole procedure of modeling the entire microscopy system is presented by the field tracing diagram as shown in Fig. 2 (b).

### 2.1.1 Vectorial fields

Before starting the procedure of the modeling, it is clarified that the electromagnetic fields discussed in this thesis are fully vectorial and rigorously governed by Maxwell's equations in different domains.

#### 2.1.1.1 Space and time domain

The electromagnetic fields are written in space-time domain in Cartesian coordinates. In this thesis, the non-magnetizable material is assumed. And no free charges is assumed that the convective current density is zero. Therefore, the current density only contains the conductive current density which is a function of electric field. And no external

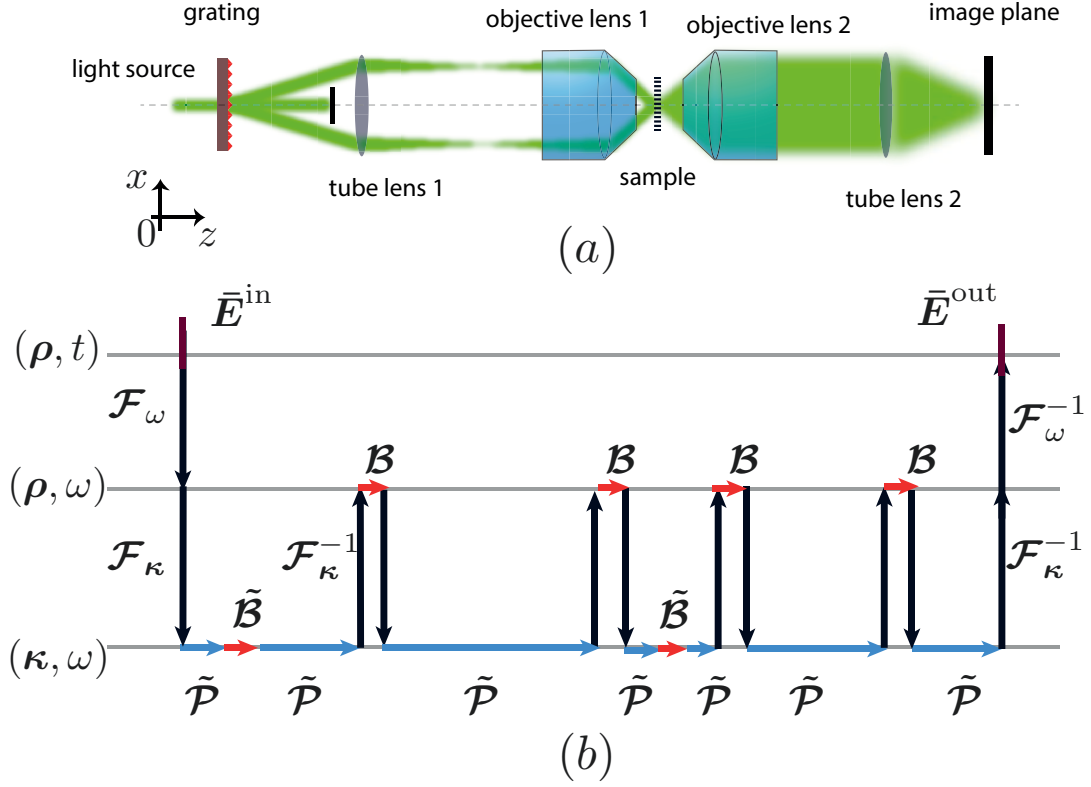


Figure 2: (a). Schematic of a fictitious microscopy system. (b). Field tracing diagram to demonstrate the propagation of the vectorial fields through the entire system, where  $\rho = [x, y]^\top$  and  $\kappa = [k_x, k_y]^\top$  are the transverse components of the position and wavevector respectively.

charge density is also assumed. Therefore, Maxwell's equations in differential form are written as:

$$\nabla \times \bar{E}(\mathbf{r}, t) = -\mu_0 \frac{\partial \bar{H}(\mathbf{r}, t)}{\partial t}, \quad (2.1a)$$

$$\nabla \times \bar{H}(\mathbf{r}, t) = \bar{J}(\mathbf{r}, t) + \frac{\partial \bar{P}(\mathbf{r}, t)}{\partial t} + \epsilon_0 \frac{\partial \bar{E}(\mathbf{r}, t)}{\partial t}, \quad (2.1b)$$

$$\nabla \cdot \bar{E}(\mathbf{r}, t) = -\frac{1}{\epsilon_0} \nabla \cdot \bar{P}(\mathbf{r}, t), \quad (2.1c)$$

$$\nabla \cdot \bar{H}(\mathbf{r}, t) = 0, \quad (2.1d)$$

where  $\mathbf{r} = [x, y, z]^\top$  is the position vector in Cartesian coordinate system.  $t$  represents the variable of time.  $\epsilon_0$  and  $\mu_0$  is the permittivity and permeability in vacuum. Eq.2.1a is the Faraday's law of induction. Eq.2.1b is Ampère-Maxwell's law. Eq.2.1c is Gauss' law. The quantities are listed in Tab.1.

Table 1: Summary of the quantities in Maxwell's equations.

Symbols	Quantities	SI units
$\vec{E}(\mathbf{r}, t)$	Electric field	[V/m]
$\vec{H}(\mathbf{r}, t)$	Magnetic field	[A/m]
$\vec{J}(\mathbf{r}, t)$	Current density	[A/m <sup>2</sup> ]
$\vec{P}(\mathbf{r}, t)$	Dielectric polarization	[As/m <sup>2</sup> ]

#### 2.1.1.2 Space and temporal-frequency domain

It is often the case that the Maxwell's equations in space and temporal-frequency domain is dealt in the modeling. Therefore, the inverse Fourier transforms of all the quantities in Eq. 2.1 are performed as:

$$\vec{E}(\mathbf{r}, t) = \frac{1}{\sqrt{2\pi}} \int_{-\infty}^{\infty} \vec{E}(\mathbf{r}, \omega) \exp(-i\omega t) d\omega, \quad (2.2a)$$

$$\vec{H}(\mathbf{r}, t) = \frac{1}{\sqrt{2\pi}} \int_{-\infty}^{\infty} \vec{H}(\mathbf{r}, \omega) \exp(-i\omega t) d\omega, \quad (2.2b)$$

$$\vec{J}(\mathbf{r}, t) = \frac{1}{\sqrt{2\pi}} \int_{-\infty}^{\infty} \vec{J}(\mathbf{r}, \omega) \exp(-i\omega t) d\omega, \quad (2.2c)$$

$$\vec{P}(\mathbf{r}, t) = \frac{1}{\sqrt{2\pi}} \int_{-\infty}^{\infty} \vec{P}(\mathbf{r}, \omega) \exp(-i\omega t) d\omega, \quad (2.2d)$$

where  $\omega$  is the angular time frequency. Then the fields in space and temporal-frequency domain are obtained as:

$$\nabla \times \vec{E}(\mathbf{r}, \omega) = i\omega\mu_0 \vec{H}(\mathbf{r}, \omega), \quad (2.3a)$$

$$\nabla \times \vec{H}(\mathbf{r}, \omega) = \vec{J}(\mathbf{r}, \omega) - i\omega \vec{P}(\mathbf{r}, \omega) - i\omega\epsilon_0 \vec{E}(\mathbf{r}, \omega), \quad (2.3b)$$

$$\nabla \cdot \vec{E}(\mathbf{r}, \omega) = -\frac{1}{\epsilon_0} \nabla \cdot \vec{P}(\mathbf{r}, \omega), \quad (2.3c)$$

$$\nabla \cdot \vec{H}(\mathbf{r}, \omega) = 0. \quad (2.3d)$$

Then the matter is assumed to be linear and isotropic in this thesis which states:

$$\vec{P}(\mathbf{r}, \omega) = \epsilon_0 \chi(\mathbf{r}, \omega) \vec{E}(\mathbf{r}, \omega), \quad (2.4)$$

where  $\chi$  is the susceptibility. Ohm's law applies to the conductive material as:

$$\vec{J}(\mathbf{r}, \omega) = \sigma^{\text{Ohm}}(\omega) \vec{E}(\mathbf{r}, \omega). \quad (2.5)$$

After the substitution, Eq. 2.3 becomes:

$$\nabla \times \vec{E}(\mathbf{r}, \omega) = i\omega\mu_0 \vec{H}(\mathbf{r}, \omega), \quad (2.6a)$$

$$\nabla \times \vec{H}(\mathbf{r}, \omega) = -i\omega\epsilon_0 \epsilon_r(\mathbf{r}, \omega) \vec{E}(\mathbf{r}, \omega), \quad (2.6b)$$

$$\nabla \cdot \vec{E}(\mathbf{r}, \omega) = -\nabla \cdot \chi(\mathbf{r}, \omega) \vec{E}(\mathbf{r}, \omega), \quad (2.6c)$$

$$\nabla \cdot \vec{H}(\mathbf{r}, \omega) = 0, \quad (2.6d)$$

where  $\epsilon_r(\mathbf{r}, \omega) = \frac{i\sigma^{\text{Ohm}}(\omega)}{\omega\epsilon_0} + \chi(\mathbf{r}, \omega) + 1$  is the relative permittivity of the isotropic medium.

### 2.1.1.3 Spatial-frequency and temporal-frequency domain

The vectorial fields are also very often used in spatial-frequency and temporal-frequency domain at a certain plane. It is also noted as Fourier domain for short. Therefore, they are obtained if the inverse Fourier transform is performed at one plane as:

$$\mathbf{E}(\boldsymbol{\rho}; z, \omega) = \frac{1}{2\pi} \int_{-\infty}^{\infty} \int_{-\infty}^{\infty} \tilde{\mathbf{E}}(\boldsymbol{\kappa}; z, \omega) \exp(-i\boldsymbol{\kappa}\boldsymbol{\rho}) d\boldsymbol{\kappa}, \quad (2.7a)$$

$$\mathbf{H}(\boldsymbol{\rho}; z, \omega) = \frac{1}{2\pi} \int_{-\infty}^{\infty} \int_{-\infty}^{\infty} \tilde{\mathbf{H}}(\boldsymbol{\kappa}; z, \omega) \exp(-i\boldsymbol{\kappa}\boldsymbol{\rho}) d\boldsymbol{\kappa}, \quad (2.7b)$$

where  $\boldsymbol{\rho} = [x, y]^T$  and  $\boldsymbol{\kappa} = [k_x, k_y]^T$  are the transverse components of the position and the wavevector. Then the fields in spatial-frequency and temporal-frequency domain are obtained as:

$$\nabla \times \mathcal{F}_{\boldsymbol{\kappa}}^{-1} [\tilde{\mathbf{E}}(\boldsymbol{\kappa}; z, \omega)] = i\omega\mu_0 \mathcal{F}_{\boldsymbol{\kappa}}^{-1} [\tilde{\mathbf{H}}(\boldsymbol{\kappa}; z, \omega)], \quad (2.8a)$$

$$\nabla \times \mathcal{F}_{\boldsymbol{\kappa}}^{-1} [\tilde{\mathbf{H}}(\boldsymbol{\kappa}; z, \omega)] = -i\omega\epsilon_0\epsilon_r(\mathbf{r}, \omega) \mathcal{F}_{\boldsymbol{\kappa}}^{-1} [\tilde{\mathbf{E}}(\boldsymbol{\kappa}; z, \omega)], \quad (2.8b)$$

$$\nabla \cdot \mathcal{F}_{\boldsymbol{\kappa}}^{-1} [\tilde{\mathbf{E}}(\boldsymbol{\kappa}; z, \omega)] = -\nabla \cdot \chi(\mathbf{r}, \omega) \mathcal{F}_{\boldsymbol{\kappa}}^{-1} [\tilde{\mathbf{E}}(\boldsymbol{\kappa}; z, \omega)], \quad (2.8c)$$

$$\nabla \cdot \mathcal{F}_{\boldsymbol{\kappa}}^{-1} [\tilde{\mathbf{H}}(\boldsymbol{\kappa}; z, \omega)] = 0, \quad (2.8d)$$

where  $\mathcal{F}_{\boldsymbol{\kappa}}^{-1}$  denotes the inverse Fourier transform of the vectorial fields which means the inverse Fourier transform of each component of the vectorial fields.

### 2.1.2 Source models

After the definition of the vectorial electromagnetic fields used in the modeling, the vectorial electric fields of the source are defined as follows. They can be in any forms and in any domains as long as they are governed by Maxwell's equations in general. In this thesis, various types of the vectorial sources are used whose explicit forms are given in the following.

The very commonly used source is plane wave which is defined as:

$$\mathbf{E} = \mathbf{E}_0 e^{-i(\mathbf{k}\mathbf{r} + \omega t)}, \quad (2.9)$$

where  $\mathbf{k} = [k_x, k_y, k_z]^T$  is the wavevector.  $\mathbf{E}_0$  is the amplitude of the plane wave.

In practice, not all plane waves are applied very often but Gaussian waves. Therefore, the paraxial Hermite Gaussian wave is defined as:

$$\mathbf{E}_{\perp} = \begin{bmatrix} E_{x0} \exp \left[ -\frac{x^2 + y^2}{w_0^2} \right] \\ E_{y0} \exp \left[ -\frac{x^2 + y^2}{w_0^2} \right] \exp [i\sigma^{\text{Gau}}] \end{bmatrix}, \quad (2.10)$$

where  $w_0$  is the radius of the waist of the Gaussian wave.  $\sigma^{\text{Gau}}$  is the delayed phase to define the linear ( $\sigma^{\text{Gau}} = 0$ ) or circular ( $\sigma^{\text{Gau}} = \pi/2$ ) polarization.

For the radially polarized beam with non-uniform amplitude, two orthogonally polarized higher order Hermite Gaussian waves are combined as: [65]

$$\mathbf{E}_{\perp} = \begin{bmatrix} E_{x0} \exp \left[ -\frac{x^2 + y^2}{w_0^2} \right] \mathcal{H}_1 \left( \frac{\sqrt{2}x}{w_0} \right) \mathcal{H}_0 \left( \frac{\sqrt{2}y}{w_0} \right) \\ E_{y0} \exp \left[ -\frac{x^2 + y^2}{w_0^2} \right] \mathcal{H}_0 \left( \frac{\sqrt{2}x}{w_0} \right) \mathcal{H}_1 \left( \frac{\sqrt{2}y}{w_0} \right) \end{bmatrix}, \quad (2.11)$$

where  $\mathcal{H}_0$  and  $\mathcal{H}_1$  are the zeroth and first order of the Hermite polynomial.

In the application of Fourier microscopy system, the emission of the fluorescent molecule is modeled by a dipole source which is defined in Fourier domain as follows [65]:

$$\begin{bmatrix} \tilde{E}_x \\ \tilde{E}_y \\ \tilde{E}_z \end{bmatrix} = \frac{i\omega^2\mu_0\mu_1}{2\pi k_1^2 k_z} \begin{bmatrix} (k_1^2 - k_x^2)p_x & -(k_x k_y)p_y & -(k_x k_z)p_z \\ -(k_x k_y)p_x & (k_1^2 - k_y^2)p_y & -(k_y k_z)p_z \\ -(k_x k_z)p_x & -(k_y k_z)p_y & (k_1^2 - k_z^2)p_z \end{bmatrix}, \quad (2.12)$$

where  $\omega$  is the angular frequency,  $\mu_1$  is the relative permeability of the medium,  $k_1$  is the wavenumber in the medium,  $k_x$ ,  $k_y$  and  $k_z$  are the components of the wavevector and  $p_x$ ,  $p_y$  and  $p_z$  are the components of the dipole moment  $\mathbf{p}$ .

### 2.1.3 Operator for free space

The free spaces between two parallel or non-parallel planes are in the gaps of different components. The electromagnetic field propagates rigorously via the Propagation (P) operator denoted by  $\tilde{\mathcal{P}}$  as shown in Fig. 2 (b), in the Fourier domain:

$$\tilde{E}^{\text{out}}(\boldsymbol{\kappa}^{\text{out}}) = \tilde{\mathcal{P}}(\boldsymbol{\kappa}^{\text{out}}, \boldsymbol{\kappa}^{\text{in}}) \tilde{E}^{\text{in}}(\boldsymbol{\kappa}^{\text{in}}), \quad (2.13)$$

where  $\boldsymbol{\kappa}^{\text{out}} = \boldsymbol{\kappa}^{\text{in}}$  and  $\tilde{\mathcal{P}}$  is discussed with details in [94]. From Eq. 2.13, it is concluded that the free space propagation is point-wise in Fourier domain which makes the computation fast. Parabasal field decomposition in Fourier domain is one option to have an efficient calculation [95].

### 2.1.4 Operators for components

The optical system consists of various components, e.g. lenses, gratings, particles, photonic crystal, ect. In the framework provided by field tracing, the effect of each of the component on the electromagnetic field is modeled using a ‘‘Bidirectional (B) operator’’ indicated in Fig. 2 (b), a mathematical construct which contains the information of how a component of the system modifies an input field.

In order to obtain the behavior of the B operator for a given component of the system, different field solvers can be used, depending on the nature of the component. This concept allows us to combine in a single simulation the computation of the electromagnetic field in nano-structures, e.g. gratings, nanoparticles, as well as of the propagation of the same field through an imaging system consisting of lenses.

#### 2.1.4.1 Curved surfaces

The microscopy systems very often consist of different complex lenses which consist of curved surfaces separating homogeneous media. Therefore, the B operator for curved surfaces is required. It is computed using the Local Plane Interface Approximation



(LPIA) [66, 70, 96–99] in the space domain, denoted by  $\mathcal{B}$  as shown in Fig. 2 (b), to propagate the field through the lenses fully vectorially as follows:

$$\mathbf{E}_{\perp}^{\text{out}}(\boldsymbol{\rho}^{\text{out}}) = \mathcal{B}(\boldsymbol{\rho}^{\text{out}}, \boldsymbol{\rho}^{\text{in}}) \mathbf{E}_{\perp}^{\text{in}}(\boldsymbol{\rho}^{\text{in}}), \quad (2.14)$$

where  $\mathbf{E}_{\perp}^{\text{in}}$  and  $\mathbf{E}_{\perp}^{\text{out}}$  are the transverse components of the electric fields at the input and output planes respectively. The longitudinal component can be calculated via Maxwell's equations when it is needed. The B operator works for both ideal and real lenses in the framework of LPIA which will be discussed in details in Sec. 2.2. Its accuracy and computational speed will be carefully evaluated in chapter 3.

#### 2.1.4.2 Micro-/Nano-structures

Besides the complex lenses, the microscopy system also very often contains micro-/nano-structures, e.g. gratings and photonic crystal as shown in Fig. 2 (a).

The B operators for the micro-/nano-structures, denoted by  $\tilde{\mathcal{B}}$  as shown in Fig. 2 (b) are calculated fully vectorially using rigorous Maxwell's equations solver, FMM, based on scattering matrix [93, 100] in the Fourier domain, to propagate the electromagnetic field through micro-/nano-structures:

$$\tilde{\mathbf{E}}_{\perp}(\boldsymbol{\kappa}^{\text{out}}) = \iint \tilde{\mathcal{B}}(\boldsymbol{\kappa}^{\text{out}}, \boldsymbol{\kappa}^{\text{in}}) \tilde{\mathbf{E}}_{\perp}(\boldsymbol{\kappa}^{\text{in}}) d\boldsymbol{\kappa}^{\text{in}}, \quad (2.15)$$

where  $\boldsymbol{\kappa}^{\text{out}} = [k_x^{\text{out}}, k_y^{\text{out}}]^{\top}$  and  $\boldsymbol{\kappa}^{\text{in}} = [k_x^{\text{in}}, k_y^{\text{in}}]^{\top}$  are the transverse components of the wavevector at output plane and input plane respectively. This equation is interpreted as multi-spatial-frequency input plane waves interacted with the structure and the multi-spatial-frequency output plane waves are generated.

When the micro-/nano-structures are periodic, e.g. gratings, photonic crystal, the output field is decomposed according to the diffraction order of the periodic structure as:

$$\tilde{\mathbf{E}}_{\perp}^{\text{out},j}(\boldsymbol{\kappa}^{\text{out},j}) = \tilde{\mathcal{B}}^j(\boldsymbol{\kappa}^{\text{out},j}, \boldsymbol{\kappa}^{\text{in}}) \tilde{\mathbf{E}}_{\perp}^{\text{in}}(\boldsymbol{\kappa}^{\text{in}}), \quad (2.16)$$

where  $j = [j_x, j_y]$  denotes the diffraction orders in  $x$  and  $y$  directions.  $\boldsymbol{\kappa}^{\text{out},j}$  is connected with the input wavevector as  $\boldsymbol{\kappa}^{\text{out},j} = \boldsymbol{\kappa}^{\text{in}} + \left[ j_x \frac{2\pi}{d_x} + j_y \frac{2\pi}{d_y} \right]$  with  $d_x$  and  $d_y$  are the periods of the periodic structures in  $x$  and  $y$  directions. The B operators applied for the periodic and non-periodic structures, which will be formulated in Sec 2.3.

From Eq. 2.16, it is concluded that for each diffraction order, the input and output fields are related point-wisely in the Fourier domain. In this manner, the computation can be accelerated, when only several diffraction orders are required, e.g. a 1D photonic crystal or a grating with the periods comparable to wavelength.

### 2.1.5 Fourier transforms

After reviewing the field tracing diagram in Fig. 2 (b), it is known that the Fourier Transforms (FT) between different domains are also essential to complete the entire modeling. They are applied to transform the vectorial field as:

$$E(\rho, \omega) = \mathcal{F}_\omega [\bar{E}(\rho, t)], \quad (2.17a)$$

$$\bar{E}(\rho, t) = \mathcal{F}_\omega^{-1} [E(\rho, \omega)], \quad (2.17b)$$

$$\tilde{E}(\kappa, \omega) = \mathcal{F}_\kappa [E(\rho, \omega)], \quad (2.17c)$$

$$E(\rho, \omega) = \mathcal{F}_\kappa^{-1} [\tilde{E}(\kappa, \omega)]. \quad (2.17d)$$

In order to accelerate the computational speed of the FT, the Homeomorphic Fourier Transform (HFT) [101, 102], also sometimes called geometric Fourier transform [103], on the basis of the stationary phase approximation is performed.

If the diffraction from the apertures is included, the Fast Fourier Transform (FFT) would be used instead of the HFT. (the pointwise nature of the HFT fails to account for that effect but, because the FFT is a coherent summation of all the plane-wave components of the spectrum, it does include diffraction). It is slower than than HFT, but still much faster than the method using direct integral. It can be accelerated with the semi-analytical approach in certain circumstances discussed in [104]. The Inverse HFT (IHFT) is applied in stead of Inverse FFT (IFFT) with the same logic.

### 2.1.6 Measured quantities

#### 2.1.6.1 Energy conservation

With the help of Eq. 2.1a and Eq. 2.1b, the electromagnetic fields are dealt with as real functions:

$$\nabla \times \bar{E}^{(r)}(\mathbf{r}, t) = -\frac{\partial}{\partial t} \bar{B}^{(r)}(\mathbf{r}, t), \quad (2.18a)$$

$$\nabla \times \bar{H}^{(r)}(\mathbf{r}, t) = \bar{J}(\mathbf{r}, t) + \frac{\partial}{\partial t} \bar{D}^{(r)}(\mathbf{r}, t), \quad (2.18b)$$

where  $\bar{B}^{(r)}$  and  $\bar{D}^{(r)}$  are the magnetic induction and electric displacement respectively. Make the dot production of Eq. 2.18a with  $\bar{H}^{(r)}(\mathbf{r}, t)$  and Eq. 2.18b with  $\bar{E}^{(r)}(\mathbf{r}, t)$  and subtract. And furthermore, with the use of differential rule of the nabla operator, the above equation becomes:

$$\nabla \cdot (\bar{E}^{(r)} \times \bar{H}^{(r)}) + \bar{H}^{(r)} \cdot \frac{\partial}{\partial t} \bar{B}^{(r)} + \bar{E}^{(r)} \cdot \frac{\partial}{\partial t} \bar{D}^{(r)} + \bar{E}^{(r)} \bar{J}^{(r)} = 0, \quad (2.19)$$

It represents the energy conservation law from Maxwell's equations. Please note that the arguments  $(\mathbf{r}, t)$  are omitted for the brevity.

#### 2.1.6.2 Poynting vector and energy density

Since the energy conservation law is formulated in Eq. 2.19, it is desired that physical quantities, which are related to the energy, would be defined. Therefore, Poynting vector is defined as the energy flux density vector as:

$$\mathbf{S}^{(r)}(\mathbf{r}, t) = \bar{E}^{(r)}(\mathbf{r}, t) \times \bar{H}^{(r)}(\mathbf{r}, t), \quad (2.20)$$

with the unit of  $[\text{W}/\text{m}^2]$ . The electric energy density  $w_e^{(r)}(\mathbf{r}, t)$  is by:

$$\frac{\partial}{\partial t} w_e^{(r)}(\mathbf{r}, t) = \bar{\mathbf{E}}^{(r)}(\mathbf{r}, t) \cdot \frac{\partial}{\partial t} \bar{\mathbf{D}}^{(r)}(\mathbf{r}, t), \quad (2.21)$$

with the unit of  $[\text{J}/\text{m}^3]$ . The magnetic energy density  $w_m^{(r)}(\mathbf{r}, t)$  is defined by:

$$\frac{\partial}{\partial t} w_m^{(r)}(\mathbf{r}, t) = \bar{\mathbf{H}}^{(r)}(\mathbf{r}, t) \cdot \frac{\partial}{\partial t} \bar{\mathbf{B}}^{(r)}(\mathbf{r}, t), \quad (2.22)$$

with the unit of  $[\text{J}/\text{m}^3]$ . The current power density  $q^{(r)}(\mathbf{r}, t)$  is defined as:

$$q^{(r)}(\mathbf{r}, t) = \bar{\mathbf{E}}^{(r)}(\mathbf{r}, t) \cdot \bar{\mathbf{J}}^{(r)}(\mathbf{r}, t), \quad (2.23)$$

with the unit of  $[\text{W}/\text{m}^3]$ .

By assuming time harmonic fields, the Poynting vector is calculated by Eq. 2.20 as:

$$\mathbf{S}(\mathbf{r}, \omega) = \frac{1}{2} \Re(\mathbf{E}(\mathbf{r}, \omega) \times \mathbf{H}^*(\mathbf{r}, \omega)). \quad (2.24)$$

The electric and magnetic energy density are calculated by Eq. 2.21 and Eq. 2.22 respectively as:

$$w_e(\mathbf{r}, \omega) = \frac{\epsilon}{4} \mathbf{E}(\mathbf{r}, \omega) \cdot \mathbf{E}^*(\mathbf{r}, \omega) = \frac{\epsilon}{4} |\mathbf{E}(\mathbf{r}, \omega)|^2, \quad (2.25a)$$

$$w_m(\mathbf{r}, \omega) = \frac{\mu}{4} \mathbf{H}(\mathbf{r}, \omega) \cdot \mathbf{H}^*(\mathbf{r}, \omega) = \frac{\mu}{4} |\mathbf{H}(\mathbf{r}, \omega)|^2. \quad (2.25b)$$

Any of the image, focal spot and interference pattern are defined as time averaged electric energy density of  $\langle w_e^{(r)}(\mathbf{r}, t) \rangle_t$  for non-time-harmonic field, or electric energy density of Eq. 2.25a for time harmonic field. Since the energy density, which is the summation of electric energy density and magnetic energy density, only has a scaling of electric energy density. Therefore, the electric energy density is called energy density for short.

#### 2.1.6.3 Diffraction efficiency

Here, the energy flux through a surface is defined as:

$$\Phi_e = \iint_{\Gamma} \mathbf{S}(\mathbf{r}, \omega) \cdot \hat{\mathbf{a}}(\mathbf{r}) d\tau, \quad (2.26)$$

where  $\hat{\mathbf{a}}$  is the normal vector to the surface  $\Gamma$ . The efficiency is defined as:

$$\eta = \frac{\Phi_e^{\text{out}}}{\Phi_e^{\text{in}}}. \quad (2.27)$$

where  $\Phi_e^{\text{in}}$  and  $\Phi_e^{\text{out}}$  are the energy flux densities which goes in and out of the surfaces respectively.

#### 2.1.6.4 Contrast and inhomogeneity

In order to evaluate the quality of the interference pattern, the contrast and the inhomogeneity are defined following the definition of electric energy density as:

$$c = \frac{w_{e,\text{up}}^{\text{ave}} - w_{e,\text{down}}^{\text{ave}}}{w_{e,\text{up}}^{\text{ave}} + w_{e,\text{down}}^{\text{ave}}}, \quad (2.28)$$

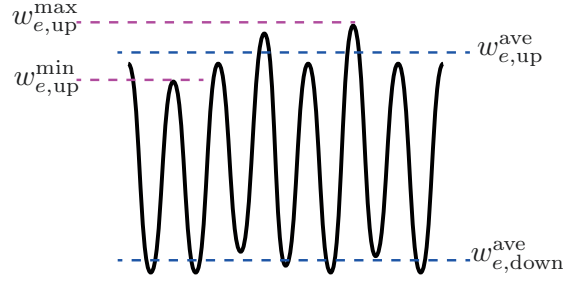


Figure 3: Illustration of the definition of contrast and inhomogeneity of the interference pattern.

where  $w_{e,up}^{ave}$  and  $w_{e,down}^{ave}$  are the averaged values of the maxima and minima of electric energy density respectively as illustrated in Fig. 3. The best contrast leads to  $c = 1$ . Inhomogeneity is another important criteria for the quality of the interference pattern. It is defined as:

$$\sigma = \frac{w_{e,up}^{max} - w_{e,up}^{min}}{w_{e,up}^{max} + w_{e,up}^{min}}, \quad (2.29)$$

where  $w_{e,up}^{max}$  and  $w_{e,up}^{min}$  are the maximum and minimum values of the maxima of electric energy density respectively as illustrated in Fig. 3. The smallest inhomogeneity leads to  $\sigma = 0$ .

#### 2.1.6.5 Deviation

In order to compare two functions, e.g. amplitude, phase, energy density, etc., the deviation between two functions is defined as:

$$\sigma^{dev} = \frac{\sum_{x,y} |f^{Ana}(x,y) - f^{Ref}(x,y)|^2}{\sum_{x,y} |f^{Ref}(x,y)|^2} \quad (2.30)$$

Please note that the notation  $\sigma^{dev}$  is different from the notations  $\sigma$  which denotes the inhomogeneity and  $\sigma^{Ohm}(\omega)$  which denotes the conductivity.

## 2.2 OPERATOR FOR CURVED SURFACES

### 2.2.1 Introduction

As it is mentioned in chapter 1, the lens systems are heavily included in the microscopy systems. The lens system can be either real lens systems [56, 105] or ideal lens systems [62, 63, 66]. The real lens systems nowadays are mainly the combination of different curved surfaces. The ideal lens systems can also be modeled well by a Gaussian reference sphere which is interpreted as a fictitious curved surface. Therefore, the modeling of the electromagnetic field propagation through the curved surface is essential for modeling of microscopy systems.

In order to model the real curved surface rigorously, the rigorous Maxwell's solvers

should be applied [93]. However it takes lots of numerical effort which makes it inapplicable for the size of curved surface beyond around 100  $\mu\text{m}$ . Therefore, an efficient modeling technique with full vectorial effect is preferred.

The so-called Local Plane Interface Approximation (LPIA) is applied to model electromagnetic field propagation through surfaces with full vectorial effect [66, 96, 105–107]. It is even preferable to model curved surface. The reason will be explained in chapter 3. It is much more efficient compared with the rigorous methods when the first order of LPIA is considered which means the electromagnetic field interacts with the curved surface only once. The ideal curved surface follows the analogous logic to allow the modeling of the ideal lens efficiently [66, 69, 70].

In this section, the electromagnetic field propagation through the real or ideal curved surface to a reference plane is fully formulated by the B operator. The local boundary condition and the free space propagation are interpreted and formulated totally separately. By the combination of the local boundary condition and the free space propagation, the full B operator is obtained.

This section is organized as: In subsection 2.2.2, the problem is briefly stated. In subsection 2.2.3, the coordinate transformation matrix is formulated to make it possible to transform the field in the global coordinate to local coordinate, or vice versa, to apply the local boundary condition straightforwardly. In subsection 2.2.4, the local boundary condition is formulated for both real ideal curved surfaces.

### 2.2.2 Problem statement

As shown in Fig. 4, the input field and the output field are in two planes. These two planes can be parallel or non-parallel to each other [94]. The surface indicated by the bold black curve can be interpreted as real surface which separates two different media or fictitious surface on which the electromagnetic field is “refracted” according to any predefined directions. For the simplicity of the demonstration, the parallel one is taken here but it is not a general restriction. If the input and output fields are connected in two planes, it can be used in the framework of field tracing for the entire system modeling [86, 87].

By expanding the B operator in Eq. 2.14, the propagation through the surface from the input plane to the output plane (possibly also the focal plane) is expressed by the operator equation:

$$E_{\perp}^{\text{out}} = \mathcal{P}^{\text{out}} \mathcal{B}^{\text{LPIA}} \mathcal{P}^{\text{in}} E_{\perp}^{\text{in}}, \quad (2.31)$$

It is known that  $\mathcal{B} = \mathcal{P}^{\text{out}} \mathcal{B}^{\text{LPIA}} \mathcal{P}^{\text{in}}$ .  $\mathcal{P}^{\text{in}}$  and  $\mathcal{P}^{\text{out}}$  are the propagation operators, which denote the free-space propagation from the input plane to the curved surface and from the curved surface to the output plane respectively as indicated in Fig. 4.

In principle this free-space propagation can be solved rigorously by Fast Fourier Transform (FFT) based techniques [69] and/or propagation integrals [108, 109], e.g. Debye integral [62–66]. It can also be solved approximately by local plane-wave propagation [66, 96]. In this thesis, the numerically most efficient way to implement this propagation is not the focus; it is concentrated on the modeling of the boundary condition on the curved surface itself, that is, on the B operator  $\mathcal{B}^{\text{LPIA}}$  in Eq. 2.31. The input and out-

put fields at the curved surface are directly connected by the boundary condition via B operator  $\mathcal{B}^{\text{LPIA}}$  as:

$$\mathbf{E}_{\perp}^{\text{out}_c} = \mathcal{B}^{\text{LPIA}} \mathbf{E}_{\perp}^{\text{in}_c}, \quad (2.32)$$

where  $\mathbf{E}_{\perp}^{\text{in}_c}$  and  $\mathbf{E}_{\perp}^{\text{out}_c}$  are the input and output fields at the curved surface.

### 2.2.3 Coordinate transformation on curved surface

#### 2.2.3.1 General form

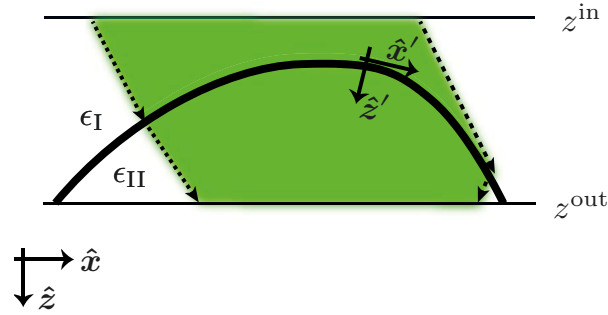


Figure 4: Schematic of LPIA. The field propagates from the input reference plane  $z = z^{\text{in}}$  to the curved surface and then to the output reference plane  $z = z^{\text{out}}$ .  $\epsilon_I$  and  $\epsilon_{II}$  are the permittivities of the media of the input and output regions respectively.

The local boundary condition is formulated in the local coordinate system at each point in the surface. Therefore, the fields are needed to be transformed from the global coordinate system to the local coordinate system on the curved surface, and vice versa. The unit vectors of the axes of the global coordinate system are, in Cartesian form:

$$\hat{\mathbf{x}} = [1, 0, 0]^T, \quad (2.33a)$$

$$\hat{\mathbf{y}} = [0, 1, 0]^T, \quad (2.33b)$$

$$\hat{\mathbf{z}} = [0, 0, 1]^T, \quad (2.33c)$$

where  $\hat{\mathbf{x}}$ ,  $\hat{\mathbf{y}}$ ,  $\hat{\mathbf{z}}$  are the unit vectors of the  $x$ ,  $y$  and  $z$  axes respectively. The unit vectors of the axes of the local coordinate system would then be:

$$\hat{\mathbf{x}}' = q_{11}\hat{\mathbf{x}} + q_{12}\hat{\mathbf{y}} + q_{13}\hat{\mathbf{z}}, \quad (2.34a)$$

$$\hat{\mathbf{y}}' = q_{21}\hat{\mathbf{x}} + q_{22}\hat{\mathbf{y}} + q_{23}\hat{\mathbf{z}}, \quad (2.34b)$$

$$\hat{\mathbf{z}}' = q_{31}\hat{\mathbf{x}} + q_{32}\hat{\mathbf{y}} + q_{33}\hat{\mathbf{z}}, \quad (2.34c)$$

where  $\hat{\mathbf{x}}'$ ,  $\hat{\mathbf{y}}'$ ,  $\hat{\mathbf{z}}'$  are the unit vectors of the  $x'$ ,  $y'$  and  $z'$  -axes. Therefore, it is written as:

$$[\hat{\mathbf{x}}', \hat{\mathbf{y}}', \hat{\mathbf{z}}']^T = \mathcal{Q}[\hat{\mathbf{x}}, \hat{\mathbf{y}}, \hat{\mathbf{z}}]^T, \quad (2.35)$$

where  $\mathcal{Q}$  is the transformation matrix:

$$\mathcal{Q} = \begin{bmatrix} q_{11} & q_{12} & q_{13} \\ q_{21} & q_{22} & q_{23} \\ q_{31} & q_{32} & q_{33} \end{bmatrix}. \quad (2.36)$$

Using the orthogonality of the transformation matrix, Eq. 2.35 can be rewritten:

$$[\hat{x}, \hat{y}, \hat{z}] = [\hat{x}', \hat{y}', \hat{z}'] \mathcal{Q}. \quad (2.37)$$

### 2.2.3.2 Example of sinusoidal surface

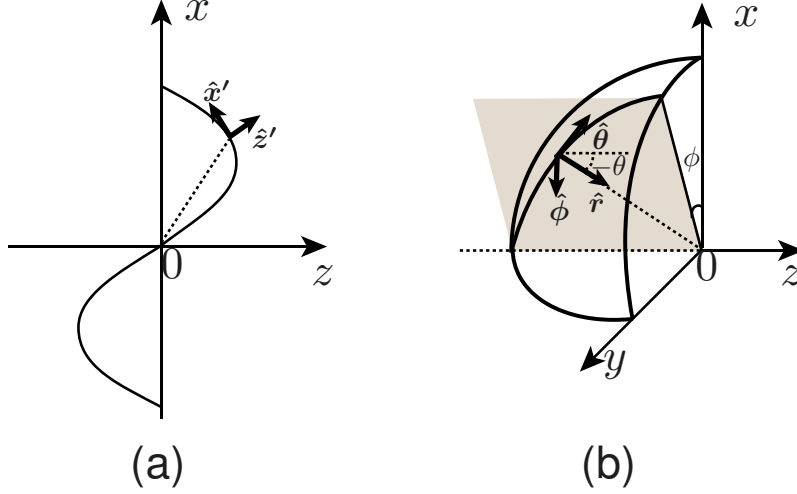


Figure 5: (a). Sinusoidal surface.  $[\hat{x}', \hat{z}']^T$  is the unit vector of the local coordinate. (b). Spherical surface.  $[\hat{\theta}, \hat{\phi}, \hat{r}]^T$  is the unit vector of the local spherical coordinate.

Even though sinusoidal curved surface is not very often included in the lens system in microscopy systems, it is used in general. It is also a good specific example to present a general curved surface. Since the structure is 2D, it is assumed to be  $y$ -invariant. So the local coordinate unit vector as shown in Fig. 5 (a), is rewritten as:

$$\hat{x}' = \cos\theta \hat{x} - \sin\theta \hat{z}, \quad (2.38a)$$

$$\hat{y}' = \hat{y}, \quad (2.38b)$$

$$\hat{z}' = \sin\theta \hat{x} + \cos\theta \hat{z}. \quad (2.38c)$$

Therefore, the transformation matrix is written as:

$$\mathcal{Q} = \begin{bmatrix} \cos\theta & 0 & -\sin\theta \\ 0 & 1 & 0 \\ \sin\theta & 0 & \cos\theta \end{bmatrix}. \quad (2.39)$$

The angle  $\theta$  is the rotation angle of the local position about the  $y$  axis. It can be obtained by the from the surface formula, e.g. of sinusoidal surface  $z = a \sin(\frac{2\pi}{d}x) + z_0$ , as:

$$\theta = \arctan \left[ \frac{2\pi a}{d} \cos(\frac{2\pi}{d}x) \right]. \quad (2.40)$$

### 2.2.3.3 Example of spherical surface

Spherical surfaces are very often the elementary surface of a real lens system. It can also be the fictitious surface to model the ideal lens on which the electromagnetic field

changes its propagation direction and the amplitude. Therefore, it is important to know the specific form of the coordinate transformation matrix. The local unit vector in spherical coordinates has the following form:

$$[\hat{x}', \hat{y}', \hat{z}']^T = [\hat{\theta}, \hat{\phi}, \hat{r}]^T, \quad (2.41)$$

and is related to the global coordinate system, as shown in Fig. 5 (b), via:

$$\hat{\theta} = \cos\theta\cos\phi\hat{x} + \cos\theta\sin\phi\hat{y} - \sin\theta\hat{z}, \quad (2.42a)$$

$$\hat{\phi} = -\sin\phi\hat{x} + \cos\phi\hat{y}, \quad (2.42b)$$

$$\hat{r} = \sin\theta\cos\phi\hat{x} + \sin\theta\sin\phi\hat{y} + \cos\theta\hat{z}, \quad (2.42c)$$

where  $\theta$  and  $\phi$  are the angular spherical coordinates of the local position, which can be obtained from the Cartesian coordinates,

$$\theta = -\arccos \frac{|z|}{\sqrt{x^2 + y^2 + z^2}}, \quad (2.43a)$$

$$\phi = \arctan \frac{y}{x}. \quad (2.43b)$$

For the Gaussian reference spherical surface of radius  $r_0$  and centered on the focus point, it is  $z = -\sqrt{r_0^2 - x^2 - y^2}$ . Therefore, the spherical coordinates are:

$$\theta = -\arccos \frac{\sqrt{r_0^2 - x^2 - y^2}}{r_0}, \quad (2.44a)$$

$$\phi = \arctan \frac{y}{x}. \quad (2.44b)$$

Therefore, the following expression for the transformation matrix from Eq. 2.36 as shown in Fig. 5 (b) is written as:

$$\mathcal{Q} = \begin{bmatrix} \cos\theta\cos\phi & \cos\theta\sin\phi & -\sin\theta \\ -\sin\phi & \cos\phi & 0 \\ \sin\theta\cos\phi & \sin\theta\sin\phi & \cos\theta \end{bmatrix} = \begin{bmatrix} \cos\theta & 0 & -\sin\theta \\ 0 & 1 & 0 \\ \sin\theta & 0 & \cos\theta \end{bmatrix} \begin{bmatrix} \cos\phi & \sin\phi & 0 \\ -\sin\phi & \cos\phi & 0 \\ 0 & 0 & 1 \end{bmatrix}. \quad (2.45)$$

Eq. 2.45 can be interpreted as the rotation of the coordinate system first an angle  $\phi$  about the  $z$  axis and then an angle  $\theta$  about the  $\phi$  axis.

#### 2.2.3.4 Transverse form

From the transformation matrix and with the help of Eq. 2.35, it is known that the input electric field at the curved surface expressed in local coordinates would be

$$E'^{\text{inc}} = \mathcal{Q}E^{\text{inc}}, \quad (2.46)$$

where  $E'^{\text{inc}} = [E_{x'}^{\text{inc}}, E_{y'}^{\text{inc}}, E_{z'}^{\text{inc}}]^T$  and  $E^{\text{inc}} = [E_x^{\text{inc}}, E_y^{\text{inc}}, E_z^{\text{inc}}]^T$  are the input field at the curved surface in local and global coordinates respectively. In accordance with Eq. 2.32 which contains the two components of electric field, Eq. 2.46 is written just in the form as:

$$E_{\perp}^{\text{inc}} = Y^{\text{loc}} E_{\perp}^{\text{inc}}, \quad (2.47)$$



where  $\mathbf{E}_{\perp}^{\text{inc}} = [E_{x'}^{\text{inc}}, E_{y'}^{\text{inc}}]^T$  and  $\mathbf{E}_{\perp}^{\text{inc}} = [E_x^{\text{inc}}, E_y^{\text{inc}}]^T$  are the components of the input field at the curved surface in local and global coordinates respectively. The input field is assumed to be that, which can be decomposed into local plane waves, so that the  $z$  component can be calculated as follows:

$$E_z^{\text{inc}} = \frac{k_x E_x^{\text{inc}} + k_y E_y^{\text{inc}}}{-k_{z,I}}, \quad (2.48)$$

with  $k_x$ ,  $k_y$  and  $k_{z,I} = \sqrt{k_0^2 \epsilon_I - k_x^2 - k_y^2}$  the  $x$ ,  $y$  and  $z$  components of the wavevector  $\mathbf{k}$  of the input field in global coordinates.  $\epsilon_I$  is the relative permittivity of the first medium.  $k_0$  is the wave number in vacuum. From Eq. 2.46, Eq. 2.47 and Eq. 2.48,  $\mathbf{Y}^{\text{loc}}$  can be obtained:

$$\mathbf{Y}^{\text{loc}} = \begin{bmatrix} \frac{-k_{z,I}q_{11} + k_x q_{13}}{-k_{z,I}} & \frac{-k_{z,I}q_{12} + k_y q_{13}}{-k_{z,I}} \\ \frac{-k_{z,I}q_{21} + k_x q_{23}}{-k_{z,I}} & \frac{-k_{z,I}q_{22} + k_y q_{23}}{-k_{z,I}} \end{bmatrix}. \quad (2.49)$$

Corresponding to Eq. 2.46, the electric field from local to global coordinates is desired as:

$$\mathbf{E}^{\text{out}_c} = \mathbf{Q}^T \mathbf{E}'^{\text{out}_c}, \quad (2.50)$$

where  $\mathbf{E}^{\text{out}_c} = [E_x^{\text{out}_c}, E_y^{\text{out}_c}, E_z^{\text{out}_c}]^T$  and  $\mathbf{E}'^{\text{out}_c} = [E_{x'}^{\text{out}_c}, E_{y'}^{\text{out}_c}, E_{z'}^{\text{out}_c}]^T$  are the output field at the curved surface in global and local coordinates respectively.

Analogously to Eq. 2.47, the components of the output field in global coordinates are obtained, by assuming the output field behaves like local plane waves on the curved surface:

$$\mathbf{E}_{\perp}^{\text{out}_c} = \mathbf{Y}^{\text{out}} \mathbf{E}_{\perp}'^{\text{out}_c}, \quad (2.51)$$

where  $\mathbf{E}_{\perp}'^{\text{out}_c} = [E_{x'}^{\text{out}_c}, E_{y'}^{\text{out}_c}]^T$  and  $\mathbf{E}_{\perp}^{\text{out}_c} = [E_x^{\text{out}_c}, E_y^{\text{out}_c}]^T$  are the  $x$  and  $y$  components of the output field in local and global coordinates respectively.  $\mathbf{Y}^{\text{out}}$  is calculated as:

$$\mathbf{Y}^{\text{out}} = \begin{bmatrix} \frac{-k'_{z,\text{II}}q_{11} + k'_x q_{31}}{-k'_{z,\text{II}}} & \frac{-k'_{z,\text{II}}q_{21} + k'_y q_{31}}{-k'_{z,\text{II}}} \\ \frac{-k'_{z,\text{II}}q_{12} + k'_x q_{32}}{-k'_{z,\text{II}}} & \frac{-k'_{z,\text{II}}q_{22} + k'_y q_{32}}{-k'_{z,\text{II}}} \end{bmatrix}, \quad (2.52)$$

where  $k'_x$ ,  $k'_y$  and  $k'_{z,\text{II}} = \sqrt{k_0^2 \epsilon_{\text{II}} - k_x'^2 - k_y'^2}$  are the  $x$ ,  $y$  and  $z$  components of the wave vector of the output field in local coordinates.  $\epsilon_{\text{II}}$  is the relative permittivity of the medium at the output.

#### 2.2.4 Local boundary condition on curved surface

##### 2.2.4.1 Real surface boundary condition

Next, it is considered that how to connect the input field  $\mathbf{E}_{\perp}^{\text{inc}}$  in Eq. 2.47 and output field  $\mathbf{E}_{\perp}'^{\text{out}_c}$  in Eq. 2.51 in local coordinates. The locally curved surface is approximated by a local plane interface. Then Fresnel's law is applied:

$$\mathbf{E}_{\perp}'^{\text{out}_c} = \mathcal{C}^{\text{Fres}} \mathbf{E}_{\perp}^{\text{inc}}, \quad (2.53)$$

where for the transmitted field,  $\mathcal{C}^{\text{Fres}}$  which is the Fresnel coefficient, is given by:

$$\mathcal{C}_t^{\text{Fres}} = \begin{bmatrix} \frac{2\epsilon_I k'_{z,\text{II}}}{\epsilon_I k'_{z,\text{II}} + \epsilon_{\text{II}} k'_{z,\text{I}}} & 0 \\ 0 & \frac{2k'_{z,\text{I}}}{k'_{z,\text{II}} + k'_{z,\text{I}}} \end{bmatrix}, \quad (2.54)$$

for the reflected field,  $\mathcal{C}^{\text{Fres}}$  is given by:

$$\mathcal{C}_r^{\text{Fres}} = \begin{bmatrix} \frac{\epsilon_I k'_{z,\text{II}} - \epsilon_{\text{II}} k'_{z,\text{I}}}{\epsilon_I k'_{z,\text{II}} + \epsilon_{\text{II}} k'_{z,\text{I}}} & 0 \\ 0 & \frac{-k'_{z,\text{II}} + k'_{z,\text{I}}}{k'_{z,\text{II}} + k'_{z,\text{I}}} \end{bmatrix}, \quad (2.55)$$

where  $k'_{z,\text{I}} = \sqrt{k_0^2 \epsilon_I - k_x'^2 - k_y'^2}$  is the  $z$  component of the  $\mathbf{k}$ -vector of the input field in local coordinates. The Fresnel coefficients used here are formulated by the wavevector instead of the angles which are often used in a text book. And they are formulated for only the transverse components of the electric field instead of the entire electric field. Therefore, the rigorous derivation procedure is added in the appendix.

Then, from Eq. 2.47, Eq. 2.51 and Eq. 2.53, the whole local boundary condition in the local B operator form is written as:

$$\mathcal{B}^{\text{LPIA}} = \mathbf{Y}^{\text{out}} \mathcal{C}^{\text{Fres}} \mathbf{Y}^{\text{loc}}, \quad (2.56)$$

It can be calculated straightforwardly by numerical computation. The time complexity of the LPIA is  $\mathcal{O}(n)$ , where  $n$  is the sampling points of the field, mainly the wave front. The time complexity of the rigorous solver, e.g. FMM, is around  $\mathcal{O}(m^3)$ , where  $m$  is the sampling points of the field with wrapped phase. Normally, it is the situation that  $m$  is much great than  $n$  as  $m \gg n$ . Therefore, the computational effort of the rigorous solvers is huge compared to LPIA. For the same example, the optical structures are the same between LPIA, FEM and FMM, but they are numerically represented differently. LPIA only takes the surface, which is usually analytically given, of the structure for calculation. FEM uses meshes to represent the whole structure. FMM uses layers to represent the whole structure. They are again much more time expensive than the case of LPIA.

#### 2.2.4.2 Ideal surface boundary condition

Next, it is considered how to connect the input field  $\mathbf{E}_{\perp}^{\text{inc}}$  in Eq. 2.47 and the output field  $\mathbf{E}_{\perp}^{\text{outc}}$  from Eq. 2.51 in the local coordinate system for an ideal lens which is represented by a fictitious curved surface as:

$$\mathbf{E}_{\perp}^{\text{outc}} = \mathcal{C}^{\text{Ideal}} \mathbf{E}_{\perp}^{\text{inc}}. \quad (2.57)$$

The aim is to determine the transmission and/or reflection coefficients  $\mathcal{C}^{\text{Ideal}}$  in the local coordinate system.

For the ideal lens which is interpreted as a fictitious curved surface, the Fresnel law is

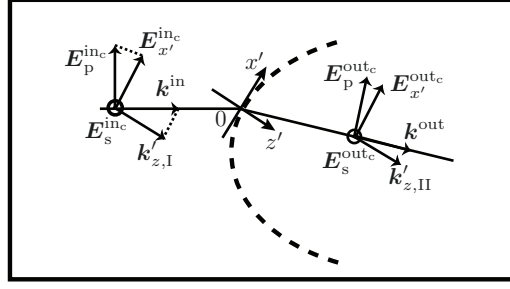


Figure 6: Schematic of the electric field propagating through a fictitious curved surface in local coordinate system.

invalidated. The transmission and reflection coefficients are obtained by energy conservation. It is assumed that there is no reflected field, all the energy is therefore transmitted. Thus the following equation (written in the local coordinate system) is obtained as:

$$\iint \mathbf{S}'^{\text{in}} \cdot d\mathbf{s}'^{\text{in}} = \iint \mathbf{S}'^{\text{out}} \cdot d\mathbf{s}'^{\text{out}}, \quad (2.58)$$

where  $\mathbf{S}'^{\text{in}}$  and  $\mathbf{S}'^{\text{out}}$  is the Poynting vector of the in- and output fields respectively.  $d\mathbf{s}'^{\text{in}}$  and  $d\mathbf{s}'^{\text{out}}$  correspond to the vector surface area differentials of the input and output surfaces respectively. In this case, the input and output surfaces coincide, so the surface-area terms in the equation cancel out and it is obtained:

$$\|\mathbf{S}'^{\text{in}}\| \frac{k'_{z,I}}{k_0 n_I} = \|\mathbf{S}'^{\text{out}}\| \frac{k'_{z,II}}{k_0 n_{II}}, \quad (2.59)$$

where  $k'_{z,I}$  and  $k'_{z,II}$  are the  $z$  components of the input and output wave vectors on the surface written in the local coordinate system.  $n_I$  and  $n_{II}$  are the refractive indices of the input and output regions.

The field is assumed to be local plane wave at the curved surface. Therefore, the field vector is perpendicular to the propagating direction as shown in Fig. 6. The field is decomposed into  $p$  and  $s$  modes which are parallel and perpendicular to the paper plane, respectively. From the decomposition and local-plane-wave assumption, a sufficient condition for Eq. 2.59 is obtained as:

$$|E_p^{\text{inc}}|^2 \frac{k'_{z,I}}{k_0 n_I} = |E_p^{\text{outc}}|^2 \frac{k'_{z,II}}{k_0 n_{II}}, \quad (2.60a)$$

$$|E_s^{\text{inc}}|^2 \frac{k'_{z,I}}{k_0 n_I} = |E_s^{\text{outc}}|^2 \frac{k'_{z,II}}{k_0 n_{II}}, \quad (2.60b)$$

where  $|E_p^{\text{inc}}|$  and  $|E_s^{\text{inc}}|$  are the amplitudes of the  $p$  and  $s$  modes of the input field, and  $|E_p^{\text{outc}}|$  and  $|E_s^{\text{outc}}|$  are the amplitude of the  $p$  and  $s$  modes of the output field. As shown

in Fig. 6, the relations between the amplitudes of the  $p$  and  $s$  modes and the amplitudes of the  $x'$  and  $y'$  components for both input and output fields are obtained as:

$$|E_p^{\text{inc}}| = \frac{k_0 n_I}{k'_{z,I}} |E_{x'}^{\text{inc}}|, \quad (2.61a)$$

$$|E_s^{\text{inc}}| = |E_{y'}^{\text{inc}}|, \quad (2.61b)$$

$$|E_p^{\text{outc}}| = \frac{k_0 n_{II}}{k'_{z,II}} |E_{x'}^{\text{outc}}|, \quad (2.61c)$$

$$|E_s^{\text{outc}}| = |E_{y'}^{\text{outc}}|. \quad (2.61d)$$

By inserting Eq. 2.61 into Eq. 2.60, the components in the local coordinate system are obtained as:

$$|E_{x'}^{\text{inc}}| \sqrt{\frac{k_0 n_I}{k'_{z,I}}} = |E_{x'}^{\text{outc}}| \sqrt{\frac{k_0 n_{II}}{k'_{z,II}}}, \quad (2.62a)$$

$$|E_{y'}^{\text{inc}}| \sqrt{\frac{k'_{z,I}}{k_0 n_I}} = |E_{y'}^{\text{outc}}| \sqrt{\frac{k'_{z,II}}{k_0 n_{II}}}. \quad (2.62b)$$

The refractive indices are assumed to be the same in both the input and output regions;  $n_I = n_{II}$ . Therefore, the transmission coefficients are:

$$\mathbf{C}^{\text{Ideal}} = \mathbf{C}_t^{\text{Ideal}} = \begin{bmatrix} \sqrt{\frac{k'_{z,II}}{k'_{z,I}}} & 0 \\ 0 & \sqrt{\frac{k'_{z,I}}{k'_{z,II}}} \end{bmatrix}. \quad (2.63)$$

Then, from Eqns. 2.47, 2.51, 2.57 and 2.63, the local boundary condition for the entire surface is written in the local B operator form:

$$\mathbf{B}^{\text{LPIA}} = \mathbf{Y}^{\text{out}} \mathbf{C}_t^{\text{Ideal}} \mathbf{Y}^{\text{loc}}, \quad (2.64)$$

which can be calculated straightforwardly by numerical computation.

Then the general equations are applied to the case that the input field is on-axis propagating along  $z$  direction with  $k_x = 0$  and  $k_y = 0$ . It can be described by  $\mathbf{E}^{\text{inc}} = [E_x^{\text{inc}}, E_y^{\text{inc}}, 0]^T$  focused by an aplanatic lens which satisfies the sine condition [66]. In the case that the fictitious surface is spherical, with the output a spherical field convergent to the center point of the Gaussian reference sphere, the transmission coefficients are calculated as follows:

$$\mathbf{C}_t^{\text{Ideal}} = \begin{bmatrix} \sqrt{\frac{1}{\cos\theta}} & 0 \\ 0 & \sqrt{\cos\theta} \end{bmatrix}. \quad (2.65)$$

Then, Eq. 2.49 is simplified according to this specific case that input field is on-axis propagating along  $z$  direction with  $k_x = 0$  and  $k_y = 0$ . Therefore, Eq. 2.49 becomes:

$$\mathbf{Y}^{\text{loc}} = \begin{bmatrix} q_{11} & q_{12} \\ q_{21} & q_{22} \end{bmatrix}. \quad (2.66)$$

For the output field at the Gaussian reference sphere, it propagates along  $\hat{r}$ , i.e. along  $z'$  axis in the local coordinates. Therefore,  $k'_x = 0$  and  $k'_y = 0$  are used to simplify Eq. 2.52 as:

$$\mathbf{Y}^{\text{out}} = \begin{bmatrix} q_{11} & q_{21} \\ q_{12} & q_{22} \end{bmatrix}. \quad (2.67)$$

Inserting Eq. 2.67, Eq. 2.66 and Eq. 2.65 to Eq. 2.64, then combining with Eq. 2.45, the B operator for the aplanatic lens is obtained as:

$$\mathcal{B}^{\text{LPIA}} = \frac{\sqrt{\cos\theta}}{2} \begin{bmatrix} c_1 + c_2 \cos 2\phi & c_2 \sin 2\phi \\ c_2 \sin 2\phi & c_1 - c_2 \cos 2\phi \end{bmatrix}, \quad (2.68)$$

where  $c_1 = \cos\theta + 1$ ,  $c_2 = \cos\theta - 1$ . Finally the consistent results with Eq. 12 in [66] is obtained as:

$$\mathbf{E}_{\perp}^{\text{outc}} = \frac{\sqrt{\cos\theta}}{2} \begin{bmatrix} E_x^{\text{inc}}(c_1 + c_2 \cos 2\phi) + E_y^{\text{inc}}(c_2 \sin 2\phi) \\ E_x^{\text{inc}}(c_2 \sin 2\phi) + E_y^{\text{inc}}(c_1 - c_2 \cos 2\phi) \end{bmatrix}. \quad (2.69)$$

But the derivation is different; especially the derivation of the transmission coefficients is more straightforward here. The so-called apodization factor  $\sqrt{\cos\theta}$  [66, 110] is included in the transmission coefficients directly.

## 2.3 OPERATOR FOR MICRO-/NANO-STRUCTURES

### 2.3.1 Introduction

Since it is already mentioned in chapter 1, micro-/nano-structures are essential for the microscopy system. In order to model the micro-/nano-structures rigorously with inclusion of the fully vectorial effect, rigorous Maxwell's equations solvers should be applied. There are many rigorous numerical solvers developed accompanying the development of computers. The following lists some as examples which are very often applied.

Finite Different Time Domain(FDTD) [111–114] method solves Maxwell's equations in time-domain. The time-dependent equations are discretized by central difference approximation both for the time and space partial derivatives. The electric field in a spatial volume is solved at a given time. Then, the magnetic field in the same spatial volume is solved at the next time interval. The process is repeated till all the require space is covered. It is widely used in the nanooptics community and lots of commercial softwares are based on FDTD, e.g. Lumerical FDTD [115], CST [116], etc.

Finite Element Method (FEM) [117–120] is a general numerical method which solves the partial differential equations rigorously. It can be applied in the areas of electromagnetic field, acoustic, fluid dynamic, heat, thermodynamics, etc. For solving Maxwell's equations, it discretizes the structure by meshes. And the electric field is approximated by a sum of the basis functions locally. By satisfying the local boundary condition, a linear equation systems are solved numerically. It is widely used in nanooptics community. Lots of commercial softwares are available, e.g. Comsol [121], JCMSuite [122], etc.

Volume Integral Method (VIM) [123–125] solves the volume integral equation, which

is derived from Maxwell's equations rigorously, based on Green's theorem. Integral Method(IM) [93, 126–130] solves the surface integral equation, which is derived from Maxwell's equations rigorously, based on Green's theorem. There are several commercial softwares available, e.g. PCGrate [131], WIAS-DiPoG [132].

Fourier Modal Method (FMM) [93, 123], which is also referred to Rigorous Coupled Wave Analysis (RCWA), is another rigorous Maxwell's equations solver. It discretizes the arbitrary structure into layers and represents the field in different layers in Fourier modes. By matching the boundary condition, the coefficients of the Fourier modes are calculated. There are lots of commercial softwares which are based on FMM, e.g. VirtualLab Fusion [133], Gsolver [134], RSoft [135].

Each of the above mentioned rigorous solvers has its pros and cons. The comparison of different rigorous solvers for simulation of a metallic slit is performed in [123]. More comparison of FEM, IM and FMM will be performed in chapter 3. In principle, all the rigorous solvers can be applied to obtain the B operator. But because of the good performance for lamellar structure, the widely acceptance in the community and the easy implementation, in this thesis, FMM is chosen to obtain the B operator.

FMM was first developed in the late 70s and early 80s by Knop [136], Moharam and Gaylord [137, 138]. It was later extended to three dimensional case and anisotropic medium [139–143]. Nearly parallel in time, it was extended to conical mounting [144] and arbitrary-shaped structure [145–147] based on the so-called Scattering (S) matrix [148–150] and the so-called R matrix [149, 151], later based on the so-called enhanced transmission matrix [152, 153]. In the meanwhile, a stable and efficient implementation was proposed by Morharam et al. [154, 155]. Lots of effort was used to improve the convergence for the TM case [156–159]. Li gave a deep mathematical background which is often referred to Li's rules [158] or inverse rule or fast Fourier factorization [160]. Later on, Lalanne et al. [100, 161, 162] applied Perfectly Matched Layers (PMLs) [163, 164] to extend FMM to model aperiodic structure. The algorithm is often referred to as Aperiodic Fourier Modal Method (AFMM). Later it was extended for arbitrary incident angle based on the so-called Contrast Field Formulation [165–167]. It was also extended to curvilinear coordinates to improve the computational speed [168, 169]. The staircase-approximation-convergence problem was addressed by Popov et al. [170] which is still a non-solved problem to the best of the author's knowledge. As time went by, there were still improvement added to FMM. Schuster et al. improved the convergence for crossed grating with so-called normal vector method [171]. Bai et al. improved the computational speed for certain types of crossed grating by applying group-theoretic approach [172–174]. Non-linear effect of second harmonic generation was implemented in the framework of FMM [175, 176]. Adaptive spatial resolution was introduced to FMM to improve the convergence performance [177–181]. General wave incidence was also addressed and applied [46, 105, 182, 183].

In this section, the author will write the B-operator matrix (B matrix) in the framework of FMM and AFMM based on the S matrix algorithm [150] to fit the framework of field tracing. The eigenvalue problem is modified to be formulated in general, including planar stratified medium, for easy implementation.

This section is organized as follows: In subsection 2.3.2, the 2D periodic structure is modeled with B operator in the framework of FMM. Due to the analogy of the peri-

odic and aperiodic structure, the 3D periodic structure is omitted. In subsection 2.3.3, the 3D case for aperiodic structure is modeled with B operator in the framework of AFMM. For the same reason of the analogy of the periodic and aperiodic structure, the 2D-aperiodic-structure case is omitted.

### 2.3.2 Periodic structure by Fourier modal method

#### 2.3.2.1 Discretization of arbitrary structure in layers

As mentioned before, only 2D structure is considered in this section. The arbitrary 2D structure is sliced into layers. For each layer, the structure is  $z$ -invariant as shown in Fig. 7. The thickness of the each layer is arbitrary. In Fig. 7, several simple structures are listed. They are gratings, grating with planar coatings etc.

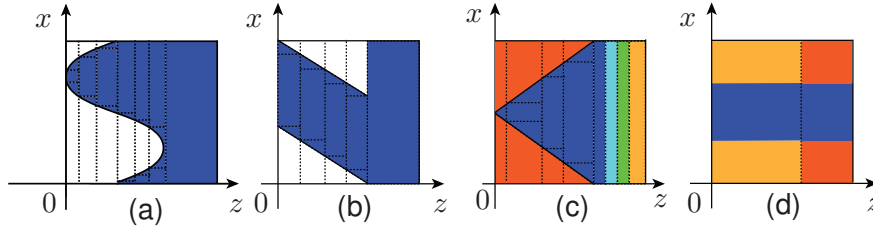


Figure 7: Various types of arbitrary structures. (a). Sinusoidal grating with a homogeneous substrate. (b). Slanted grating with a homogeneous substrate. (c). Triangular grating with planar coating layers. (d). Rectangular grating with inhomogeneous substrate.

#### 2.3.2.2 Field solutions in each layer

The structure is assumed to be non-magnetic, isotropic. And as mentioned in Sec. 2.1, the field is assumed time-harmonic. Therefore, the electromagnetic field in each layer, e.g. layer  $l$ , is governed by the following Maxwell's equations in frequency domain.

$$\nabla \times \mathbf{E}(\mathbf{r}) = i\omega\mu_0\mathbf{H}(\mathbf{r}), \quad (2.70a)$$

$$\nabla \times \mathbf{H}(\mathbf{r}) = -i\omega\epsilon(\mathbf{r})\mathbf{E}(\mathbf{r}), \quad (2.70b)$$

where  $\epsilon = \epsilon_0\epsilon_r$  is the permittivity of the structure. Please note that the layer index  $l$  is omitted in the notation for clearness.

Expanding Eq. 2.70a, the following equations are obtained as:

$$\frac{\partial E_z(\mathbf{r})}{\partial y} - \frac{\partial E_y(\mathbf{r})}{\partial z} = i\omega\mu_0 H_x(\mathbf{r}), \quad (2.71a)$$

$$\frac{\partial E_x(\mathbf{r})}{\partial z} - \frac{\partial E_z(\mathbf{r})}{\partial x} = i\omega\mu_0 H_y(\mathbf{r}), \quad (2.71b)$$

$$\frac{\partial E_y(\mathbf{r})}{\partial x} - \frac{\partial E_x(\mathbf{r})}{\partial y} = i\omega\mu_0 H_z(\mathbf{r}). \quad (2.71c)$$

From Eq. 2.70b, the following equations obtained analogously as:

$$\frac{\partial H_z(\mathbf{r})}{\partial y} - \frac{\partial H_y(\mathbf{r})}{\partial z} = -i\omega\epsilon_0\epsilon_r(\mathbf{r})E_x(\mathbf{r}), \quad (2.72a)$$

$$\frac{\partial H_x(\mathbf{r})}{\partial z} - \frac{\partial H_z(\mathbf{r})}{\partial x} = -i\omega\epsilon_0\epsilon_r(\mathbf{r})E_y(\mathbf{r}), \quad (2.72b)$$

$$\frac{\partial H_y(\mathbf{r})}{\partial x} - \frac{\partial H_x(\mathbf{r})}{\partial y} = -i\omega\epsilon_0\epsilon_r(\mathbf{r})E_z(\mathbf{r}). \quad (2.72c)$$

They are six differential equations where the six components of the electromagnetic fields are coupled. The structure is assumed to be 2D, e.g.  $y$ -invariant. The electromagnetic field is also assumed to be 2D which is the same  $y$ -invariant as the structure. In mathematics, it is written as:

$$\mathbf{E}(\mathbf{r}) = \mathbf{E}(x, z), \quad (2.73a)$$

$$\mathbf{H}(\mathbf{r}) = \mathbf{H}(x, z), \quad (2.73b)$$

$$\epsilon_r(\mathbf{r}) = \epsilon_r(x, z). \quad (2.73c)$$

Then, it is concluded that all the partial differential part with  $y$  are zero. The equations are obtained from Eq. 2.71b, 2.72a and 2.72c as:

$$\frac{\partial E_x(x, z)}{\partial z} - \frac{\partial E_z(x, z)}{\partial x} = i\omega\mu_0 H_y(x, z), \quad (2.74a)$$

$$-\frac{\partial H_y(x, z)}{\partial z} = -i\omega\epsilon_0\epsilon_r(x, z)E_x(x, z), \quad (2.74b)$$

$$\frac{\partial H_y(x, z)}{\partial x} = -i\omega\epsilon_0\epsilon_r(x, z)E_z(x, z). \quad (2.74c)$$

Analogously, following equations from Eq. 2.71a, 2.71c and 2.72b are obtained as:

$$-\frac{\partial E_y(x, z)}{\partial z} = i\omega\mu_0 H_x(x, z), \quad (2.75a)$$

$$\frac{\partial E_y(x, z)}{\partial x} = i\omega\mu_0 H_z(x, z), \quad (2.75b)$$

$$\frac{\partial H_x(x, z)}{\partial z} - \frac{\partial H_z(x, z)}{\partial x} = -i\omega\epsilon_0\epsilon_r(x, z)E_y(x, z). \quad (2.75c)$$

From the above two sets equations, it is known that they are totally decoupled. Eq. 2.74 is called Transverse Magnetic (TM) case because the magnetic field is transverse which means  $H_y$  is along the invariant direction of the structure as indicated in Fig. 8 (b). The magnetic field only has  $H_y$  component. The electric field has  $E_x$  and  $E_z$  components in general. Analogously, Eq. 2.75 is called Transverse Electric (TE) case because the electric field is transverse as indicated in Fig. 8 (a).  $E_y$  is along the invariant direction of the structure. The electric field only has  $E_y$  component. The magnetic field has  $H_x$  and  $H_z$  components in general. Note that TE- and TM-field decomposition only exists in the case where the structure and the field are both 2D.

Next, TE and TM field are treated separately. TE case is simpler than TM case in the for-



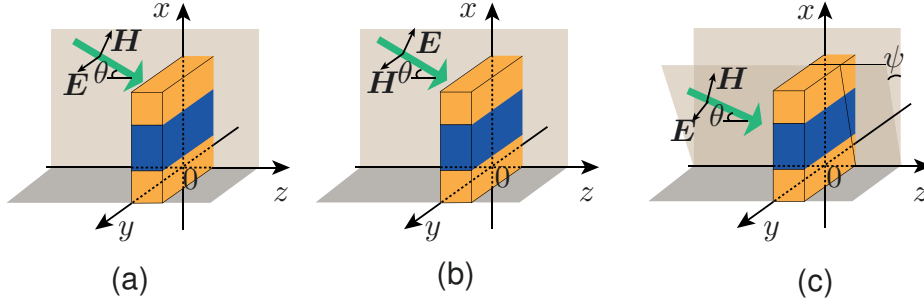


Figure 8: TE, TM and conical cases. (a). TE case means the structure and electric field are both  $y$ -invariant. (b). TM case means the structure and magnetic field are both  $y$ -invariant. (c). Conical case means the structure is  $y$ -invariant. The electromagnetic field is in arbitrary direction.

mulation. Therefore, TE case is formulated first. Substituting  $\omega = \frac{k_0}{\sqrt{\epsilon_0 \mu_0}}$  and eliminate  $H_z(x, z)$ , the following equation is obtained from Eq. 2.75 as:

$$H_x(x, z) = \frac{i}{k_0} \sqrt{\frac{\epsilon_0}{\mu_0}} \frac{\partial E_y(x, z)}{\partial z}, \quad (2.76a)$$

$$\frac{\partial H_x(x, z)}{\partial z} - \frac{i}{k_0} \sqrt{\frac{\epsilon_0}{\mu_0}} \frac{\partial^2 E_y(x, z)}{\partial x^2} = -\frac{i}{k_0} \sqrt{\frac{\epsilon_0}{\mu_0}} \epsilon_r(x, z) E_y(x, z). \quad (2.76b)$$

Eliminating  $H_x(x, z)$ , it is obtained as:

$$\frac{\partial^2 E_y(x, z)}{\partial z^2} + \frac{\partial^2 E_y(x, z)}{\partial x^2} + k_0^2 \epsilon_r(x, z) E_y(x, z) = 0. \quad (2.77)$$

It is the second order partial differential equation. In order to get rid of the derivatives. The Fourier transformations are performed to the electric field and the structure which is represented by the relative permittivity written as:

$$E_y(x, z) = \int \tilde{E}_y(z, k_x) \exp(-ik_x x) dk_x, \quad (2.78a)$$

$$\epsilon_r(x, z) = \int \tilde{\epsilon}_r(z, k_x) \exp(-ik_x x) dk_x. \quad (2.78b)$$

Inserting Eq. 2.78 to Eq. 2.77, the following equation is obtained with the help of convolution theory:

$$\begin{aligned} \frac{d^2}{dz^2} \int \tilde{E}_y(z, k_x) \exp(-ik_x x) dk_x - k_x^2 \int \tilde{E}_y(z, k_x) \exp(-ik_x x) dk_x \\ = -k_0^2 \int \int \tilde{\epsilon}_r(z, (k_x - k'_x)) \tilde{E}_y(z, k'_x) dk'_x \exp(-ik_x x) dk_x. \end{aligned} \quad (2.79)$$

The second order partial differential equation becomes second order differential equation. The above equation is satisfied to every  $k_x$ . Therefore, the kernel is taken out of the integral as:

$$\frac{d}{dz^2} \tilde{E}_y(z, k_x) = k_x^2 \tilde{E}_y(z, k_x) - k_0^2 \int \tilde{\epsilon}_r(z, (k_x - k'_x)) \tilde{E}_y(z, k'_x) dk'_x. \quad (2.80)$$

It is the couple-wave equations where the fields with different spatial frequencies are coupled with each other by the convolution with the structure. In order to perform the numerical computation, discretization must be performed. For the periodic structure,  $\epsilon_r(x, z)$  is periodic function in  $x$ -direction which means:

$$\epsilon_r(x, z) = \epsilon_r(x + d, z), \quad (2.81)$$

where  $d$  is the grating period. It is discretized in Fourier domain with the sampling distance  $\delta k = \frac{2\pi}{d}$ . According to Floquet's or Bloch's theorem, the field is also periodic. It is sampled with the same sampling distance as the structure. Therefore,  $k_x$  can be written in the discretized form as

$$k_{xn} = k_{x0} + n \cdot \delta k. \quad (2.82)$$

Eq. 2.80 is discretized as:

$$\frac{d}{dz^2} \tilde{E}_y(z, k_{xn}) = k_{xn}^2 \tilde{E}_y(z, k_{xn}) - k_0^2 \sum_{m=-\infty}^{\infty} \tilde{\epsilon}_r(z, (k_{xn} - k_{xm})) \tilde{E}_y(z, k_{xm}). \quad (2.83)$$

It is written in compact matrix form as:

$$\frac{d\tilde{\mathbf{E}}_y(z)}{dz^2} = [\mathbf{K}_x^2 - k_0^2 \tilde{\epsilon}_r(z)] \tilde{\mathbf{E}}_y(z), \quad (2.84)$$

where  $\tilde{\mathbf{E}}_y(z)$  is the vector contains all the spatial frequencies components.  $\mathbf{K}_x$  is the diagonal matrix which has  $k_{xn}$  in its diagonal.  $\tilde{\epsilon}_r(z)$  is the Toeplitz matrix related to the permittivity.

In order to transform the above equation to be second order ordinary differential equation,  $\tilde{\epsilon}_r(z)$  must be  $z$ -independent which means the structure must be  $z$ -invariant. It is the reason why the arbitrary structure must be sliced into layers which is  $z$ -invariant. Therefore, it is obtained as:

$$\frac{d\tilde{\mathbf{E}}_y(z)}{dz^2} = [\mathbf{K}_x^2 - k_0^2 \tilde{\epsilon}_r] \tilde{\mathbf{E}}_y(z). \quad (2.85)$$

For each of the spatial-frequency component of  $\tilde{\mathbf{E}}_y(z, k_x)$  with  $k_{xn}$ , the eigen solution is assumed as:

$$\tilde{E}_y(z, k_{xn}) = \sum_{i=-N}^N \omega_{n,i} \exp(q_i z) c_i, \quad (2.86)$$

where  $2N + 1$  is the number of the truncation orders or sampling points for numerical computation. It is written in matrix form as:

$$\tilde{\mathbf{E}}_y(z, k_x) = \mathbf{W} \exp(\mathbf{Q}z) \mathbf{c}. \quad (2.87)$$

Substituting Eq. 2.87 into 2.85, the eigenvalue problem in linear algebra is obtained as:

$$\mathbf{Q}^2 \mathbf{W} = [(\mathbf{K}_x)^2 - k_0^2 \tilde{\epsilon}_r] \mathbf{W}. \quad (2.88)$$

Then the eigenvalue problem is solved for  $[(\mathbf{K}_x)^2 - k_0^2 \tilde{\epsilon}_r]$ . There are two separated cases. First, if the structure is homogeneous which means  $\epsilon_r$  is constant, the eigenvalues of the

matrix is the elements of the diagonal. The eigenvectors of the matrix is identity matrix. In other words, the eigenvalue problem can be solved analytically. This case presents the modeling of the planar coating in physical sense. Second, if the structure is inhomogenous which means  $\epsilon_r$  is a function of space, the eigenvalue problem is calculated numerically, e.g. by the software package from CenterSpace [184]. The complexity of this process is  $\mathcal{O}(2N+1)^3$  which is the most computational expensive part of FMM. The square root of eigenvalue has two values which represent two propagating directions, namely the forward propagating direction  $+z$  and the backward propagating direction  $-z$ . Therefore, the electric field is the sum of the two direction propagating field. Neglecting the gain field which is non-physical, it is obtained as:

$$\tilde{E}_y(z) = \mathbf{W}_{\text{TE}} [\exp(-\mathbf{Q}_{\text{TE}}(z - h_{l-1}))\mathbf{c}_{\text{TE}}^+ + \exp(\mathbf{Q}_{\text{TE}}(z - h_l))\mathbf{c}_{\text{TE}}^-], \quad (2.89)$$

where  $h_{l-1}$  and  $h_l$  are the position of the left and right boundaries of the layer respectively as shown in Fig. 9. From Eq. 2.76a, the magnetic field is calculated as:

$$\tilde{H}_x(z, k_x) = \frac{i}{k_0} \sqrt{\frac{\epsilon_0}{\mu_0}} \frac{d\tilde{E}_y(z, k_x)}{dz}, \quad (2.90)$$

where  $\tilde{H}_x(z, k_x)$  is the Fourier coefficients in matrix form of the  $H_x(x, z)$ . Then it is obtained as:

$$\tilde{H}_x(z) = \frac{i}{k_0} \sqrt{\frac{\epsilon_0}{\mu_0}} \mathbf{W}_{\text{TE}} \mathbf{Q}_{\text{TE}} [-\exp(-\mathbf{Q}_{\text{TE}}(z - h_{l-1}))\mathbf{c}_{\text{TE}}^+ + \exp(\mathbf{Q}_{\text{TE}}(z - h_l))\mathbf{c}_{\text{TE}}^-]. \quad (2.91)$$

To this point, the field solutions in the TE case are obtained. Next, the coupled-wave equation in TM case as indicated in Fig. 8 (b) can be derived analogously:

$$\frac{d\tilde{H}_y(z)}{dz^2} = \tilde{\eta}^{-1} [(\mathbf{K}_x \tilde{\eta} \mathbf{K}_x) - k_0^2 \mathbf{I}] \tilde{H}_y(z), \quad (2.92)$$

where  $\tilde{\eta}$  is the Teoplitz matrix with the elements related to  $\tilde{\eta}$ .  $\mathbf{I}$  is identity matrix. Then the inverse rule which is also referred to as Li's rule [149, 156] is applied. It means  $\tilde{\eta}$  is replaces by  $\tilde{\epsilon}_r^{-1}$  to improve the convergence speed.

Eq. 2.92 is reformulated as:

$$\frac{d\tilde{H}_y(z)}{dz^2} = \tilde{\eta}^{-1} [(\mathbf{K}_x \tilde{\epsilon}_r^{-1} \mathbf{K}_x) - k_0^2 \mathbf{I}] \tilde{H}_y(z). \quad (2.93)$$

Totally analogous to TE case, the field solutions is obtained as:

$$\tilde{H}_y(z) = \mathbf{W}_{\text{TM}} [\exp(-\mathbf{Q}_{\text{TM}}(z - h_{l-1}))\mathbf{c}_{\text{TM}}^+ + \exp(\mathbf{Q}_{\text{TM}}(z - h_l))\mathbf{c}_{\text{TM}}^-], \quad (2.94a)$$

$$\tilde{E}_x(z) = \frac{1}{k_0} \sqrt{\frac{\mu_0}{\epsilon_0}} \tilde{\eta} \mathbf{W}_{\text{TM}} \mathbf{Q}_{\text{TM}} [-\exp(-\mathbf{Q}_{\text{TM}}(z - h_{l-1}))\mathbf{c}_{\text{TM}}^+ + \exp(\mathbf{Q}_{\text{TM}}(z - h_l))\mathbf{c}_{\text{TM}}^-]. \quad (2.94b)$$

The conical case as indicated in Fig. 8 (c) can be derived analogously to TE and TM case. The derivation is omitted here for brevity.

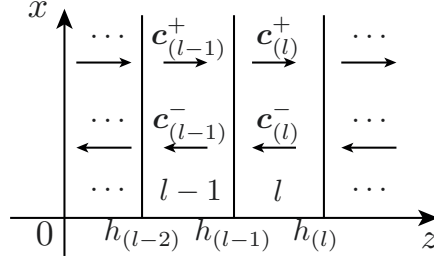


Figure 9: Demonstration of the boundary condition at the boundary  $z = h_{(l-1)}$  between the field in layer  $l - 1$  and  $l$ .

### 2.3.2.3 Boundary conditions

The field solution for TE, TM and conical incidence are obtained above in one specific layer  $l$ . Therefore, the field solution in the layer  $l - 1$  is obtained directly. TE-polarization case is taken for example for further demonstration, the fields in layer  $l - 1$  is obtained from Eq. 2.89 and Eq. 2.91 as:

$$\tilde{E}_{y(l-1)}(z) = W_{\text{TE}(l-1)} \left[ \exp(-Q_{\text{TE}(l-1)}(z - h_{(l-2)})) c_{\text{TE}(l-1)}^+ + \exp(Q_{\text{TE}(l-1)}(z - h_{(l-1)})) c_{\text{TE}(l-1)}^- \right], \quad (2.95a)$$

$$\tilde{H}_{x(l-1)}(z) = -\frac{i}{k_0} \sqrt{\frac{\epsilon_0}{\mu_0}} W_{\text{TE}(l-1)} Q_{\text{TE}(l-1)} \left[ -\exp(-Q_{\text{TE}(l-1)}(z - h_{(l-2)})) c_{\text{TE}(l-1)}^+ + \exp(Q_{\text{TE}(l-1)}(z - h_{(l-1)})) c_{\text{TE}(l-1)}^- \right]. \quad (2.95b)$$

The transverse components of the electromagnetic fields are continuous at the boundary at  $z = h_{(l-1)}$  shown in Fig. 9 as:

$$\tilde{E}_{y(l-1)}(z = h_{(l-1)}) = \tilde{E}_{y(l)}(z = h_{(l-1)}), \quad (2.96a)$$

$$\tilde{H}_{x(l-1)}(z = h_{(l-1)}) = \tilde{H}_{x(l)}(z = h_{(l-1)}). \quad (2.96b)$$

Then it is obtained as:

$$\begin{bmatrix} W_{\text{TE}(l-1)} X_{\text{TE}(l-1)} & W_{\text{TE}(l-1)} \\ V_{\text{TE}(l-1)} X_{\text{TE}(l-1)} & -V_{\text{TE}(l-1)} \end{bmatrix} \begin{bmatrix} c_{\text{TE}(l-1)}^+ \\ c_{\text{TE}(l-1)}^- \end{bmatrix} = \begin{bmatrix} W_{\text{TE}(l)} & W_{\text{TE}(l)} X_{\text{TE}(l)} \\ V_{\text{TE}(l)} & -V_{\text{TE}(l)} X_{\text{TE}(l)} \end{bmatrix} \begin{bmatrix} c_{\text{TE}(l)}^+ \\ c_{\text{TE}(l)}^- \end{bmatrix}, \quad (2.97)$$

where  $X_{\text{TE}(l)} = \exp(Q_{\text{TE}(l)}(h_{(l-1)} - h_{(l)}))$  is related to the propagation kernel in Fourier domain in layer  $l$ .  $X_{\text{TE}(l-1)} = \exp(-Q_{\text{TE}(l-1)}(h_{(l-1)} - h_{(l-2)}))$  is related to the propagation kernel in Fourier domain in layer  $l - 1$ .  $V_{\text{TE}(l)}$  and  $V_{\text{TE}(l-1)}$  is calculated by the following equations:

$$V_{\text{TE}(l)} = -W_{\text{TE}(l)} Q_{\text{TE}(l)}, \quad (2.98a)$$

$$V_{\text{TE}(l-1)} = -W_{\text{TE}(l-1)} Q_{\text{TE}(l-1)}. \quad (2.98b)$$

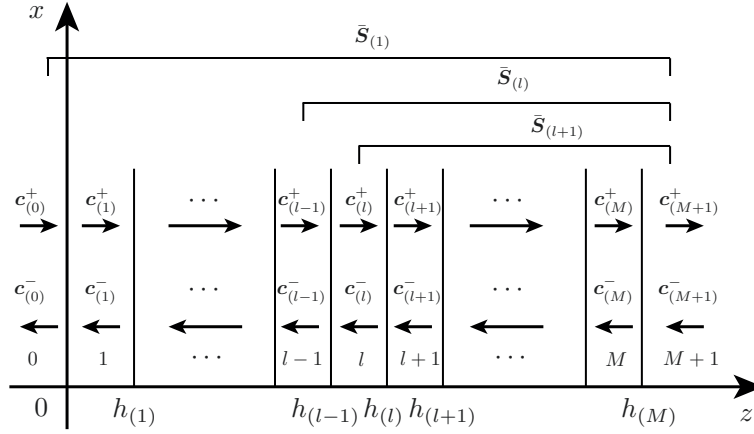


Figure 10: The demonstration of the S matrix.  $\bar{S}_{(l)}$ ,  $\bar{S}_{(l+1)}$  and  $\bar{S}_{(1)}$  are the accumulated S matrices till boundaries at  $h_{l+1}$ ,  $h_l$  and  $h_1$  respectively.

#### 2.3.2.4 From S matrix to B matrix

Scattering (S) matrix is well known to deal with the stratified media by propagating the modes through the layers stably [150]. But in order to propagate the transverse field components, a minor modification is done to S matrix which results in B operator matrix, which is denoted by B matrix for short. Because of the analogy between TE, TM and conical incidence, the TE case is taken for example here.

The derivation is taken analogous to the procedure which is detailed formulated in [166]. Therefore, the accumulated S matrix, as indicated in Fig. 10, is directly written here as:

$$\begin{bmatrix} c_{\text{TE}(0)}^- \\ c_{\text{TE}(M+1)}^+ \end{bmatrix} = \begin{bmatrix} \bar{S}_{(1)}^{11} & \bar{S}_{(1)}^{12} \\ \bar{S}_{(1)}^{21} & \bar{S}_{(1)}^{22} \end{bmatrix} \begin{bmatrix} c_{\text{TE}(M+1)}^- \\ c_{\text{TE}(0)}^+ \end{bmatrix}. \quad (2.99)$$

The conversion of the S matrix to B matrix is performed in the form of:

$$\begin{bmatrix} \tilde{E}_{y(0)}^- \\ \tilde{E}_{y(M+1)}^+ \end{bmatrix} = \begin{bmatrix} \tilde{\mathcal{B}}_{(1)}^{11} & \tilde{\mathcal{B}}_{(1)}^{12} \\ \tilde{\mathcal{B}}_{(1)}^{21} & \tilde{\mathcal{B}}_{(1)}^{22} \end{bmatrix} \begin{bmatrix} \tilde{E}_{y(M+1)}^- \\ \tilde{E}_{y(0)}^+ \end{bmatrix}, \quad (2.100)$$

where

$$\tilde{\mathcal{B}}_{(1)}^{11} = \mathbf{W}_{\text{TE}(0)} \bar{S}_{(1)}^{11} \mathbf{W}_{\text{TE}(M+1)}, \quad (2.101a)$$

$$\tilde{\mathcal{B}}_{(1)}^{12} = \mathbf{W}_{\text{TE}(0)} \bar{S}_{(1)}^{12} \mathbf{W}_{\text{TE}(0)}, \quad (2.101b)$$

$$\tilde{\mathcal{B}}_{(1)}^{21} = \mathbf{W}_{\text{TE}(M+1)} \bar{S}_{(1)}^{21} \mathbf{W}_{\text{TE}(M+1)}, \quad (2.101c)$$

$$\tilde{\mathcal{B}}_{(1)}^{22} = \mathbf{W}_{\text{TE}(M+1)} \bar{S}_{(1)}^{22} \mathbf{W}_{\text{TE}(0)}. \quad (2.101d)$$

The B matrix is the direct connection of the input field at input plane and output field at output plane in Fourier domain indicated by Eq. 2.100. Therefore, it is very straightforward to apply in the entire modeling. One only needs to find the corresponding element in B matrix and to multiply the specific element of the input field to calculate the specific element of the output field. Please note that the B matrix for ideal periodic

grating is directly calculated by the predefined diffraction efficiencies in Eq. 2.26. If the input field is equidistantly sampled in Fourier domain by  $\delta k$ , the corresponding elements in B matrix are obtained simultaneously for all of the input  $\kappa$  in one eigenvalue calculation. By doing this, the computational time is accelerated. If the input field is non-equidistantly sampled, one has to calculate the corresponding elements in B matrix each time for each input  $\kappa$  or the numerical tricks, e.g. interpolation and fitting, are applied for improving the computational speed.

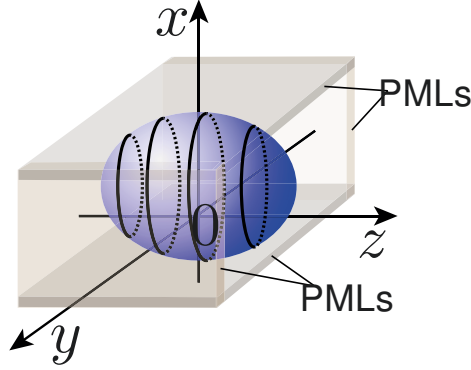


Figure 11: Schematic of the arbitrary 3D structure bounded by PMLs at the lateral sides. It is also sliced into layers with  $z$ -invariant.

### 2.3.3 Aperiodic structure by Fourier modal method

#### 2.3.3.1 Absorbing layers

The structure discussed in this subsection is aperiodic. Only the 3D case for aperiodic structure is considered for brevity. There is a natural connection between periodic and aperiodic structure. If the period of the periodic structure is large enough even to infinity, the interaction of the electromagnetic field between the neighboring period, which is also referred to aliasing, becomes minor even vanishes. Therefore, one can always deal with the aperiodic structure with the periodic theory with large enough period. It is often called super-cell approach [165]. However, this approach is not practical because of the very expensive numerical effort. In order to reduce the numerical effort, one has to reduce the period but in the same time to avoid the aliasing. Therefore, absorbing layers should be added at the lateral sides of the structure to absorb all the electromagnetic field which would interact with the neighboring period. In principle, any absorbing layers would work if it absorbs any electromagnetic field with any spectral frequency and incident angle. The so-called Perfectly Matched Layers (PMLs) [163] functions exactly this way. Therefore, by adding PMLs at the lateral sides, the theory which deals with the periodic structure can be directly used for the aperiodic structure [100, 165, 185, 186].

### 2.3.3.2 Discretization of arbitrary structure into layers

Analogous to the discretization of arbitrary 2D structure in subsection 2.3.2, the 3D structure as shown in Fig. 11 is discretized into layers in which the structure is z-invariant. The reason is the same as discussed in 2.3.2.

### 2.3.3.3 Field solutions in each layer

Because of the analogy to the periodic case, Eq. 2.71 and 2.72 are directly taken for further derivation.  $E_z(\mathbf{r})$  and  $H_z(\mathbf{r})$  are eliminated by substitution. The PMLs is implemented with the complex stretched coordinates [164, 165] at the lateral directions. Therefore, the following equation is obtained as:

$$\frac{\partial}{\partial z} E_x(\mathbf{r}) = i\omega\mu_0 H_y(\mathbf{r}) + \frac{1}{f'(x)} \frac{\partial}{\partial x} \left[ \frac{1}{i\omega\epsilon_0\epsilon_r(\mathbf{r})} \left( \frac{1}{f'(x)} \frac{\partial}{\partial x} H_y(\mathbf{r}) - \frac{1}{f'(y)} \frac{\partial}{\partial y} H_x(\mathbf{r}) \right) \right], \quad (2.102a)$$

$$\frac{\partial}{\partial z} E_y(\mathbf{r}) = -i\omega\mu_0 H_x(\mathbf{r}) + \frac{1}{f'(y)} \frac{\partial}{\partial y} \left[ \frac{1}{i\omega\epsilon_0\epsilon_r(\mathbf{r})} \left( \frac{1}{f'(x)} \frac{\partial}{\partial x} H_y(\mathbf{r}) - \frac{1}{f'(y)} \frac{\partial}{\partial y} H_x(\mathbf{r}) \right) \right], \quad (2.102b)$$

$$\frac{\partial}{\partial z} H_x(\mathbf{r}) = -i\omega\epsilon_0\epsilon_r(\mathbf{r}) E_y(\mathbf{r}) + \frac{1}{f'(x)} \frac{\partial}{\partial x} \left[ \frac{1}{i\omega\mu_0} \left( \frac{1}{f'(x)} \frac{\partial}{\partial x} E_y(\mathbf{r}) - \frac{1}{f'(y)} \frac{\partial}{\partial y} E_x(\mathbf{r}) \right) \right], \quad (2.102c)$$

$$\frac{\partial}{\partial z} H_y(\mathbf{r}) = i\omega\epsilon_0\epsilon_r(\mathbf{r}) E_x(\mathbf{r}) + \frac{1}{f'(y)} \frac{\partial}{\partial y} \left[ \frac{1}{i\omega\mu_0} \left( \frac{1}{f'(x)} \frac{\partial}{\partial x} E_y(\mathbf{r}) - \frac{1}{f'(y)} \frac{\partial}{\partial y} E_x(\mathbf{r}) \right) \right], \quad (2.102d)$$

where  $f(x)$  and  $f(y)$  are the functions related to PMLs which is give in the appendix A in [162].  $f'(x)$  and  $f'(y)$  are their first order derivatives as in Eq. 8 in [162]. Then the Fourier transforms of the related quantities are obtained as:

$$E_x(\mathbf{r}) = \frac{1}{2\pi} \iint \tilde{E}_x(z, \kappa) \exp[-i(k_x x + k_y y)] dk_x dk_y, \quad (2.103a)$$

$$E_y(\mathbf{r}) = \frac{1}{2\pi} \iint \tilde{E}_y(z, \kappa) \exp[-i(k_x x + k_y y)] dk_x dk_y, \quad (2.103b)$$

$$H_x(\mathbf{r}) = \frac{1}{2\pi} \iint \tilde{H}_x(z, \kappa) \exp[-i(k_x x + k_y y)] dk_x dk_y, \quad (2.103c)$$

$$H_y(\mathbf{r}) = \frac{1}{2\pi} \iint \tilde{H}_y(z, \kappa) \exp[-i(k_x x + k_y y)] dk_x dk_y, \quad (2.103d)$$

$$\epsilon_r(\mathbf{r}) = \frac{1}{2\pi} \iint \tilde{\epsilon}_r(z, \kappa) \exp[-i(k_x x + k_y y)] dk_x dk_y, \quad (2.103e)$$

$$\frac{1}{\epsilon_r(\mathbf{r})} = \frac{1}{2\pi} \iint \tilde{\eta}(z, \kappa) \exp[-i(k_x x + k_y y)] dk_x dk_y, \quad (2.103f)$$

$$\frac{1}{f'(x)} = \frac{1}{\sqrt{2\pi}} \int \tilde{f}_{p,x}(z, k_x) \exp(-ik_x x) dk_x, \quad (2.103g)$$

$$\frac{1}{f'(y)} = \frac{1}{\sqrt{2\pi}} \int \tilde{f}_{p,y}(z, k_y) \exp(-ik_y y) dk_y. \quad (2.103h)$$

Insert Eq. 2.103 into Eq. 2.102, perform the discretization and make the structure z-invariant analogously to the TE case for periodic structure, the results are written in matrix form as:

$$k_0 \frac{\partial}{\partial z} \begin{bmatrix} \tilde{E}_x(z) \\ \tilde{E}_y(z) \end{bmatrix} = \begin{bmatrix} -F_x K_x \hat{\eta} F_y K_y & F_x K_x \hat{\eta} F_x K_x - k_0^2 I \\ k_0^2 I - F_y K_y \hat{\eta} F_y K_y & -F_y K_y \hat{\eta} F_x K_x \end{bmatrix} \begin{bmatrix} i\sqrt{\frac{\mu_0}{\epsilon_0}} \tilde{H}_x(z) \\ i\sqrt{\frac{\mu_0}{\epsilon_0}} \tilde{H}_y(z) \end{bmatrix}, \quad (2.104a)$$

$$k_0 \frac{\partial}{\partial z} \begin{bmatrix} i\sqrt{\frac{\mu_0}{\epsilon_0}} \tilde{H}_x(z) \\ i\sqrt{\frac{\mu_0}{\epsilon_0}} \tilde{H}_y(z) \end{bmatrix} = \begin{bmatrix} -F_x K_x F_y K_y & -k_0^2 \tilde{\epsilon}_r + F_x K_x F_x K_x \\ k_0^2 \tilde{\epsilon}_r - F_y K_y F_y K_y & F_x K_x F_y K_y \end{bmatrix} \begin{bmatrix} \tilde{E}_x(z) \\ \tilde{E}_y(z) \end{bmatrix}. \quad (2.104b)$$

They are analogous to Eq. 2.84. They can be written in more compact form as:

$$k_0 \frac{\partial}{\partial z} \tilde{\mathbf{E}}(z) = \mathbf{A} \tilde{\mathbf{H}}(z), \quad (2.105a)$$

$$k_0 \frac{\partial}{\partial z} \tilde{\mathbf{H}}(z) = \mathbf{B} \tilde{\mathbf{E}}(z), \quad (2.105b)$$

where

$$\tilde{\mathbf{E}}(z) = \begin{bmatrix} \tilde{E}_x(z) \\ \tilde{E}_y(z) \end{bmatrix}, \quad (2.106a)$$

$$\tilde{\mathbf{H}}(z) = \begin{bmatrix} i\sqrt{\frac{\mu_0}{\epsilon_0}} \tilde{H}_x(z) \\ i\sqrt{\frac{\mu_0}{\epsilon_0}} \tilde{H}_y(z) \end{bmatrix}, \quad (2.106b)$$

$$\mathbf{A} = \begin{bmatrix} F_x K_x \tilde{\eta} F_y K_y & k_0^2 \mathbf{I} - F_x K_x \tilde{\eta} F_x K_x \\ -k_0^2 \mathbf{I} + F_y K_y \tilde{\eta} F_y K_y & -F_y K_y \tilde{\eta} F_x K_x \end{bmatrix}, \quad (2.106c)$$

$$\mathbf{B} = \begin{bmatrix} -F_x K_x F_y K_y & -k_0^2 \tilde{\mathbf{E}} + F_x K_x F_x K_x \\ k_0^2 \tilde{\mathbf{E}} - F_y K_y F_y K_y & F_x K_x F_y K_y \end{bmatrix}. \quad (2.106d)$$

Then, the ordinary differential equation is obtained as:

$$k_0^2 \frac{\partial^2}{\partial z^2} \tilde{\mathbf{E}} = \mathbf{A} \mathbf{B} \tilde{\mathbf{E}}. \quad (2.107)$$

By solving the eigenvalue problem, the electric field is expressed as:

$$\tilde{\mathbf{E}}(z) = \mathbf{W}_{3D} [\exp(-\mathbf{Q}_{3D}(z - h_{l-1})) \mathbf{c}_{3D}^+ + \exp(\mathbf{Q}_{3D}(z - h_l)) \mathbf{c}_{3D}^-], \quad (2.108)$$

with the help of Eq. 2.105a, the magnetic field is expressed as:

$$\tilde{\mathbf{H}}(z) = -k_0 \mathbf{A}^{-1} \mathbf{W}_{3D} \mathbf{Q}_{3D} [\exp(-\mathbf{Q}_{3D}(z - h_{l-1})) \mathbf{c}_{3D}^+ + \exp(\mathbf{Q}_{3D}(z - h_l)) \mathbf{c}_{3D}^-]. \quad (2.109)$$

Therefore, to this point, the electromagnetic field in a certain layer is obtained with the unknowns of the coefficients  $\mathbf{c}_{3D}^+$  and  $\mathbf{c}_{3D}^-$ .

#### 2.3.3.4 Boundary conditions

In order to calculate the unknowns, linear equations are formulated from the boundary condition which states that the transverse electromagnetic components are continuous at boundary  $z = h_{(l-1)}$  shown in Fig. 9. Totally analogous to Eq. 2.97, the following equation is obtained as:

$$\begin{bmatrix} \mathbf{W}_{3D(l-1)} \mathbf{X}_{3D(l-1)} & \mathbf{W}_{3D(l-1)} \\ \mathbf{V}_{3D(l-1)} \mathbf{X}_{3D(l-1)} & -\mathbf{V}_{3D(l-1)} \end{bmatrix} \begin{bmatrix} \mathbf{c}_{3D(l-1)}^+ \\ \mathbf{c}_{3D(l-1)}^- \end{bmatrix} = \begin{bmatrix} \mathbf{W}_{3D(l)} & \mathbf{W}_{3D(l)} \mathbf{X}_{3D(l)} \\ \mathbf{V}_{3D(l)} & -\mathbf{V}_{3D(l)} \mathbf{X}_{3D(l)} \end{bmatrix} \begin{bmatrix} \mathbf{c}_{3D(l)}^+ \\ \mathbf{c}_{3D(l)}^- \end{bmatrix}, \quad (2.110)$$

where  $\mathbf{X}_{3D(l)} = \exp(\mathbf{Q}_{3D(l)}(h_{(l-1)} - h_{(l)}))$  is related to the propagation kernel in Fourier domain in layer  $l$ .  $\mathbf{X}_{3D(l-1)} = \exp(-\mathbf{Q}_{3D(l-1)}(h_{(l-1)} - h_{(l-2)}))$  is related to the propagation kernel in Fourier domain in layer  $l-1$ .  $\mathbf{V}_{3D(l)}$  and  $\mathbf{V}_{3D(l-1)}$  is calculated by the following equations:

$$\mathbf{V}_{3D(l)} = -k_0 \mathbf{A}_{(l)}^{-1} \mathbf{W}_{3D(l)} \mathbf{Q}_{3D(l)}, \quad (2.111a)$$

$$\mathbf{V}_{3D(l-1)} = -k_0 \mathbf{A}_{(l-1)}^{-1} \mathbf{W}_{3D(l-1)} \mathbf{Q}_{3D(l-1)}. \quad (2.111b)$$



### 2.3.3.5 From S matrix to B matrix

For the same reason as mentioned before, the S matrix is written to B matrix. Analogous to the TE case before, the following equation analogous to Eq. 2.99 is directly written as:

$$\begin{bmatrix} c_{3D(0)}^- \\ c_{3D(M+1)}^+ \end{bmatrix} = \begin{bmatrix} \tilde{S}_{3D(1)}^{11} & \tilde{S}_{3D(1)}^{12} \\ \tilde{S}_{3D(1)}^{21} & \tilde{S}_{3D(1)}^{22} \end{bmatrix} \begin{bmatrix} c_{3D(M+1)}^- \\ c_{3D(0)}^+ \end{bmatrix}. \quad (2.112)$$

In order to convert the S matrix to B matrix as in Eq. 2.100, direct derivation is performed with the help of Eq. 2.108. The results are obtained as:

$$\tilde{\mathcal{B}}_{(1)}^{11} = W_{3D(0)} \tilde{S}_{3D(1)}^{11} W_{3D(M+1)} \quad (2.113a)$$

$$\tilde{\mathcal{B}}_{(1)}^{12} = W_{3D(0)} \tilde{S}_{3D(1)}^{12} W_{3D(0)}, \quad (2.113b)$$

$$\tilde{\mathcal{B}}_{(1)}^{21} = W_{3D(M+1)} \tilde{S}_{3D(1)}^{21} W_{3D(M+1)}, \quad (2.113c)$$

$$\tilde{\mathcal{B}}_{(1)}^{22} = W_{3D(M+1)} \tilde{S}_{3D(1)}^{22} W_{3D(0)}. \quad (2.113d)$$

The above B matrix is sampled in Fourier domain by the inverse of computational window size, which is relatively small. Therefore, the sampling is not fine enough in Fourier domain for some applications. In order to have a fine sampling, the so-called near field to near/far field transformation is applied as discussed in detail in [187].

## 2.4 SUMMARY AND CONCLUSION

In this chapter, the full theory is formulated. The LPIA for curved surfaces and FMM for micro-/nano-structures are the focus. All the field tracing techniques are implemented in the software VirtualLab Fusion [133] in which numerical experiments are performed in next chapters. The laptop used in this thesis has the property as: RAM: 16 GB , CPU: Intel Core i7 @2.4 GHz.

### 3.1 INTRODUCTION

The B operator for the real curved surfaces in the framework of the LPIA are formulated in details in Sec. 2.2. How accurate is it remains unknown. Especially for the reason that it is not derived from Maxwell's equations rigorously or with certain assumptions. Therefore, it is necessary to validate the B operator and evaluate the limitation of the it based on LPIA.

In [106], the authors compared the LPIA boundary condition combined with the Local Plane Wave Approximation (LPWA) free space propagation with the rigorous method for the triangular-shaped structure. But it suffers from the intrinsic drawback of the diffraction from the sharp edge. In [107], the authors show the high accuracy of the LPIA boundary condition combined with the LPWA free space propagation for the V-shaped structure even including evanescent wave. But the calculated coupling efficiencies between the LPIA and rigorous one is still observable because the influence of the diffraction of the sharp edge. What about the curved surface without the diffraction from the shape edge? In [96], the authors compared the LPIA boundary condition combined with LPWA free space propagation with rigorous method for curved surface which is sinusoidal. They showed good agreement for large period of structure but observe deviation for small period of structures. For the reason that LPIA local boundary condition and LPWA free space propagation are always considered being combined as a whole, the origin of the inaccuracy are not separately discussed for the LPIA local boundary condition and LPWA free space propagation.

As discussed in Sec. 2.2, the LPIA for the local boundary condition is separated from the free space propagation. The free space propagation can always performed rigorously. If the LPIA for the local boundary condition is accurate enough, the field at any plane should be accurate enough. It is only considered that the fields interacts with one boundary once in the deviation of B operator in Sec. 2.2. Therefore, it is named as LPIA of the first order. When LPIA boundary condition is talked about in the following, it always means LPIA of the first order unless it is emphasized as LPIA of higher orders which means the fields interacts with one boundary for multiple times. In the following section, the LPIA for real curved surface will be validated by comparing with the rigorous solution by FEM [93] in different types of a 2D single curved surface. And the limitation of the LPIA will be evaluated in the situation that higher orders of LPIA occur. The LPIA with combination of free space propagation will also be validated by comparing with FEM for 2D single curved surface. The results of FEM is obtained by the software JCMSuite [122]. The detail of the implementation of FEM is shown in [188, 189]. For evaluating the versatility, the results by LPIA for a 2D two-curved-surface component will also be validated, when the field is in the focal region propagating through the second curved surface with Wave Propagation Method (WPM) [190–193] shown in

the literature. For the practice usage, most components are 3D structured. Therefore, two different types of 3D lenses with LPIA combined with free space propagation are compared with the results from WPM in [193].

The B operator for the fictitious curved surface in the framework of the LPIA is also

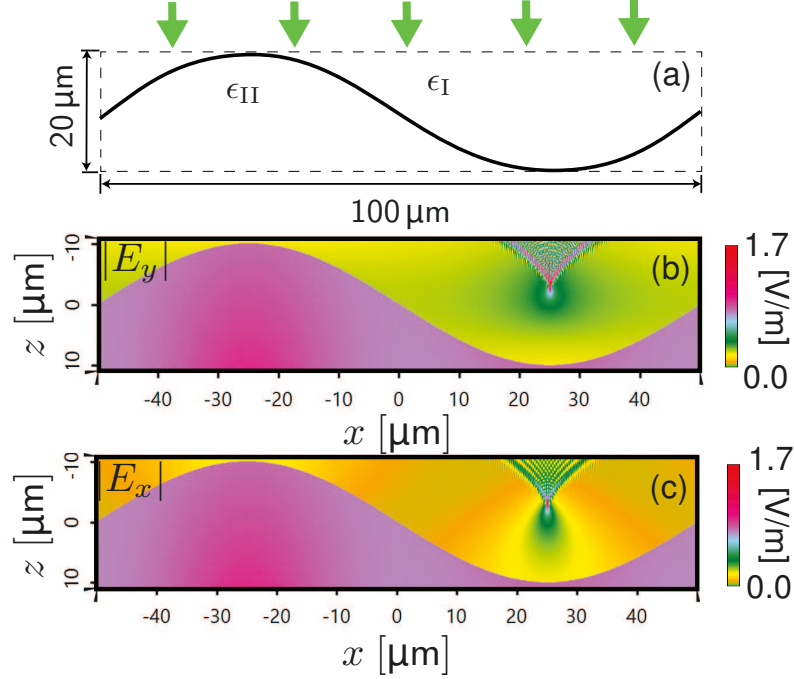


Figure 12: (a). Schematic of the structure: a sinusoidal surface with lateral size 100 μm and depth 20 μm. (b)-(c). The amplitudes of the electric field components are calculated by FEM. The incident field is not included in the region above the surface.

formulated in details in Sec. 2.2. Though the basic concept is the same with the ideal lens in [9, 62–64, 66, 69], the derivation is different. It is validated mathematically in Sec. 2.2. In this chapter, the numerical validation and evaluation will be performed to show its accuracy and versatility.

The result is compared with Debye-Wolf integral which calculates the field at the focal plane with plane wave incidence [66]. In addition, to show the versatility of the B operator for fictitious curved surfaces, the focused fields with rectangular and annular apertures are calculated and focusing of cylindrical vector beams [9, 69], e.g. radially and azimuthally polarized beams, are also performed.

The B operator for the micro-/nano-structures by FMM is formulated in details in Sec. 2.3. It is derived rigorously from Maxwell's equations mathematically. But the implementation is done numerically. Therefore, the validation should be performed by comparing with other rigorous methods to obtain convincing results for the application examples in this thesis. Besides the validation, the evaluation of the computational speed is also very important to show pros and cons compared to other methods in different cases.

The validation of FMM for periodic and aperiodic structure were already validated by

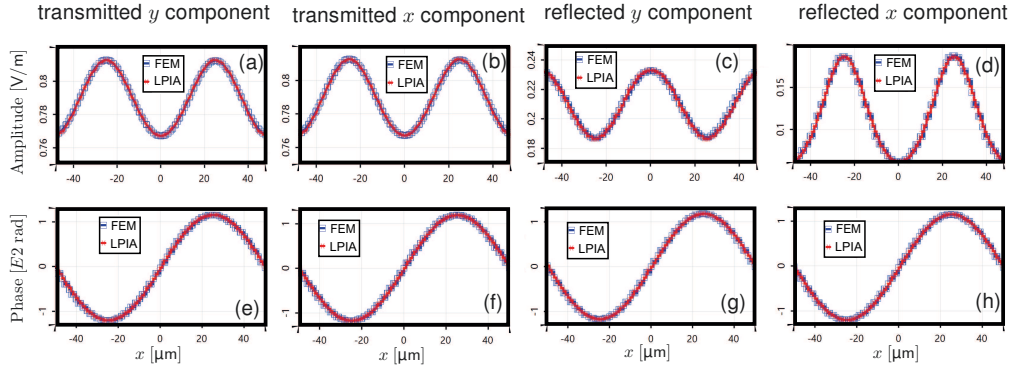


Figure 13: Comparison of field quantities on the curved surface obtained by LPIA and FEM. Please note that the phase is unwrapped one.

the authors by comparing the results with other methods, e.g. integral method(IM) [146], supercell approach [165], method of line [161]. The evaluation of the computational speed of FMM is performed by comparing other methods such as FEM, FDTD, volume integral method, etc. in [123]. But the structure is restricted to only the binary grating with metal as the material. Furthermore, the performance of different methods are performed by different computers. Therefore, the computational time does not reveal the computational speed directly.

Therefore, in Sec. 3.3, the results for different types of periodic structures with IM and FEM will be compared to evaluate the convergence and computational speed of FMM. The results of IM is obtained by the code from WIAS [132]. The detail of the implementation of IM is shown in [128]. The results of FEM is again obtained by the software JCMSuite [122]. Furthermore, all three methods are performed with the same laptop. Therefore, the computational time can directly reveal the computational speed. Even though FMM for aperiodic structure was already validated in the literature, the results with FEM for the 2D case as well as the 3D case are still compared briefly to validate the FMM code used in this thesis.

## 3.2 OPERATOR FOR CURVED SURFACES

### 3.2.1 Real curved surface

In the following numerical results for the real curved surfaces, the input fields are plane waves with wavelength  $\lambda = 532 \text{ nm}$ . The amplitudes of the incident plane waves are normalized. The permittivity of the input region, which is air, is  $\epsilon_I = 1$ . The permittivity of the output region, which is fused silica, is  $\epsilon_{II} = 2.135$ .

#### 3.2.1.1 Local boundary condition base on LPIA

In order to validate the local boundary condition by LPIA, three examples are studied numerically. The first one is the full sinusoidal surface with a relatively low ratio of

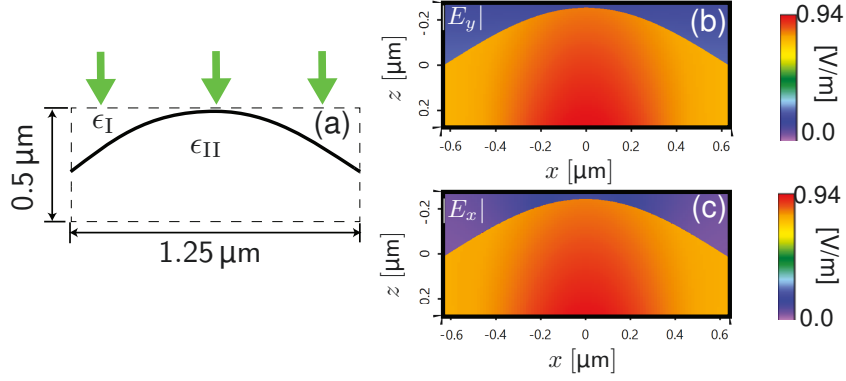


Figure 14: (a). Schematic of the structure: a half-sinusoidal surface with lateral size  $1.25 \mu\text{m}$  and depth  $0.25 \mu\text{m}$ . (b)-(c). The amplitudes of the electric field are calculated by FEM.

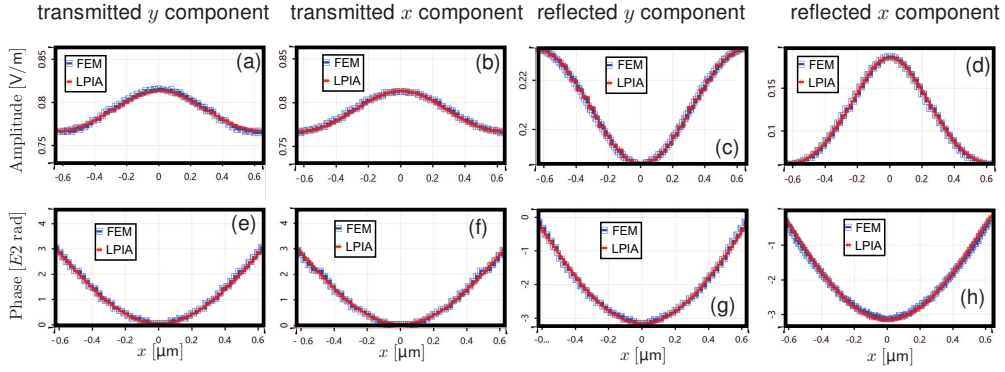


Figure 15: Comparison of field quantities on the curved surface obtained by LPIA and FEM corresponding to Fig. 14.

height to size but relatively large size. The second one is the half-sinusoidal surface with a relatively small size, even comparable to the wavelength. The third one is a half-sinusoidal surface with a relatively high ratio of height to size. In the first example, the reflected field at the output reference plane  $z = -10 \mu\text{m}$  is not in the homeomorphic zone [102], sometimes also referred to as geometric zone [103]. In the third example, the field at the output reference plane  $z = 0$  is not in the homeomorphic zone.

The incidence direction is normal incidence from above, inclined incidence will be considered later for the evaluation. Both TE and TM polarized fields are investigated to show full vectorial effects.

Fig. 12 (b) and (c) show the reference field amplitudes by the rigorous solution FEM. Fig. 12 (b) is the amplitude of the  $y$  component of the electric field in TE polarization. Analogously, Fig. 12 (c) is the amplitude of the  $x$  component of the electric field in TM polarization. The field above the curved surface is only the reflected one, without including the incident field. The field at the lower side of the curved surface is the transmitted one.

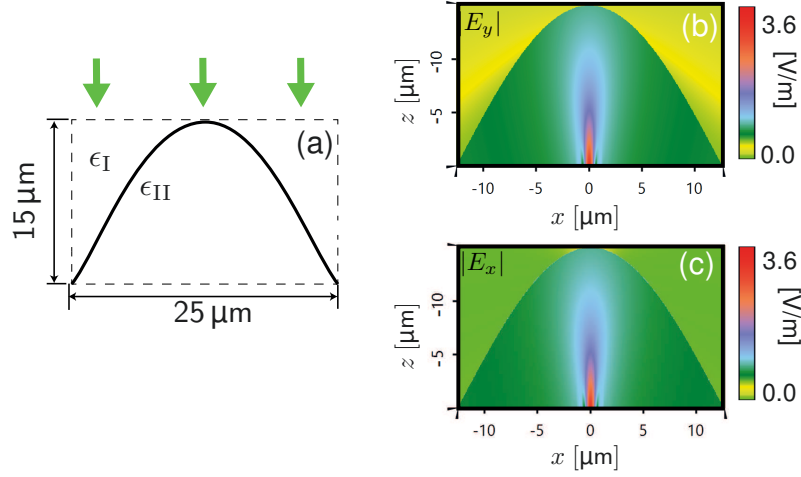


Figure 16: (a). Schematic of the structure: a half-sinusoidal surface with lateral size  $25\ \mu\text{m}$  and depth  $15\ \mu\text{m}$ . (b)-(c). The amplitudes of the electric field components are calculated by FEM.

From the first impression of the amplitudes, they look very much like they follow the local plane wave and local plane interface approximation. For a more precise validation, the comparison of both the amplitudes and the unwrapped phases directly on the curved surface for both the reflected and the transmitted fields for  $y$  and  $x$  components are performed respectively. The results are shown in Fig. 13. A very good agreement of

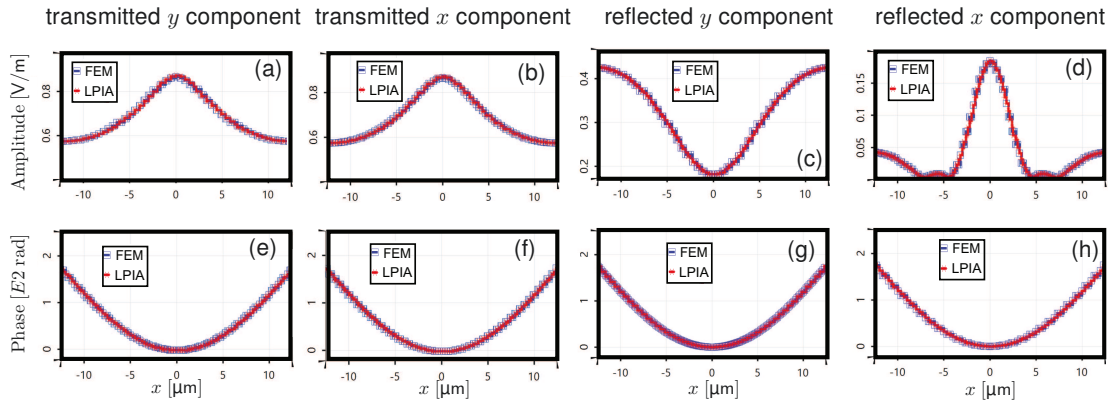


Figure 17: Comparison of field quantities on the curved surface obtained by LPIA and FEM corresponding to Fig. 16.

the quantities from LPIA and FEM is achieved. Evaluating the agreement by the deviation  $\sigma^{\text{dev}}$ , it is below 0.1% for all the cases considered. For the reflected field, although it diffracts during propagation, LPIA is still valid directly on the surface. The calculation time for LPIA is  $\sim 0.2\text{s}$  on an everyday computer. But it is  $\sim 15\text{mins}$  for FEM on the same computer, which is  $\sim 4500$  times slower.



Following an analogous logic, the reference field amplitudes by FEM for the second example are shown in Fig. 14 (b) and (c) for the  $y$  and  $x$  components respectively. The size of the curved surface is only  $1.25\ \mu\text{m}$  which is comparable to the wavelength. The comparison results of the amplitudes and unwrapped phases on the curved surface are shown in Fig. 15. All the  $y$  and  $x$  components of the transmitted and reflected field are compared. They are again in good agreement. The deviations are also below  $0.1\%$ . The calculation time for LPIA in this case is  $\sim 0.2\text{ s}$  on an everyday computer. But it is  $\sim 40\text{ s}$  for FEM on the same computer, which is around 200 times slower.

For the third example, the whole reflected and transmitted fields are shown in Fig. 16 (b) and (c). The field quantities are compared on the curved surface shown in Fig. 17, as the previous example, by both LPIA and FEM. The results are still in good agreement.

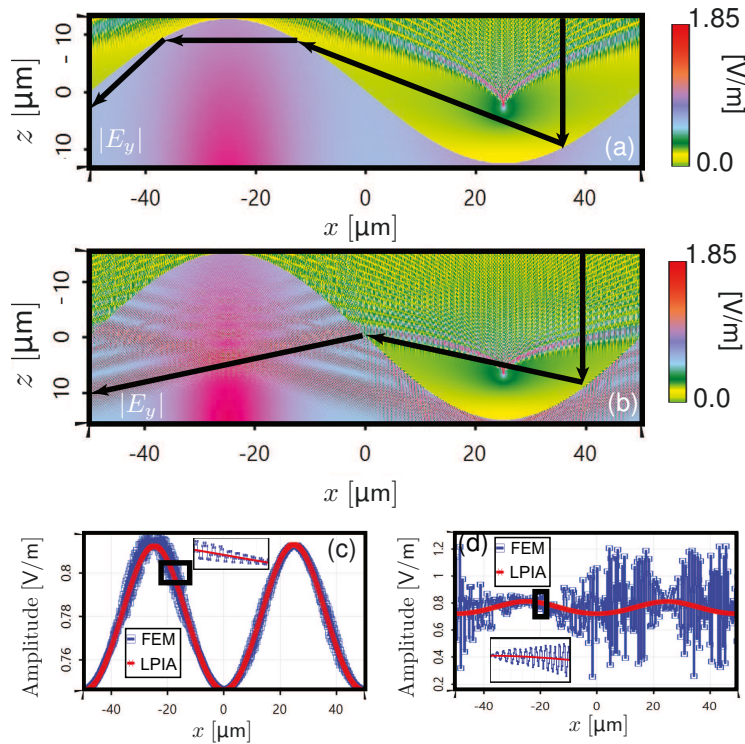


Figure 18: The amplitude of the  $y$  component by FEM with the height of the structure  $25\ \mu\text{m}$  in (a) and  $30\ \mu\text{m}$  in (b). The black lines with arrows indicate the multi-reflection and refraction. Comparison of the amplitudes of the transmitted fields on the curved surface obtained by LPIA and FEM in (c) and (d). The insets are the magnification of the parts in black boxes.

The deviation is still below  $0.1\%$ . From the results, it is concluded that even though the transmitted field at the reference plane  $z = 0$  is not in the homeomorphic zone, the diffraction appears during propagation. LPIA is validated on the curved surface. The calculation time for LPIA is  $\sim 0.2\text{ s}$  on an everyday computer. But it is  $\sim 4\text{ mins}$  for FEM on the same computer, which is around 1200 times slower. When the size of the structure is larger, the advantage of LPIA is more obvious compared to the rigorous

solvers, e.g. FEM.

In the previous part, only the cases when LPIA is validated are considered. It is natural

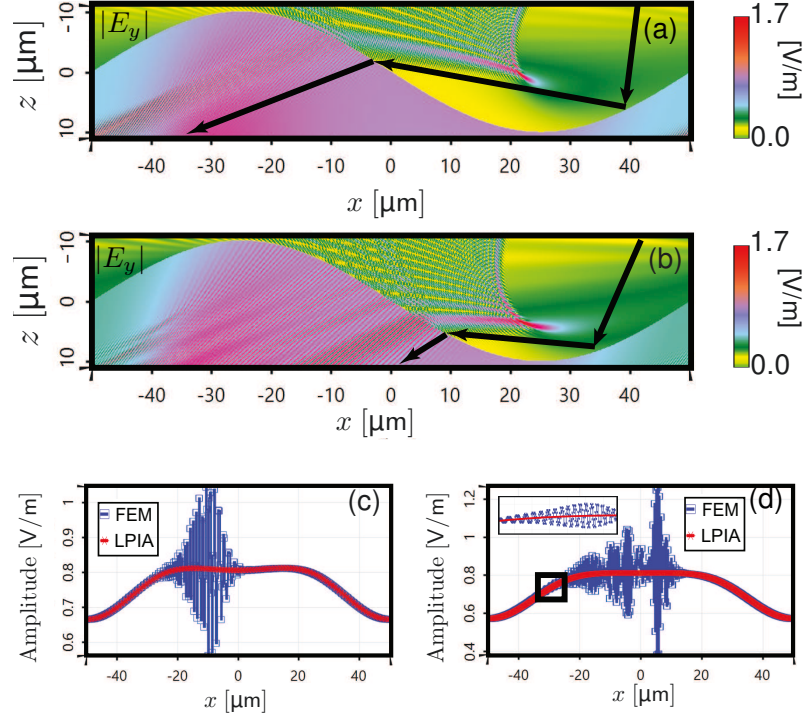


Figure 19: The amplitude of the  $y$  component by FEM with the incident angle  $20^\circ$  in (a) and  $30^\circ$  in (b). The black lines with arrows indicate the multi-reflection and transmission. Comparison of the amplitudes of the transmitted fields on the curved surface obtained by LPIA and FEM in (c) and (d). The insets are the magnification of the parts in black box in (d).

to wonder where the limitation is. Therefore, two groups of evaluation examples are performed.

In the first group, the multi-reflection and transmission occur which has a clear physical interpretation.

In Fig. 18, lateral size of the curved surface are kept as  $100\text{ }\mu\text{m}$  and increase the heights of the surface to  $25\text{ }\mu\text{m}$  shown in (a) and  $30\text{ }\mu\text{m}$  shown in (b). For simplicity, only the amplitudes of the  $y$  components are shown. In Fig. 18 (a) and (b), part of the reflected field impinges upon the same surface multiple times, thus making the LPIA of the first order inaccurate. It is not mentioned in [96]. Higher-order LPIA produces more accurate results. But it causes higher numerical effort and degrades the speed advantage of the LPIA of the first order. The amplitudes on the surface by LPIA of the first order are compared with FEM as shown in Fig. 18 (c) and (d), which correspond to the structure in Fig. 18 (a) and (b). LPIA becomes inaccurate when multiple reflections and transmissions occur. The inaccuracy increases as the multiple reflections and transmissions increase. The inaccuracy comes from the exclusion in the first-order LPIA treatment of



the multiple interactions of the field with the interface.

In Fig. 19, the structure are kept the same as in Fig. 12 (a). The incident field is the same as in the previous case but with different incident angles. The amplitudes are shown in Fig. 19 (a) for incident angle  $20^\circ$  and (b) for incident angle  $30^\circ$ . By comparing the amplitudes on the surface from LPIA and FEM as shown in Fig. 19 (c) and (d), the same conclusion is reached as before. The results from LPIA is still accurate in the positions where multiple interactions do not occur.

In the second group, the multiple reflections and transmissions do not occur but there

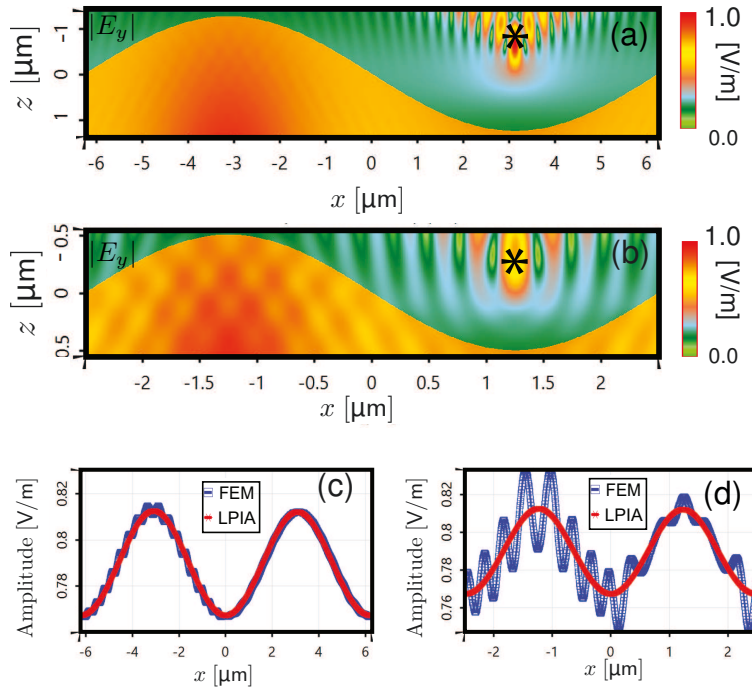


Figure 20: The amplitude of the  $y$  component by FEM with lateral size  $12.5\text{ μm}$  and height  $2.5\text{ μm}$  in (a) and the lateral size  $5\text{ μm}$  and height  $1\text{ μm}$  in (b). The black asterisks indicate the geometric focuses. Comparison of the amplitudes of the transmitted fields on the curved surface in (c) and (d).

appears an internal resonance due to the diffraction and this would mean there are, in fact, multiple interactions with the surface, which also has a clear physical interpretation.

In Fig. 20, the ratio of the lateral size to the height of the structure is kept the same as in Fig. 12. The incident field is also the same. Therefore, there are no multiple reflections and transmissions predicted by the local plane wave model. But as the lateral size and the height decrease as shown in Fig. 20 (a) and (b), the focal spots as indicated by the black asterisks are closer to the surface. Therefore, the interaction of the diffracted field with the surface still occurs which makes the LPIA inaccurate. It is not mentioned in [96]. The internal resonance effect cannot be directly added by taking the higher orders of LPIA into consideration in principle. It gives the fundamental limitation of LPIA deal-

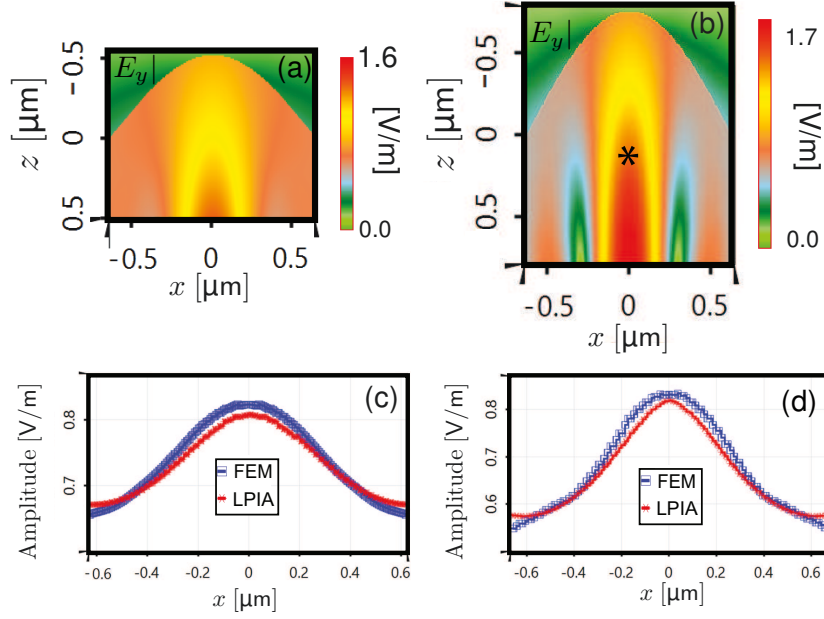


Figure 21: The amplitude of the  $y$  component by FEM with lateral size  $1.25 \mu\text{m}$  and height  $0.5 \mu\text{m}$  in (a) and the lateral size  $1.25 \mu\text{m}$  and height  $0.75 \mu\text{m}$  in (b). Comparison of the amplitudes of the transmitted fields on the curved surface in (c) and (d).

ing with micro-/nano-structures. By comparing the amplitudes on the surface by LPIA with those by FEM as shown in Fig. 20 (c) and (d), the inaccuracy of LPIA is influenced by the internal resonance. But the result from LPIA can give a good prediction of the mean envelope of amplitude.

In Fig. 21, another example of internal resonance is shown. The lateral size of the curved surface  $1.25 \mu\text{m}$  are kept (the same as in Fig. 14) and the height of the structure increases to  $0.5 \mu\text{m}$  in Fig. 21 (a) and  $0.75 \mu\text{m}$  in Fig. 21 (b). By increasing the height, the focal spot is closer to the surface so that internal resonance occurs. The comparison of the amplitudes of the transmitted fields on the surface by LPIA and FEM is shown in Fig. 21 (c) and (d). The deviation increases but not strongly because the resonant fields are not so strong.

According to the evaluation of the limitations, any kind of optical surfaces, which can avoid the multiple reflection/transmission and the internal resonance with the surface, can be studied accurately under this theory. For example, sinusoidal or freeform surface with low aspect ratio, with paraxial incidence can be studied. For the specifically given surface and incidence, it can be analyzed according to the two mentioned limitations.

#### 3.2.1.2 Combined with free space propagation

As formulated in chapter. 2, the output field is defined at a reference plane. It is desired to validate the output field by comparing LPIA combined with Free-Space Propagation (FSP) with FEM. As shown in Fig. 12, the output field, which is the reflected field at  $z = -10 \mu\text{m}$ , is in the focal region. It can be obtained from the field on the surface by

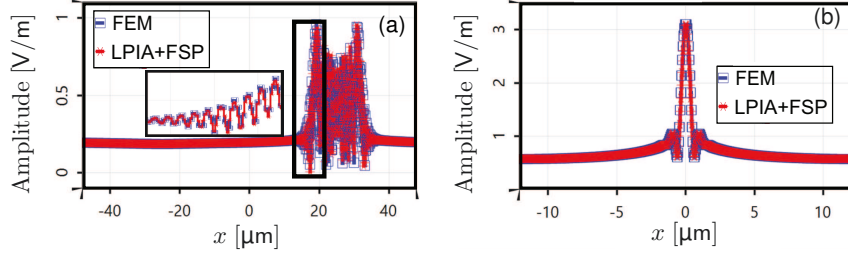


Figure 22: (a). Comparison of the reflected fields on the reference plane at  $z = -10 \mu\text{m}$  in Fig. 12 (b). (b). Comparison of the transmitted fields on the reference plane at  $z = 0 \mu\text{m}$  in Fig. 16 (b).

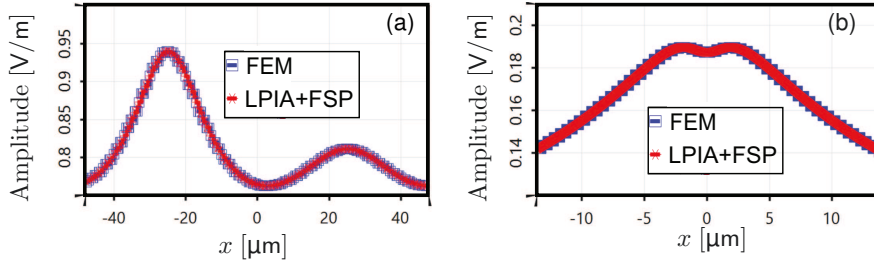


Figure 23: (a). Comparison of the transmitted fields on the reference plane at  $z = 10 \mu\text{m}$  in Fig. 12 (b). (b). Comparison of the reflected fields on the reference plane at  $z = -15 \mu\text{m}$  in Fig. 16 (b).

a diffraction integral [108, 109]. The amplitude of the reflected field at  $z = -10 \mu\text{m}$  is compared with that obtained by FEM. They are in good agreement, as shown in Fig. 22 (a). The output field, as shown in Fig. 16 (b), is the transmitted field at  $z = 0 \mu\text{m}$ . It is also obtained by a diffraction integral. The amplitude is compared with FEM that they are in good agreement as shown in Fig. 22 (b). Both of the amplitudes obtained by LPIA have a deviation  $\sigma^{\text{dev}} < 0.1\%$  respect to the FEM reference.

When the output field at the reference plane is in the homeomorphic zone, the local plane wave propagation [86, 96, 103] is applied with fast computational speed. Fig. 23 (a) shows the amplitudes of the transmitted fields when the structure is that of Fig. 12 (a). The reference plane is at  $z = 10 \mu\text{m}$ . The results obtained by LPIA with FSP based on local plane wave propagation are in good agreement with those obtained by FEM. Another example is shown in Fig. 23 (b), which shows the amplitude of the reflected field based on the structure shown in Fig. 16 (a). The reference plane is at  $z = -15 \mu\text{m}$ . The results obtained by LPIA with FSP based on local plane-wave propagation are in good agreement with those obtained by FEM. Both of the amplitudes obtained by LPIA have a deviation  $\sigma^{\text{dev}} < 0.1\%$  respect to the FEM reference.

The above comparison of the single interface is very essential for interpreting the LPIA for real surface. But the single surface is not very often used as an optical component. Therefore, in the following, the results from a double-surface component is also com-

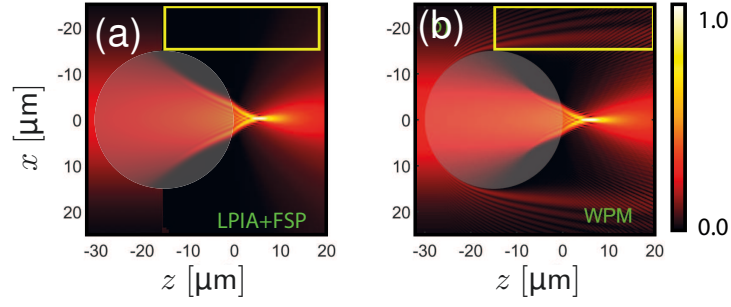


Figure 24: (a). Amplitude of the electric field calculated by LPIA+FSP. (b). The reference calculated by WPM. It is adapted from Fig. 1 (b) in [191].

pared with a highly accurate method: WPM. In order to compare the results from literature, the parameters for the component and the incident wave are the same as the ones in [191]. The 1D Gaussian beam, polarized in  $y$  direction, with wavelength 632 nm

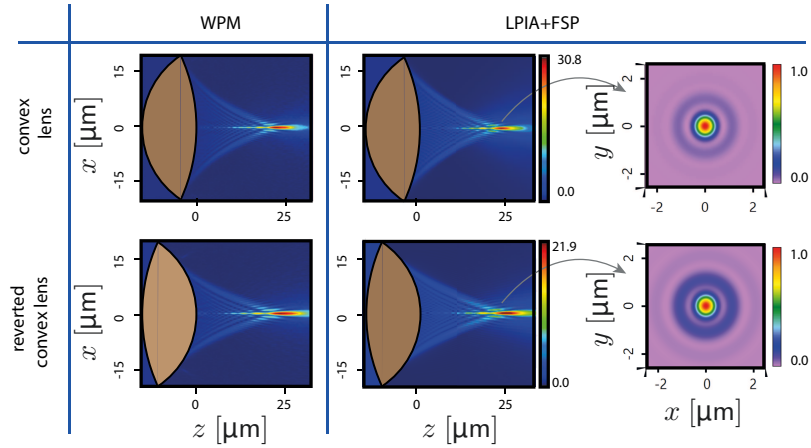


Figure 25: The comparison of LPIA+FSP with WPM. The amplitudes of  $E_y$  is shown in the second column compared with the ones in the first column adapted from [193]. The normalized energy density at the focal plane  $z = 25 \mu\text{m}$  are shown in the third column.

and a waist radius of  $\omega_0 = 15 \mu\text{m}$  focuses through a cylindrical rod lens whose refractive index is  $n^g = 1.5$  and diameter is  $30 \mu\text{m}$ . Its numerical aperture is around 0.8. The second surface is in the focal region as indicated in Fig. 24. The amplitude of the  $y$  component of the electric field is shown in Fig. 24 (a). In this example, the comparison of the propagation of the transmitted field is performed. Therefore, the incident field and the refracted field from the first surface is not included as indicated in the yellow boxes. The transmitted beam calculated by LPIA combined with the free space propagation is in very good agreement with the one obtained by WPM in [191] shown in Fig. 24 (b). Even though the above example is based on an optical components with two surfaces, it is still 2D, thus it is not used as often as the lenses consisting of 3D surfaces in practice.

Therefore, the calculation for 3D real-lens surface is also investigated in the following. In order to compare the results with the ones obtained by WPM in literature. The parameters are in accordance with the ones in [193]. The 2D plane wave, polarized in  $y$  direction, with wavelength 633 nm is focused by two different types of spherical convex lenses. The first lens has a smaller curvature radius for the first surface which is  $24\text{ }\mu\text{m}$  than the second which is  $-50\text{ }\mu\text{m}$ . The second lens is the reverted one of the first lens as indicated by the solid brown color in Fig. 25. The diameter of the lenses are  $40\text{ }\mu\text{m}$  with the refractive index  $n^l = 1.5$ . The  $x - z$  section of the amplitude of the  $y$  component of the electric field through an entire 3D-field distribution is shown in the second column compared with the results from [193] in the first column in Fig. 25. They are in very good agreement. The differences between these two lenses, e.g. aberrations, energy losses are indicated by both methods.

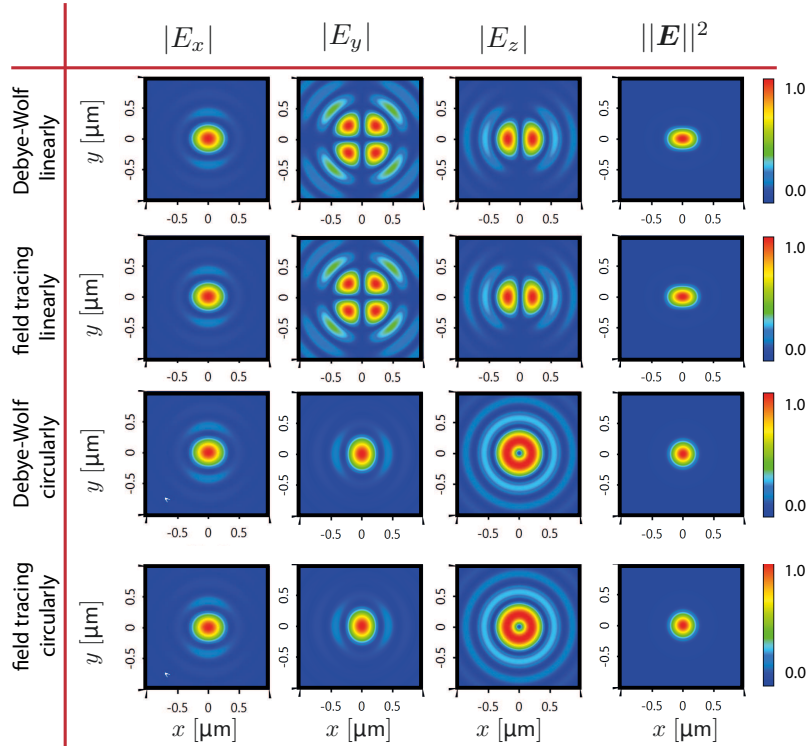


Figure 26: Comparison of the commonly used Debye-Wolf integral and the field tracing based on B operator for idealized aplanatic lens.

### 3.2.2 Fictitious curved surface

In the following numerical results for the fictitious curved surfaces, the input fields are plane waves with wavelength  $\lambda = 532\text{ nm}$ . The numerical aperture is 0.95 in air. The amplitudes and energy densities at the focal plane are normalized.

### 3.2.2.1 Focusing of uniformly polarized plane waves

First, the focusing of the uniformly polarized plane waves, which are linearly and circularly polarized, are compared with the Debye-Wolf integral [66]. The results are shown in first, second and third columns for each of the components of the electric field in Fig. 26. The vectorial effects are clearly demonstrated both for linearly and circularly polarized beams. The results by the B operator based on the field tracing techniques are in very good agreement with the direct Debye-Wolf integral.

### 3.2.2.2 Focusing through variously-shaped apertures

From the theory in chapter 2, the shapes aperture based on the field tracing techniques is not restricted. Therefore, the focusing of the linearly and circularly polarized beams with rectangular and annular apertures are performed directly. The results are shown in Fig. 27. The results from rectangular aperture is distorted compared to the one from circular aperture as shown in Fig. 27 (c)-(d). The results from the annular aperture has more aberrations compared to the circular aperture but with reduces lateral size as shown in Fig. 27 (g)-(h).

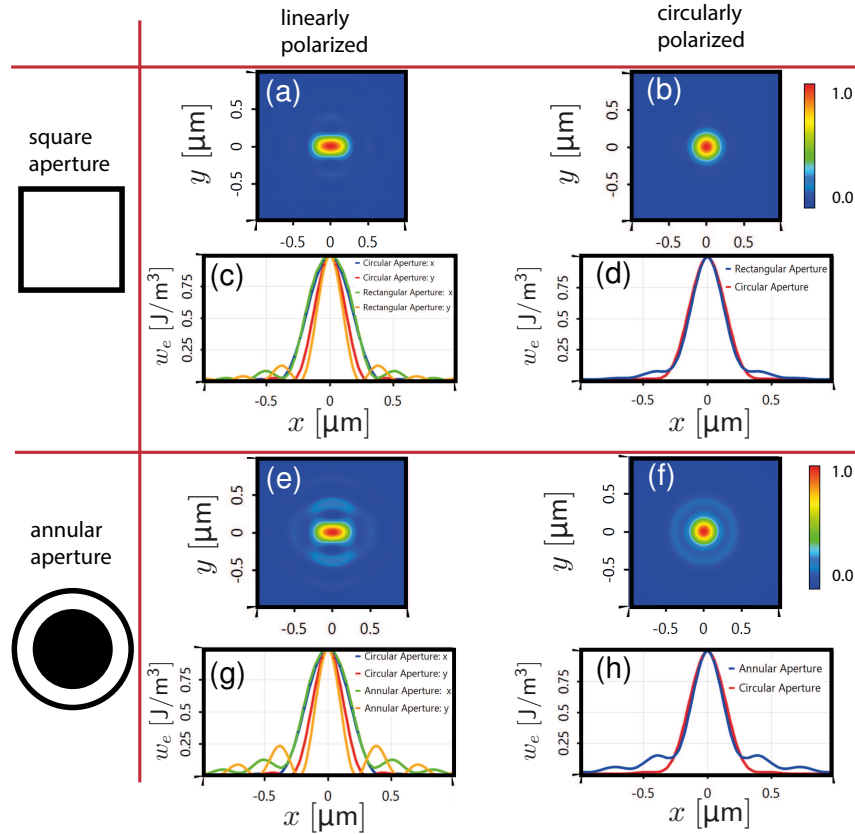


Figure 27: The demonstration of the flexibility of the field tracing techniques of square and annular apertures based on B operator for idealized aplanatic lens.

### 3.2.2.3 Focusing of cylindrical vector beams

Not only the shapes of the aperture is not restricted via the field tracing techniques based on B operator for fictitious surfaces, but also the polarization of the beam is not restricted. Therefore, the results obtained for cylindrical vector beams, e.g. radially and azimuthally polarized beams, are shown in Fig. 28. The transverse components and the longitudinal components of the radially polarized beams are shown to demonstrate the vectorial effects clearly.

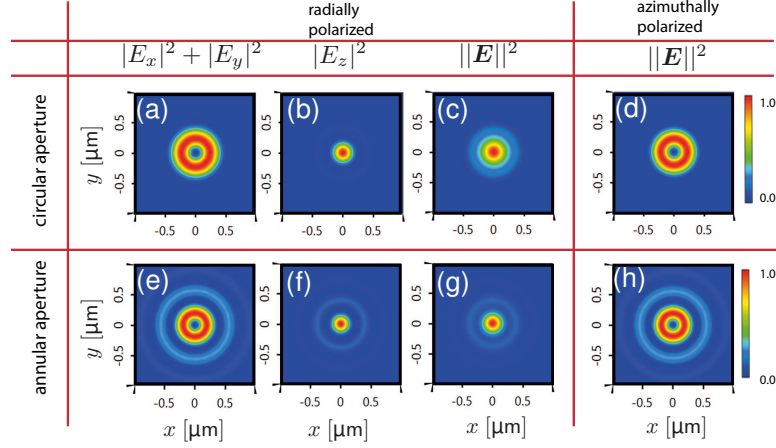


Figure 28: The demonstration of the flexibility of the field tracing techniques of focusing of radially and azimuthally polarized beams based on B operator for idealized aplanatic lens.

## 3.3 OPERATOR FOR MICRO-/NANO-STRUCTURES

### 3.3.1 Periodic structure

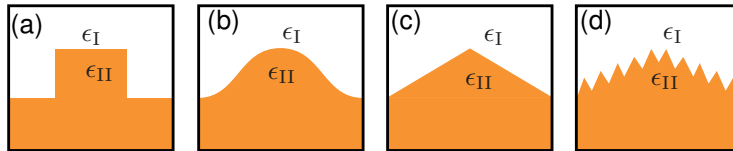


Figure 29: The demonstration of different types of profiles of the gratings.

Periodic structures, e.g. gratings, photonic crystal, are widely used in microscopy systems in nanooptics. Therefore, variously-shaped profiles of 2D gratings are in the need of modeling. The typical ones are taken in the following examples for the investigation of the convergence and calculation speed of FMM compared with IM and FEM. They



are rectangular, sinusoidal, triangular and combined two triangular profiles as shown in Fig. 29. The incident wave is plane wave with normal incidence with wavelength 532 nm. The period of the grating is 1  $\mu\text{m}$ . The thickness of the grating profile is 1  $\mu\text{m}$ . The combined triangular grating has a second grating with period of 50 nm and thickness of 500 nm. The permittivity of the input region, which is air, is  $\epsilon_I = 1$ . The permittivity of the transmitted grating, which is fused silica, is  $\epsilon_{II} = 2.135$ . The permittivity of the reflected grating, which has a gold substrate, is  $\epsilon_{II} = -5.568 + i2.245$ .

The diffraction efficiencies of the transmitted +1 order for fused silica and the reflected

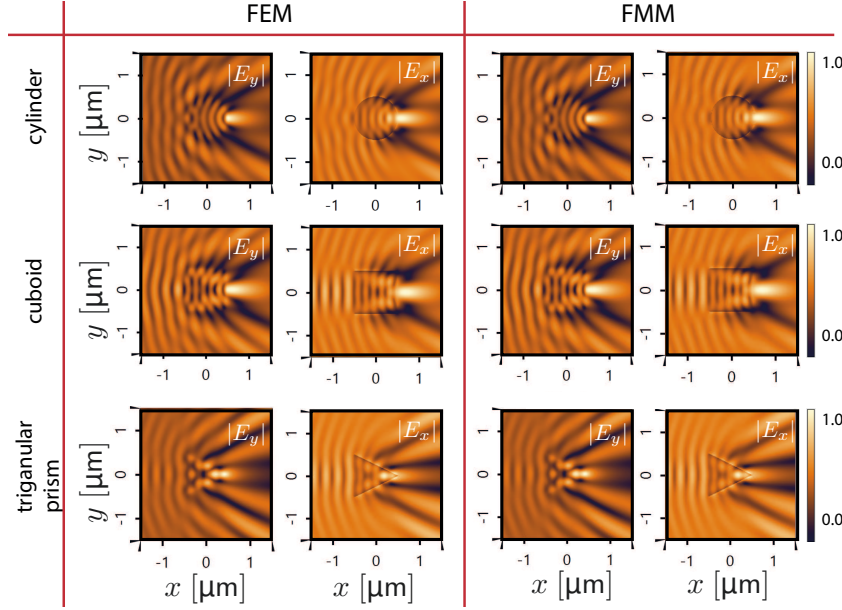


Figure 30: Comparison of the modeling of nanocylinder in the upper row, of cuboid in the middle row, of triangular prism in the lower row.

+1 order for gold are shown in Tab. 2 together with the calculation time. By comparing with IM and FEM for the rectangular profile, FMM shows the advantage that only one layer is used. By using the inverse rule [158], TM case for fused silica has the same convergent speed. But for gold which is metal, it still has slower convergent speed than TE. By comparing with IM and FEM for the sinusoidal and triangular profiles, FMM has slower convergent speed than IM and FEM in the case of TM, especially with gold because of the influence from layering of the profile using staircase approximation [170]. For the combined triangular profile which is more complex, all of the three methods need more time. FMM nearly fails to obtain the convergent result for TM with gold. The oscillation of the fields caused by the staircase is too strong because more layers are needed for the complex profile [170].

### 3.3.2 Aperiodic structure

The theory of the aperiodic structure based on FMM with PMLs is already mature. Therefore, only a few examples are shown in Fig. 30 and Fig. 31 for 2D and 3D struc-



Table 2: Diffraction Efficiencies (DE) and calculation time for different types of 2D grating by different methods

			fused silica		gold	
			TE	TM	TE	TM
rectangular	DE	FMM	21.2582 %	26.8610 %	22.5454 %	6.8750 %
		IM	21.2581 %	26.8611 %	22.5452 %	6.8758 %
		FEM	21.2582 %	26.8611 %	22.5452 %	6.8751 %
	time	FMM	0.12 s	0.15 s	0.2 s	2.1 s
		IM	11 s	11 s	13 s	13 s
		FEM	9 s	9 s	10 s	10 s
sinusoidal	DE	FMM	16.0165 %	38.3079 %	20.4293 %	2.268 %
		IM	16.0167 %	38.3075 %	20.4298 %	2.263 %
		FEM	16.0160 %	38.3070 %	20.4291 %	2.269 %
	time	FMM	6 s	31 s	13 s	300 s
		IM	0.26 s	0.26 s	0.31 s	0.5 s
		FEM	10 s	10 s	11 s	11 s
triangular	DE	FMM	28.8279 %	43.9181 %	0.068 59 %	3.843 %
		IM	28.8270 %	43.9187 %	0.068 50 %	3.846 %
		FEM	28.8271 %	43.9189 %	0.068 52 %	3.841 %
	time	FMM	6 s	33 s	15 s	400 s
		IM	1 s	1 s	1.3 s	1.3 s
		FEM	10 s	10 s	12 s	12 s
combined	DE	FMM	37.958 %	43.129 %	0.001 45 %	0.4377 %
		IM	37.953 %	43.127 %	0.001 49 %	0.4764 %
		FEM	37.956 %	43.121 %	0.001 44 %	0.4781 %
	time	FMM	120 s	700 s	480 s	4800 s
		IM	28 s	28 s	90 s	90 s
		FEM	25 s	25 s	28 s	28 s

tures for the validation of the codes.

For the 2D structures, the plane wave, with wavelength 532 nm, propagates through variously-shaped structures made of fused silica with refractive index  $n^f = 1.461$ . The shapes are circular with the diameter of 1  $\mu\text{m}$ , square with the size of 1  $\mu\text{m}$  and triangular with both the width and thickness of 1  $\mu\text{m}$ . The normalized amplitudes for TE and TM field components are shown in Fig. 30. By comparing with FEM, they are in very good agreement with the deviation below 0.02 %.

For the 3D structure, the plane wave, polarized in  $x$  direction, with wavelength of

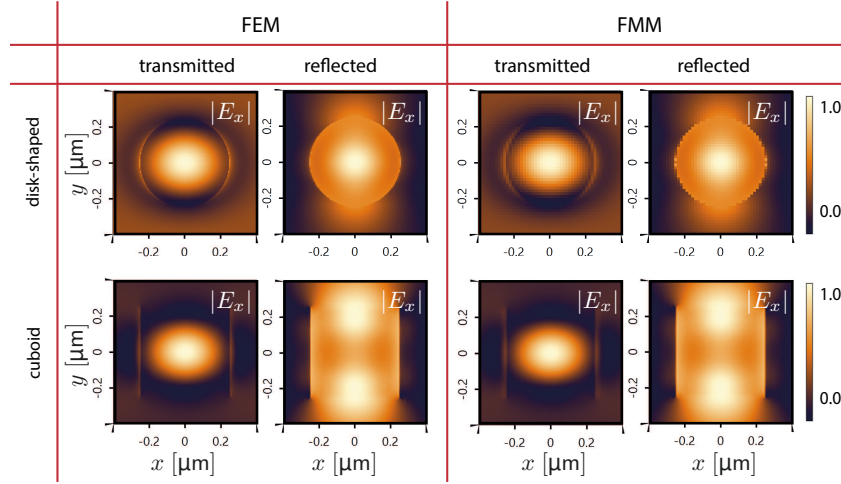


Figure 31: Comparison of the modeling of disk-shaped particle in the upper row and of cuboid particle in the lower row.

532 nm, propagates through disk-shaped and cuboid nanoparticles. The disk-shaped nanoparticle with diameter and the thickness of both 500 nm is made of glass with refractive index  $n^g = 1.5$ . The cuboid nanoparticle is made of the same medium with lateral sizes and the thinness of 500 nm.

The normalized amplitudes of the  $x$  component of the transmitted and reflected electric fields are shown in Fig. 31. By comparison with FEM, they are in very good agreement with the deviation below 0.02 %.

### 3.4 SUMMARY AND CONCLUSION

The numerical validations of the B operators for curved surfaces and micro-/nano-structures are performed by comparing with other rigorous or accurate methods. The pros and cons of the B operators based on LPIA and FMM are investigated. Therefore, the accuracy of the B operators used in the following chapters is guaranteed.



## MODELING OF FOCUSING THROUGH A MICRO-/NANO-PARTICLE

---

### 4.1 INTRODUCTION

As mentioned in chapter 1, a focal spot with as small as possible lateral size is desired, not only for high-resolution microscopy [62, 63, 65], but also in optical lithography, optical data storage, laser machining, etc. However, lateral spot size is restricted by the diffraction limit investigated by Rayleigh [53] and Abbe [1]. In recent years, various methods have been proposed to obtain an ever-smaller lateral size of the focal spot.

Quabis et.al. found, through numerical investigations, that the focusing of a radially polarized beam with an annular aperture results in an even smaller focal spot compared to the diffraction limit [194]; later, experimental results measured with the knife-edge method [195, 196] by focusing with  $NA = 0.9$ , validated the numerical prediction [7]. Additional experiments managed to provide an even smaller focal spot [197] by focusing with  $NA = 1.4$ . The size of the focal spot when linearly, circularly and radially polarized fields are used in combination with an annular aperture is investigated numerically in [198] and is reviewed in [9]. Some authors also demonstrated the sub-diffraction focusing by using a mask based on the concept of superoscillation [199–203].

Besides the investigation of the polarization of the beams and the types of apertures/-masks which influence the size of the focal spot, other authors added a microsphere in the focal region of the convectional microscopy system, which is called microsphere-based microscopy [12, 14, 83], to demonstrate super resolution experimentally. However, the focal spot behind the microsphere was demonstrated numerically only by assuming ideal plane wave illumination [13, 204]. Later, an engineered microsphere added in the focal region of a conventional microscopy system with radially polarized beam was proposed [10]. A focal spot, which was called nanojet, with the size  $\sim 0.14 \lambda^2$  behind the engineered microsphere, was demonstrated numerically [10].

With a similar aim in mind, a fully vectorial physical-optics modeling of the focusing of an electromagnetic field through a micro-/nano-particle of size comparable to the wavelength is performed in this chapter. The focused field on the micro-/nano-particles is obtained with linearly, circularly and radially polarized input fields with both circular and annular apertures. The micro-/nano-particles have spherical, disk and cuboid shapes, shown in Fig 32. The size of the focal spot behind the micro-/nano-particle is investigated and analyzed.

To this point, all of the numerical simulations are based on an ideal lens which is aplanatic. It satisfies the Abbe sine condition. In experiment, the real lens system is used which might bring defects because of aberration and misalignment. Few were discussed in the literature. In [205], a method was proposed to include the presumed aberration. In [78], the aberration of astigmatic of a Gaussian field was presumed by the authors. In [79], the aberration of preliminary astigmatic of a vortex beam is presumed by the

authors. However, no aberration from the real lens system is discussed. Therefore, the focusing of linearly, circularly and radially polarized waves are performed also by the real lens system in this chapter, shown in Fig. 33. The aberration of a real lens system, especially of a misaligned real lens system is analysed. The focusing of the aberrated spot through the micro-/nano-particle is also investigated. This chapter is structured as: in Sec. 4.2 modeling tasks and techniques are summarized by the field tracing diagram; in Sec. 4.3 the numerical results for focusing by an ideal lens and through a micro-/nano-particle are presented and analyzed; in Sec. 4.4 the numerical results for focusing by a real lens and through a micro-/nano-particle are presented and analyzed. Sec. 4.5 summarizes and concludes the chapter.

#### 4.2 MODELING TASKS AND TECHNIQUES

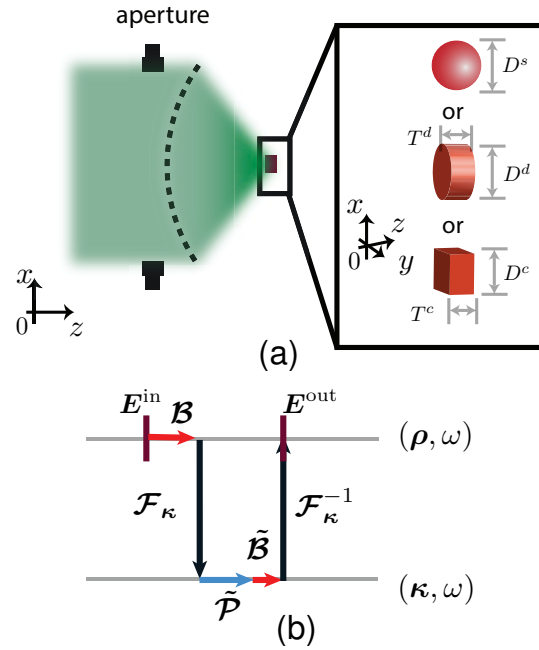


Figure 32: (a). Schematic of focusing through a micro-/nano-particle by ideal lens. (b). The corresponding field tracing diagram.

Firstly, the focusing by an ideal lens is performed as shown in Fig. 32. The paraxial Gaussian wave with linear, circular and radial polarizations by both circular and annular apertures are focused through a micro-/nano-particle. The micro-/nano-particle is dielectric and placed in the focal region of the ideal lens. It is variously shaped, including spherical, disk-shaped and cuboid. The focal spots only by the lens system are obtained at the focal plane first, and then the focal spots behind the micro-/nano-particles are obtained and analyzed [206]. The size of the spot  $\delta$  is defined as the area divided by square of the wavelength  $\lambda$ . The area is defined where the energy density is above half the maximum. It is in accordance with the definition in [7, 197, 198]. Secondly, the focus-

ing by a real lens system is performed as shown in Fig. 33. The paraxial Gaussian wave

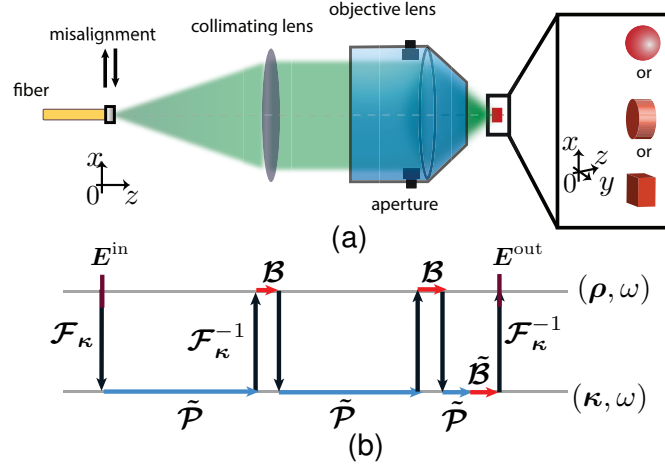


Figure 33: (a). Schematic of focusing through a micro-/nano-particle by real lens. (b). The corresponding field tracing diagram.

is generated by a fiber, then it is collimated by a real commercial lens and then focused also by a real commercial objective lens. The influence of the lateral misalignment of the fiber on the focused beam at the focal plane is investigated. The influence on the focal spot behind the micro-/nano-particles is investigated too. The modeling techniques in

Table 3: Summary of the applications of field tracing techniques.

		$\mathcal{B}$	$\tilde{\mathcal{B}}$	$\mathcal{F}_\kappa \& \mathcal{F}_\kappa^{-1}$
ideal lens	only focusing	LPIA:ideal	no	HFT&IFFT
	through spherical particle	LPIA:ideal	Mie	HFT&IFFT
	through disk-shaped particle	LPIA:ideal	FMM	HFT&IFFT
	through cuboid particle	LPIA:ideal	FMM	HFT&IFFT
real lens	only focusing	LPIA:real	no	HFT&IHFT but IFFT for the last one
	through spherical particle	LPIA:real	Mie	HFT&IHFT but IFFT for the last one
	through disk-shaped particle	LPIA:real	FMM	HFT&IHFT but IFFT for the last one
	through cuboid particle	LPIA:real	FMM	HFT&IHFT but IFFT for the last one

the framework of field tracing as demonstrated by the field tracing diagram shown in Fig. 32 (b) and Fig. 33 (b) are summarized in Tab. 3. Please note that the modeling of the spherical particle can be done by FMM. But it takes large numerical effort because of the layering as discussed in chapter 3. Therefore, Mie theory [89, 207, 208] is used instead in

this chapter for modeling of the spherical particle. The free-space-propagation operator between parallel planes is used and not listed in Tab. 3 for brevity.

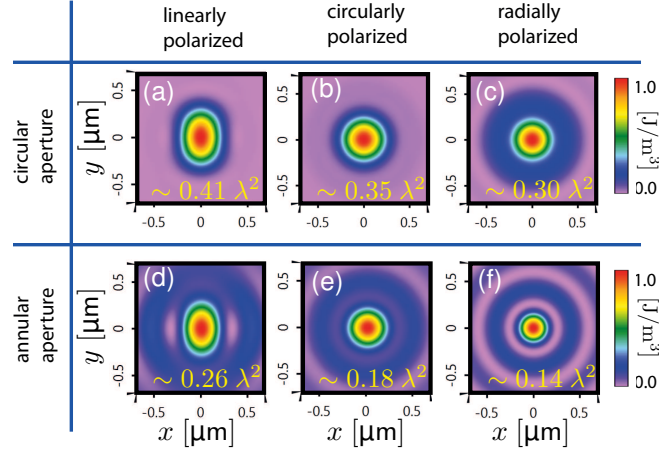


Figure 34: Energy densities at the focal plane obtained by only focusing by the idealized aplanatic lens. The sizes of the focal spot are noted in the corresponding figures in yellow.

#### 4.3 FOCUSING BY IDEAL LENS THROUGH A MICRO-/NANO-PARTICLE

##### 4.3.1 Focusing only by ideal lens system

The numerical experiments are performed for three different polarizations of the incident fields which are linearly (in  $y$  direction), circularly and radially polarized beams. For each of the polarization, the circular and annular apertures are used. As indicated in Fig. 32 (a), the input fields are paraxial Gaussian wave with a diameter ( $1/e^2$ ) which is 94 % of the diameter of the entrance pupil of the objective lens. The ratio of the radius of the inner block to the radius of the outer aperture is used to describe the size of the annular aperture. The size of the annular aperture for linearly and circularly are 65 % and 75 % respectively. The reason is that the smallest focal spots [198] are desired to be obtained. The size of the annular aperture for radially polarized is 90 % in order to have a small focal spot as well as enough energy. The ideal lens has a numerical aperture of 0.95 in air with refractive index  $n^a = 1.0$ , and the wavelength of the incident field is 632.8 nm in accordance with the parameters in [209].

The focal spots produced by the focusing lens system at the focal plane are shown in Fig. 34. They are calculated within several seconds. By measuring the sizes of the focal spots, we have the same conclusion as in [198] that the size of the radially polarized beam is smaller than the linearly and circularly polarized beams. The use of an annular aperture further decreases the size of the focal spots. The sizes of the focal spot are noted in the corresponding figures in yellow.

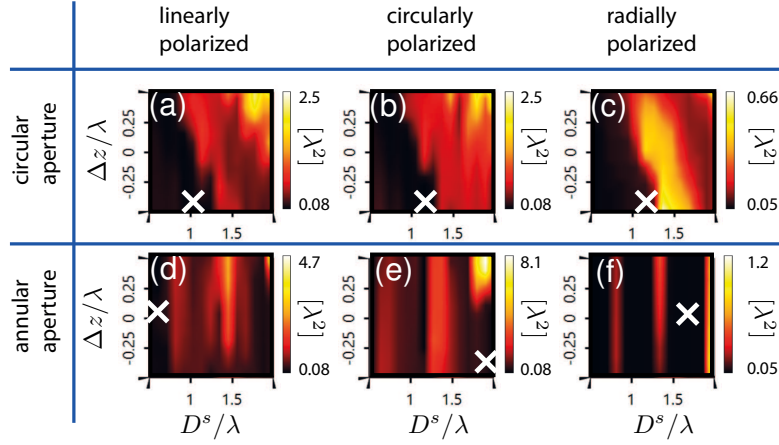


Figure 35: Scan of the parameter space (diameter of the spherical particle and distance from center of the particle to focal plane) to locate the parameter combination that minimizes the resulting spot size. The "X" is where the parameters are taken for the results in Fig. 36. The color scale represents the spot size.

#### 4.3.2 Focusing through a micro-/nano-particle

Then we move on to the next step, to show the results of focusing through spherical, disk-shaped and cuboid micro-/nano-particles. The micro-/nano-particles are dielectric

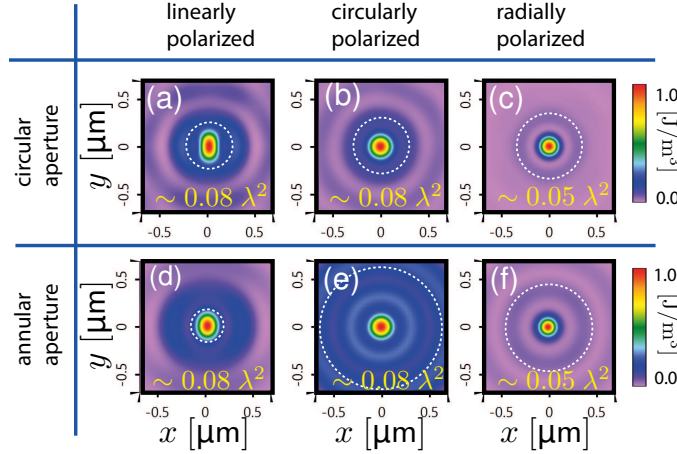


Figure 36: Energy densities obtained by focusing the field through spherical micro-/nano-particles. The dashed white circle represents the diameter of the spherical particle.

with refractive index  $n^p = 1.79$ . The size of the spherical particle is characterized by its diameter  $D^s$ , shown in Fig. 32 (a). The size of the disk-shaped particle is characterized by its diameter  $D^d$  and thickness  $T^d$ . The size of the cuboid particle is characterized by its lateral lengths  $D^c$  which are assumed equal, and thickness  $T^c$ . All the above size-related quantities are scaled by the wavelength for easy demonstration.



#### 4.3.2.1 Spherical micro-/nano-particle

As shown in Fig. 35, the parameter space defined by the diameter of the spherical particle and the longitudinal distance between the center of the particle and the focal plane is scanned. By doing so, the parameter combination that corresponds to the smallest focal spot behind the spherical particle is found. As a result of this analysis, it is found that the smallest spots for linearly and circularly polarized beams in both circular and annular apertures are around  $\sim 0.08 \lambda^2$ , shown in Fig 35 (a), (b), (d) and (e). The smallest spots for radially polarized beams in both circular and annular apertures are around  $\sim 0.05 \lambda^2$  in Fig. 35 (c) and (f). They are all beyond the diffraction limit. The reason is that the resonant effect of the spherical micro-/nano-particle generates evanescent waves which make the focal spots tiny ones. By comparing the circular (Fig. 35 (a)-(c)) and annular (Fig. 35 (d)-(f)) cases, it is found that the size of the focal spot is less sensitive to the longitudinal position of the micro-/nano-particle in the case of an annular aperture. The reason for this is the optical needle effect [210] in the focal region by the lens system when annular aperture is applied.

The tiny focal spots are shown in Fig. 36 with the size and longitudinal position marked

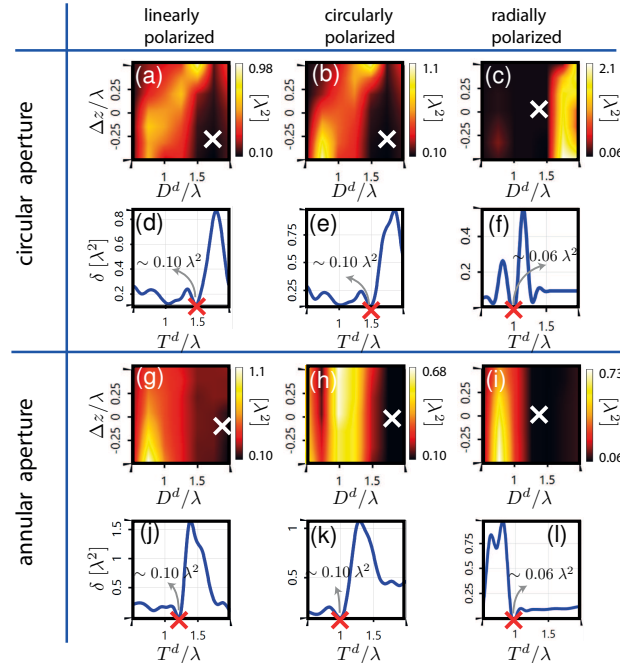


Figure 37: Scan of the parameter space (diameter of the disk-shaped particle and distance from center of the particle to focal plane in (a)-(c) and (g)-(i), thickness of the disk-shaped particle in (d)-(f) and (j)-(l) ) to locate the parameter combination that minimizes the resulting spot size. The white "X" is where the parameters are taken for the results in the corresponding figures below. The red "X" is where the parameters are taken for the results in Fig. 38.

by "X" in Fig. 35. The dashed white circle represents the diameter of the spherical particle. The tiny spots in the radially polarized case have less aberration compared to the

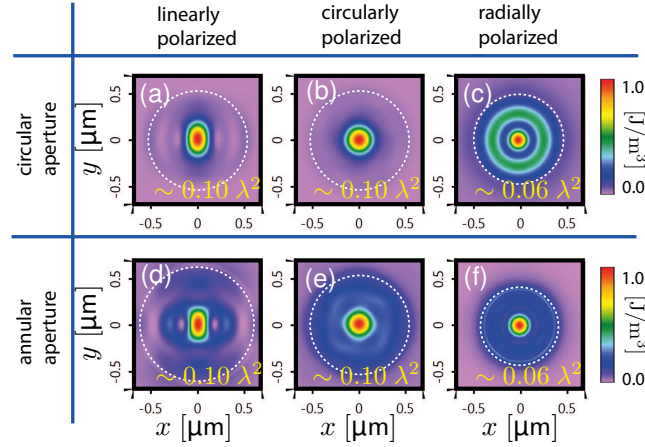


Figure 38: Energy densities obtained by focusing the field through a disk-shaped micro-/nano-particle. The dashed white circle represents the diameter of the disk-shaped particle.

linearly and circularly polarized cases. By comparing with Fig. 34, the decrease in the size of the focal spot behind the spherical particle is clearly demonstrated.

#### 4.3.2.2 Disk-shaped micro-/nano-particle

The spherical particle has concave surfaces. Therefore, it is straightforward to interpret the fact that it has a focusing effect. If the particle is disk-shaped with planar surfaces, does it still have a focusing effect? To answer this question, the analogous procedure to the previous subsection is followed. As shown in Fig. 37, first, the diameter  $D^d$  of the disk-shaped particle and the longitudinal distance between the center of the particle and the focal plane are scanned by making the thickness constant  $T^d = 1 \lambda$ . Then, the smallest focal spots as indicated by the white "X" is chosen, and the thickness  $T^d$  is scanned. Then the smallest focal spots are selected, as indicated by the red "X". It is found that the smallest spots for linearly and circularly polarized beams in both circular and annular apertures are around  $\sim 0.10 \lambda^2$ , shown in Fig. 37 (d), (e), (j) and (k). The smallest spots for radially polarized beams in both circular and annular apertures are around  $\sim 0.06 \lambda^2$ , shown in Fig. 37 (f) and (l). They are larger than in the case of a spherical micro-/nano-particle but still beyond the diffraction limit, which means evanescent waves are also generated. They are generated by resonant effects involving the entire disk, not only its planar surfaces. Without the presence of the side walls, i.e. if instead of the micro-/nano-particle there were only a planar slab, the focusing effect will not occur because no evanescent waves can be generated according to the phase matching condition.

The tiny focal spots are shown in Fig. 38. The aberrations for the radially polarized cases are more obvious than in the spherical particle case. The diameter of the disk-shaped particle is indicated by the dashed white circles.

## 4.3.2.3 Cuboid micro-/nano-particle

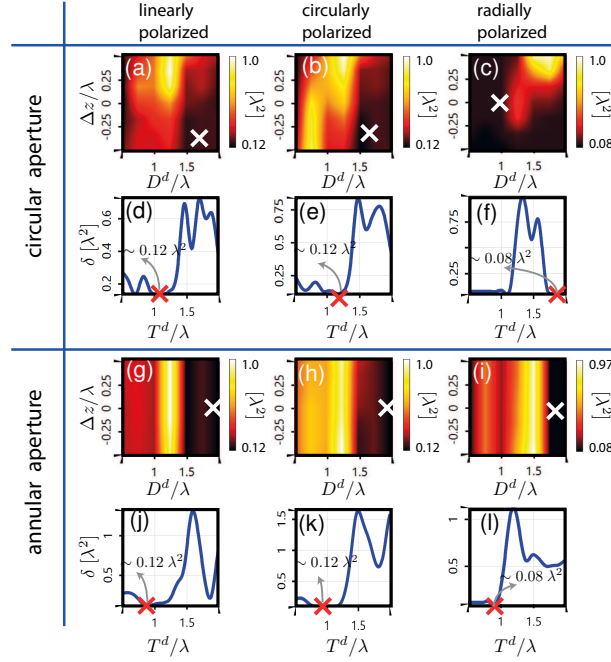


Figure 39: Scan of the parameter space (width and length, which are equal, of the cuboid particle and distance from center of the particle to focal plane in (a)-(c) and (g)-(i), thickness of the cuboid particle in (d)-(f) and (j)-(l) ) to locate the parameter combination that minimizes the resulting spot size. The white "X" is where the parameters are taken for the results in the corresponding figures below. The red "X" is where the parameters are taken for the results in Fig. 40.

The cuboid particle, which is rarely discussed in the literature, should also provide the focusing effect because it has side surfaces which have the potential to provide the resonant effect. Therefore, to prove this hypothesis, the same procedure as before is performed, as shown in Fig. 39. It is found that the smallest spots for the linearly and circularly polarized beams in both circular and annular apertures are around  $\sim 0.12 \lambda^2$ , shown in Fig. 39 (d), (e), (j) and (k). The smallest spots for the radially polarized beam in both circular and annular apertures are around  $\sim 0.08 \lambda^2$ , shown in Fig. 39 (f) and (l). They are larger compared to the spherical and disk-shaped particle cases. The reason might be that the planar side walls provide a less effective resonant effect than the curved side walls. But the size of the focal spots is still beyond the diffraction limit. The tiny focal spots are shown in Fig. 40 with demonstration of the aberration effects.

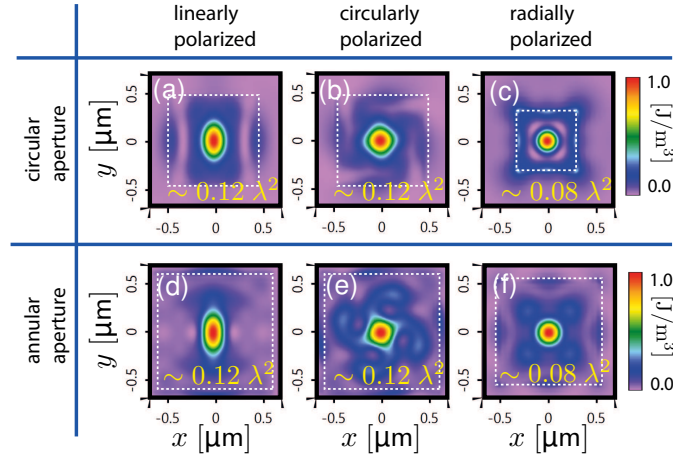


Figure 40: Energy densities obtained by focusing the field through certain cuboid micro-/nano-particles. The dashed white square represents the lateral size of the cuboid particle.

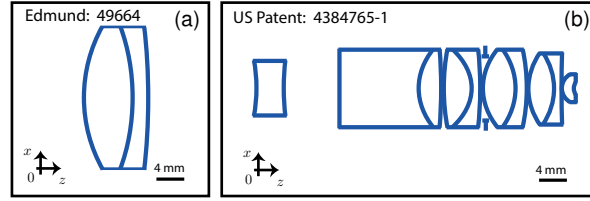


Figure 41: Cross section of the real lens system including the collimating and the objective lenses.

#### 4.4 FOCUSING BY REAL LENS THROUGH A MICRO-/NANO-PARTICLE

##### 4.4.1 Focusing only by real lens system

Considering performing the experiment, a real lens system which consists of complex lenses is applied. Therefore, the vectorial physical-optics modeling of the real lens system is performed to guide the experiment. In the real lens case, the corresponding numerical experiment is performed as in the ideal lens case: focusing of a linearly, circularly or radially polarized beam. Therefore, the same parameters are taken as the ones in the ideal lens case, e.g. the wavelength of 632.8 nm, the sizes of the annular aperture is of 65 %, 75 % and 90 % for the linearly, circularly and radially polarized beams respectively, etc. The real collimating lens consists of three spherical surfaces with an effective focal length of 40 mm as shown in Fig. 41 (a). The real objective lens, placed 150 mm behind the collimating lens, is apochromatic, consisting of sixteen spherical surfaces with  $NA = 0.95$  as shown in Fig. 41 (b). They are from the catalog of the commercial company Edmund Optics and from a US patent [211] respectively.

Firstly, when there is no misalignment for the real lens system, the focal spot at the focal plane is calculated as shown in Fig. 42 and compared with the ideal lens model

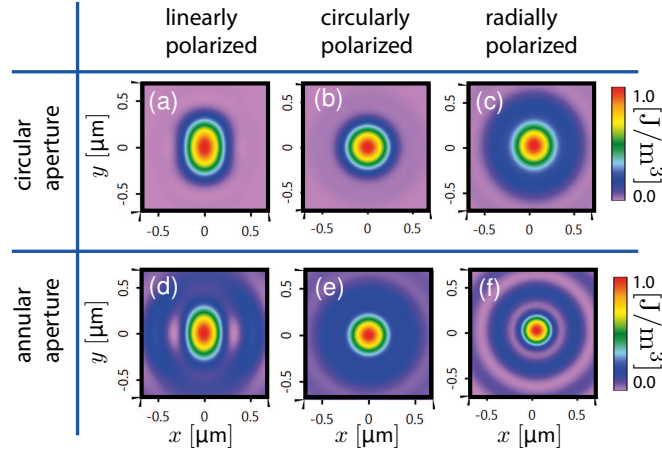


Figure 42: Energy densities at the focal plane obtained by only focusing by the real lens.

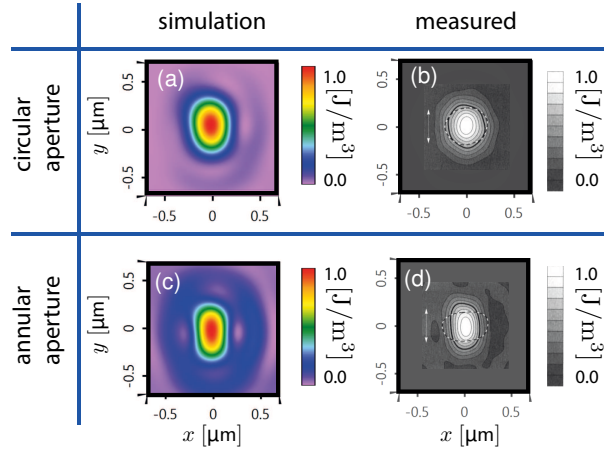


Figure 43: Comparison of the focal spots obtained via simulation using a real lens model and via experiment. (b) and (d) are adapted from Fig. 3 in [209].

shown in Fig. 34. The deviations between the ideal lens case and that with real lenses, with linearly, circularly and radially polarized beams and with both circular and annular apertures, are all below 0.5%. It means the real lens is well designed. Aberration has nearly no effect on the focal spot in the case of perfect alignment of the system. The calculation time for the real lens remains within seconds.

Secondly, when there is lateral misalignment of the real lens system, e.g. misalignment of the source of  $-200\mu\text{m}$  and  $200\mu\text{m}$  in  $x$  and  $y$  directions respectively, the results for focusing of the linearly polarized beam is compared with the experiment result in literature [209] as shown in Fig 43. Please note that the size of the annular aperture is 56% which is in accordance with the value in [209]. The distorted focal spots are demonstrated by both the numerical and experiment results. It indicates that the model in the framework of field tracing provides convincing results.

Then, when the source and the lens system are misaligned with respect to each other,

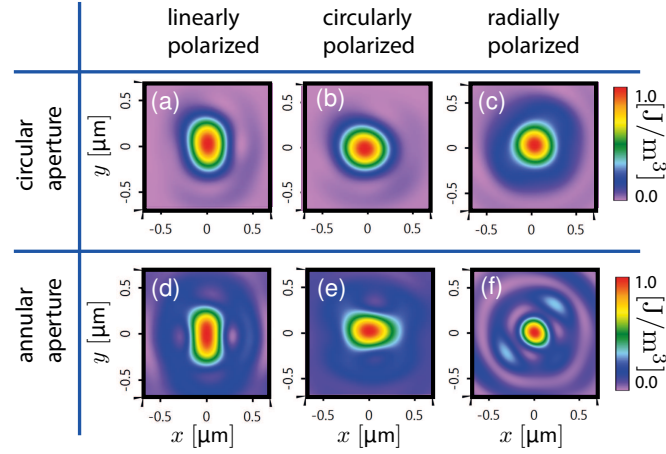


Figure 44: Energy densities obtained at the focal plane by simulation with a real lens model, with a misalignment of the source of  $-200 \mu\text{m}$  and  $200 \mu\text{m}$  in  $x$  and  $y$  directions respectively.

the focal spot is distorted, as shown in Fig. 44, where the distorted focal spots for the

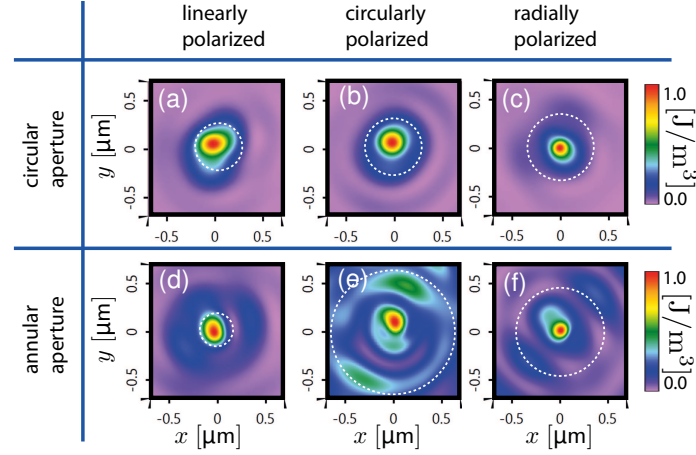


Figure 45: Distorted energy densities obtained by focusing through the spherical micro-/nano-particles by a real lens with misalignment of the source of  $-200 \mu\text{m}$  and  $200 \mu\text{m}$  in  $x$  and  $y$  directions respectively.

cases of circular (a)-(c) and annular (d)-(f) aperture are shown, for a source which has been shifted by  $200 \mu\text{m}$  in negative  $x$  direction and positive  $y$  direction with respect to the optical axis of the lens system.

The corresponding deviation from the ideal lens case is  $\sigma^{\text{dev}} = 0.9\%$  for the circular-aperture case and  $\sigma^{\text{dev}} = 2.8\%$  for the annular-aperture case, when the incident field is linearly polarized as shown in Fig. 44 (a) and (d). The values of the deviation from the ideal lens case are  $\sigma^{\text{dev}} = 1.0\%$  and  $\sigma^{\text{dev}} = 3.1\%$  for the circular-aperture and the annular-aperture respectively, when the incident field is circularly polarized as shown in Fig. 44 (b) and (e). The conclusion is reached that the small rotationally symmetric focal

spot obtained with the annular aperture is sensitive to the misalignment and not easy to obtain experimentally, even though it is predicted by the aplanatic lens model. The values of the deviation from the aplanatic lens case are  $\sigma^{\text{dev}} = 1.5\%$  and  $\sigma^{\text{dev}} = 3.3\%$  respectively, when the incident field is radially polarized as shown in Fig. 44 (c) and (f). If the shift of the source is increased, the focal spot becomes even more distorted. The details are discussed in [98].

#### 4.4.2 Focusing through a micro-/nano-particle

Then the distorted focused spots are focused through the previously investigated spherical, disk-shaped and cuboid micro-/nano-particles. The center of the micro-/nano-particles coincides with lateral position where the maximum value of the distorted spots are, as shown in Fig. 44. The focal spots behind the micro-/nano-particles are shown in Fig. 45 for spherical, and in Fig. 46 and Fig. 47 for disk-shaped and cubic micro-/nano-particles respectively. It is seen that the tiny focal spots are also distorted as expected. But the tiny-focal-spot property is still obtained.

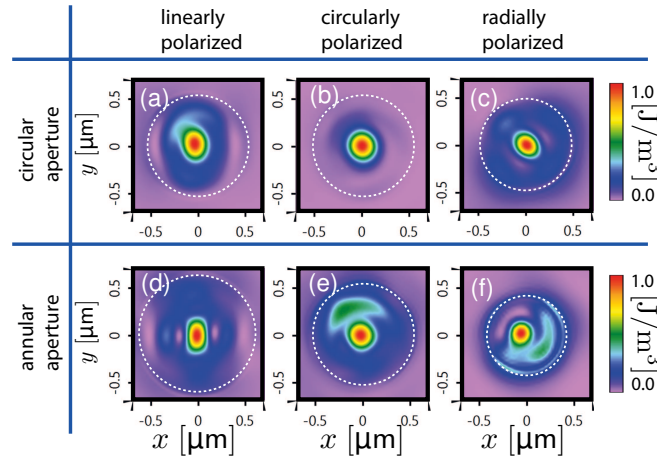


Figure 46: Distorted energy densities obtained by focusing through the disk-shaped micro-/nano-particles by a real lens with misalignment of the source of  $-200\ \mu\text{m}$  and  $200\ \mu\text{m}$  in  $x$  and  $y$  directions respectively.

#### 4.5 SUMMARY AND CONCLUSION

The focusing of linearly, circularly and radially polarized beams through spherical, disk-shaped and cuboid micro-/nano-particles with the sizes comparable to the wavelength are investigated by idealized aplanatic lens. The tiny focal spots are generated behind the variously shaped micro-/nano-particles. The size of the tiny focal spots can be achieved to  $\sim 0.05\ \lambda^2$  when the radially polarized beam and spherical micro-/nano-particles are applied. Linearly and circularly polarized beams combined disk-shaped and cuboid shaped micro-/nano-particle also generate tiny focal spots which are beyond the diffraction limit.



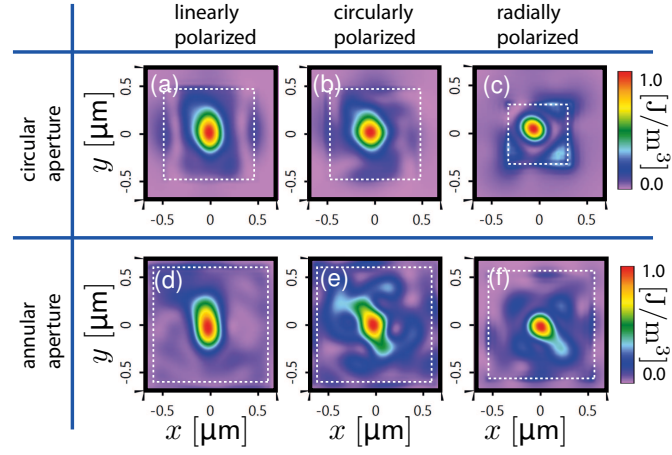


Figure 47: Distorted energy densities obtained by focusing through the cuboid micro-/nano-particles by a real lens with misalignment of the source of  $-200 \mu\text{m}$  and  $200 \mu\text{m}$  in  $x$  and  $y$  directions respectively.

An corresponding analysis to the idealized aplanatic lens is also performed, which fully considers the structure of the real lens system for the influence of, e.g. the misalignment of the system. It is found that the real lens system distorts the tiny focal spots due to the misalignment of the source. But they are still tiny spots beyond the diffraction limit in the investigated cases.





## 5.1 INTRODUCTION

As it is mentioned in chapter 1, Fourier microscopy, which is sometimes referred to as back focal plane imaging [212, 213], has gained attraction due to its ability of producing a direct visualization of the angular distribution (spatial frequency) of scattered light with high spatial resolution. During the last two decades it has been widely used in various fields of optical science, especially in nanooptics and in material science.

Among lots of other applications, e.g. imaging of surface plasma [25, 214–217], viewing angle measurement of displays [218], etc., it is very often applied to: 1) imaging the emission diagram of a single molecule, e.g. to retrieve its orientation [24, 65, 70, 219–221], or to reconstruct the sub-wavelength period of a Photonic Crystal (PhC) illuminated by the emitted light [15, 35, 222–227]; and 2) the direct angular-spectral analysis of a PhC to measure its dispersion relation [26, 82, 213]. In the case of imaging of the emission diagram of a single molecule to retrieve its orientation, the experimental results of the emission diagram are fitted to the closest one obtained by a theoretical calculation based on an ideal lens model [65, 70]. In the case of imaging of the emission diagram to reconstruct the period of a PhC illuminated by the emitted light, an ideal lens model is also used to obtain the Fourier image simply by taking the square of the amplitude of the Fourier-expanded electric field [223, 224]. In the case of a spectral analysis of a PhC, the Fourier microscopy system is combined with a spectrometer in order to obtain the full angular and spectral distributions with ease. All of the complex lens systems are assumed ideal and work perfectly.

However, the real lens systems, consisting of complex optical surfaces, will almost certainly fail to perform ideally in reality during the experiment. Aberrations, misalignment and the vectorial properties of the complex surfaces of the real lens system always have an impact on the experimental results which need to be considered. A ray tracing method has been applied in literature [56] to analyze the performance of the different configurations of real objective and tube lenses. But the polarization effects, e.g. of the dipole source, on the amplitude of the field are not included [68]. In addition, the diffraction from the PhC or the spectrometer grating is also not included. Therefore, a fully vectorial physical-optics modeling is desired for the real lens system, especially one which allows for the inclusion of nano-structures, e.g. the PhC or the spectrometer grating.

Bear this in mind, in this work, the fully vectorial physical-optics modeling of the entire Fourier microscopy system is performed with real lenses [228]. And the nano-structures are also included in the simulation, e.g. the PhC and the spectrometer grating, in the entire real-lens-based Fourier microscopy system. The whole modeling is performed in the framework of field tracing by connecting different field solvers, and is applied to two different applications: 1) the emission diagram of a single molecule and 2) angular-

spectral analysis of a photonic crystal.

This chapter is structured as: in Sec. 5.2 modeling tasks and techniques are summarized by the field tracing diagram; in Sec. 5.3 the numerical results for the emission diagram of a single molecule are presented and analyzed; in Sec. 5.4 the numerical results for the angular-spectral analysis of a PhC are presented and analyzed. Sec. 5.5 summarizes and concludes the chapter.

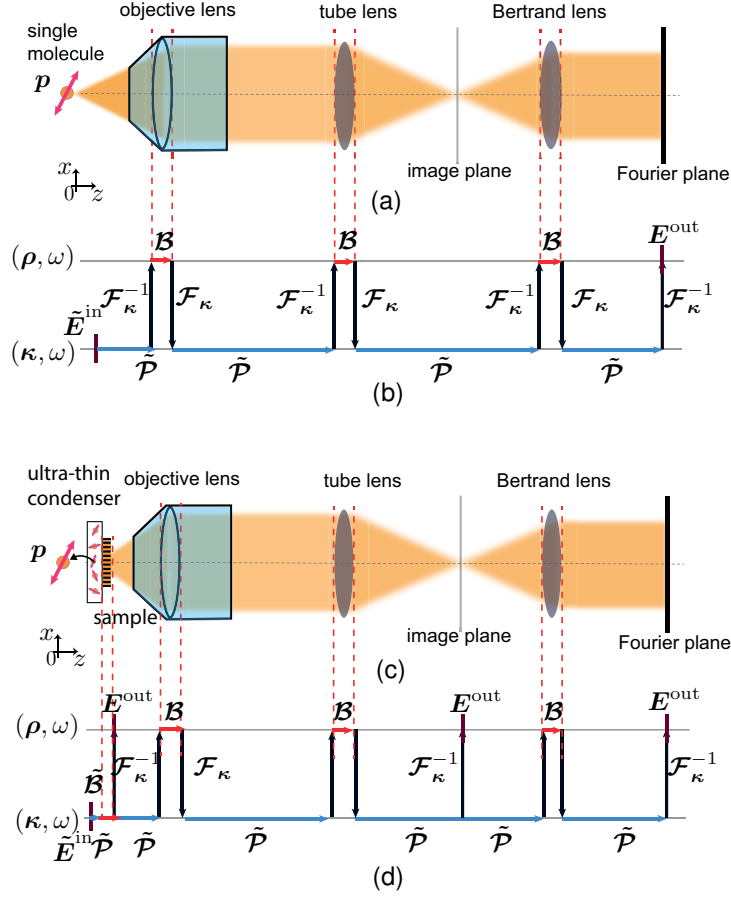


Figure 48: (a) and (b) show the schematic of the Fourier microscopy system for imaging the emission diagram of a single molecule and through the PhC respectively. (b) and (d) are the corresponding field tracing diagrams.

## 5.2 MODELING TASKS AND TECHNIQUES

In both applications, the imaging systems are based on mapping the back focal plane of a front objective lens; the optical systems, shown in Fig 48 and Fig. 49, are known as “Fourier imaging microscopy systems”. The Fourier microscope considered here consists of a high numerical-aperture (NA) objective lens, a tube lens and a Bertrand lens. The front focal plane of the tube lens coincides with the back focal plane of the objective [24, 56]. Fourier image is formed at the back focal plane of the Bertrand lens: this

plane is called the Fourier plane.

In the application of imaging the emission of diagram of the single molecule to retrieve its orientation, the emission of the fluorescent single molecule is modeled by a dipole source as indicate in 48 (a). It propagates through the Fourier imaging microscopy sys-

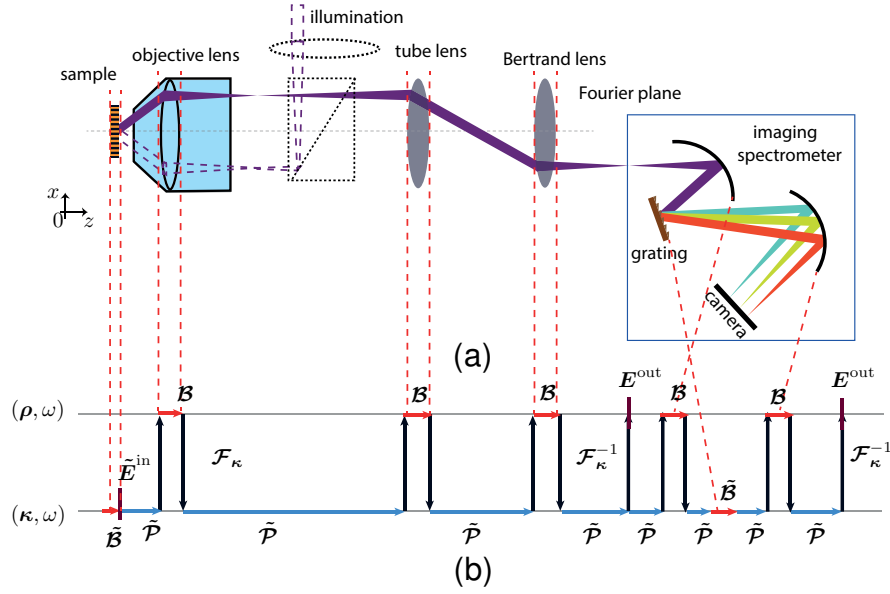


Figure 49: (a). The schematic of the Fourier microscope combined with spectroscopy, based on a real lens system for the spectral analysis of a PhC. (b). The corresponding field tracing diagram explaining the vectorial field propagation through the Fourier microscope combined with spectroscopy.

tem and has the image at the Fourier plane, where the camera detector is placed. The image, which is defined as energy density, is captured.

In the application of imaging of the emission diagram of a molecule through the PhC to reconstruct its period, a schematic of which is shown in Fig. 48 (c). The so-called ultra-thin condenser is a layer of randomly distributed fluorescent molecules embedded in a PMMA layer and located in the near-field region of the PhC. The PhC is the sample, which is to be observed by the Fourier microscopy system. It is nanostructured and periodic. Again, the emission of the fluorescent single molecule on  $z$  axis is modeled by a dipole source as indicate in 48 (c). Then it illuminates the PhC in the near field. The diffracted light from the PhC is collected by the Fourier imaging system and is imaged at the Fourier plane.

In the application of angular-spectral analysis of the PhC shown in Fig. 49 (a), with the illumination light reflecting from through the PhC, which is also used as the sample in the entire system. After propagating through the Fourier microscope, the light propagates further through the spectrometer, which consists of parabolic mirrors and a grating, to the detector plane.

The corresponding entire modeling procedures are indicated in the field tracing diagram as shown in Fig. 48 (b), Fig. 48 (d) and Fig. 49 (b) are summarized briefly in Tab.4:

Please note that when certain diffraction orders are taken from the PhC and spectrom-

Table 4: Summary of the applications of field tracing techniques. SG: Spectrometer Grating

			$\mathcal{B}$	$\tilde{\mathcal{B}}$ : PhC/SG	$\mathcal{F}_\kappa \& \mathcal{F}_\kappa^{-1}$
application 1	retrieve orientation of a single molecule Fig. 48 (a) and (b)	without lens	no	no/no	no
		ideal lens	ideal	no/no	HFT&IHFT
		real lenses without diffraction	real	no/no	HFT&IHFT
		real lenses with diffraction	real	no/no	HFT&IHFT but FFT&IFFT for last pair
	reconstruct period of a PhC Fig. 48 (c) and (d)	near field space domain	no	real/no	IFFT
		near field Fourier domain	no	real/no	no
		far field image plane	real	real/no	HFT&IHFT but IFFT for the last one
		far field Fourier plane	real	real/no	HFT&IHFT
application 2	angular-spectral analysis of a PhC Fig. 49 (a) and (b)	Fourier microscope	real	ideal/no	HFT&IHFT but IFFT for the last one
		Fourier microscope + spectrometer	real	ideal/real	HFT&IHFT but IFFT for the last one
		entire system	real	real/real	HFT&IHFT but IFFT for the last one

eter grating, combined with the all HFT are performed, the entire modeling procedure is point-wise. This facilitates the modeling of the entire system in a computationally efficient manner.

### 5.3 EMISSION DIAGRAM OF A SINGLE MOLECULE

To measure the angular distribution of the emission pattern of single molecule, or scattering diagram of single nano-objects, a back focal plane imaging technique is applied which is experimentally realized via a Fourier microscopy system. The optical components of the system evidently influence the field as it propagates through them. Consequently, the back focal plane image obtained at the Fourier plane can deviate from the actual far-field angular pattern of single molecules or nano-objects; it can even be significantly distorted.

### 5.3.1 Without lens vs. ideal lens vs. real lens

To address this issue, the emission pattern of a single molecule is imaged via a Fourier microscopy system using different levels of approximation - i.e. with ideal and real lenses. The ideal lens satisfies the Abbe's sine condition and assumes the energy conversation propagating through the Gaussian reference sphere [70, 98]. The real lens consists of complex surfaces [56]. The anti-reflection coating is not included in the model used in this paper because of the lack of the data from the manufacturers. Firstly, the energy density predicted by an ideal lens model is compared with the energy density without any lenses, purely in the Fourier domain, which is the actual characteristic of the emission pattern. Then the energy density based on an ideal lens model is compared with the energy density when the real lenses are considered, to evaluate the deviation.

The single molecule is in the front focus of the objective lens and the energy density distribution at the Fourier plane (Fig. 48 (a)) is calculated assuming a dipole source with different dipole moment orientations  $\mathbf{p} = [p_x, p_y, p_z]$  (Fig. 50 (a) and (b)). The emission wavelength is 587.5nm in accordance with [56], where the real lens data is from. The single molecule is embedded in the medium which has the refractive index  $n = 1.52$ . The simulated images are shown in Fig. 50 (c) and each image is normalized to its maximum value. The units of the axes in the images corresponding to the Fourier domain without lens have dimensions of spatial frequency, and they are related to the spherical coordinates by  $k_x = k_0 n \sin \theta \cos \phi$  and  $k_y = k_0 n \sin \theta \sin \phi$ , where  $k_0$  is the wavenumber in vacuum.  $n$  is the refractive index of the surrounding medium.  $\theta$  and  $\phi$  are the inclination angle and azimuthal angle respectively as indicated in Fig. 50 (a). The units of the axes in the images corresponding to the ideal and Olympus lenses have the dimension of spatial coordinates and they are related to the spherical coordinates by  $x = f n \sin \theta \cos \phi$  and  $y = f n \sin \theta \sin \phi$ , where  $f$  is a constant related to the focal lengths of the objective, tube and Bertrand lenses.

The study is started by comparing the energy density distribution at the back focal plane of the ideal lens with that of the dipole field at the focus in the Fourier domain (Fig. 50 (c), upper two rows). These images are filtered with an NA=1.4 in order to make them comparable with the simulation of the real system (which has the same value of the NA), which is also in accordance with the numerical aperture used in the experimental results of [229].

With increasing wave-vector, which corresponds to a larger emission angle, the dipole energy density in the Fourier domain exhibits a significantly higher deviation with respect to that at the back focal plane of the ideal lens [70]. It is attributed to the pronounced longitudinal field presented at the origin of the dipole. In the meantime the field at the back focal plane contains no longitudinal field because of the crosstalk between the transversal field component and the longitudinal one, when the vectorial field propagates through the ideal lens according to energy conservation [65, 98, 229]. Obviously, there is an evolution of the energy density in the Fourier domain related to the ratio of transversal and longitudinal fields as they transform through the lens to the back focal plane. The emission pattern of the dipole source has a toroidal shape, with an axis coinciding with the direction of the dipole moment: the energy density has maximum value at the perpendicular direction ( $x$  direction in Fig. 50 (c) second of

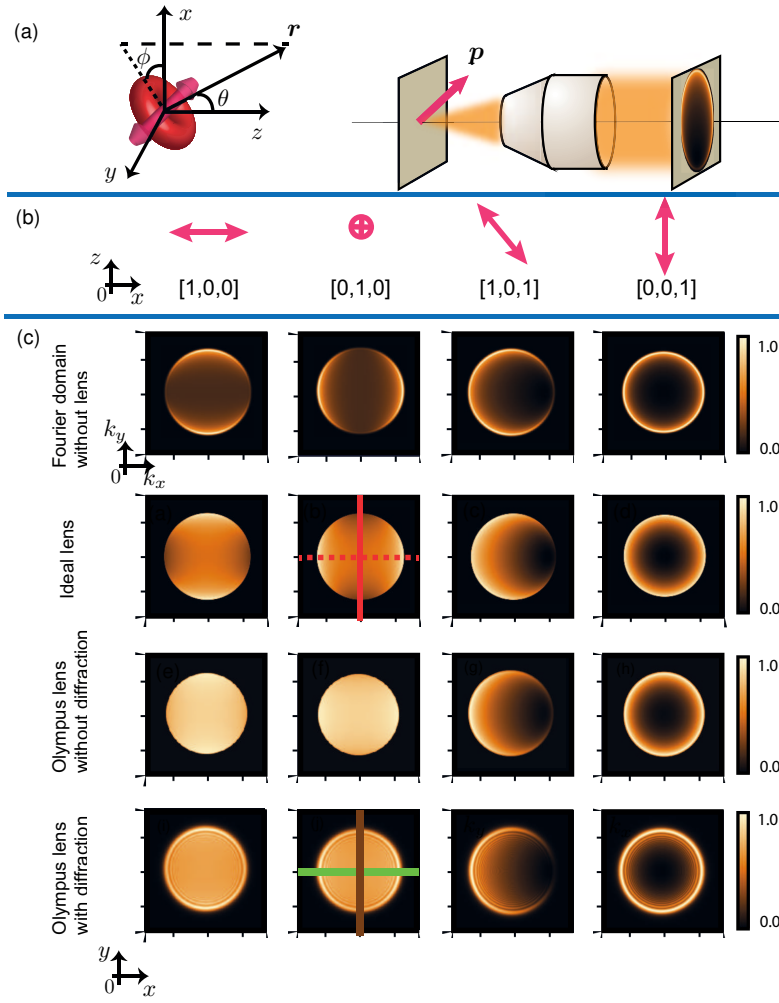


Figure 50: (a). Schematic to show the dipole orientation  $\mathbf{p}$  and the position  $\mathbf{r}$ . (b). Dipole orientations under investigation. (c) shows the energy density of a dipole without a lens, by ideal or real lens.

the first row) and minimum along the direction of the dipole moment ( $y$  direction in Fig. 50 (c) second in the first row). The ideal lens also demonstrates a similar behavior: pronounced emission along  $x$  (Fig. 50 (c) second in the second row) and significantly less along  $y$  (Fig. 50 (c) second in the second row).

In the next step the performance of a real system is compared with the ideal lens. As the specific real system a Fourier microscopy system is taken, consisting of commercial optical lenses: an Olympus 60X (US 5517360) objective lens and an Olympus tube lens. The data of these lenses is taken from [56]. This objective lens is chosen, in order to compare the simulation results with the experimental ones reported in [229]. A Thorlab lens AC254-200-B serves as the Bertrand lens in this system.

The back focal plane image is obtained by calculating the energy density at the Fourier plane as shown in Fig. 48 (a). In order to understand the influence of the real system on

the information obtained at the Fourier plane, the beam propagation is modeled, with and without the diffraction effects of the system respectively. In the real system the Fourier plane image appears not to have a very pronounced difference between the two perpendiculars directions (Fig. 50 (c) second in the third row). That means the image obtained at the Fourier plane of the real system differs significantly from the angular distribution of the emission of the single molecule at the focus of the collecting objective lens. The difference is caused by the performance of the optical components in the real system, particularly by Fresnel losses [229], various aberrations etc.

The distortion of information in the angular emission pattern at the Fourier plane is even more strongly pronounced when diffraction is taken into account in the calculation. (Fig. 50 (c) second in fourth row, Fig. 51 (a)). The curves in Fig. 51 (a) show strong oscillation with increasing angle, which is in relatively good agreement with the experimental results reported in reference [229] shown in Fig. 51 (b). This oscillating behavior is deceptive: one could naively attribute it to the emission pattern of the single molecule, which means energy density oscillation versus angle, whereas in reality they are caused by the diffraction presented in the optical system; in other words, these are measurement artifacts. The oscillating pattern (ring pattern in the images) originates mostly from the aperture of the objective, since the apertures of the tube and Bertrand lenses have a larger diameter than the beam.

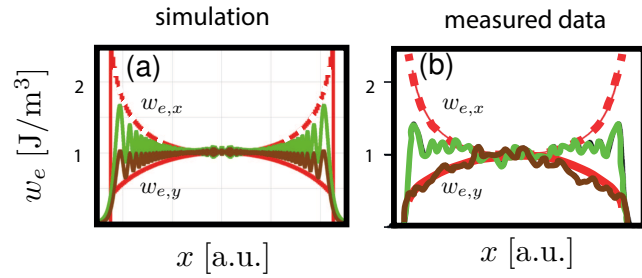


Figure 51: Comparison of the simulation results with the experimental results from literature. (a). The extracted profiles from Fig. 50 (c) with the corresponding colors and shapes. (b). The adapted results from literature [229] to show corresponding experiment results.

### 5.3.2 Performance of different real lenses

Observing the strong difference between the performance of the ideal lens model and the real lens system, as well as between the actual emission pattern of a single molecule and the distorted information retrieved of it which is obtained at the Fourier plane, raises the question of whether there is a real objective lens that can exhibit a performance similar to the ideal one. Having this in mind, the Fourier plane images are compared which are calculated for four Fourier microscopy systems consisting of objective lenses with different magnifications and numerical apertures with corresponding tube lenses by the same manufacturers as the objective lenses; the Bertrand lens is the same in all four configurations. The results are shown in Fig. 52. The first aspect that is noticeable



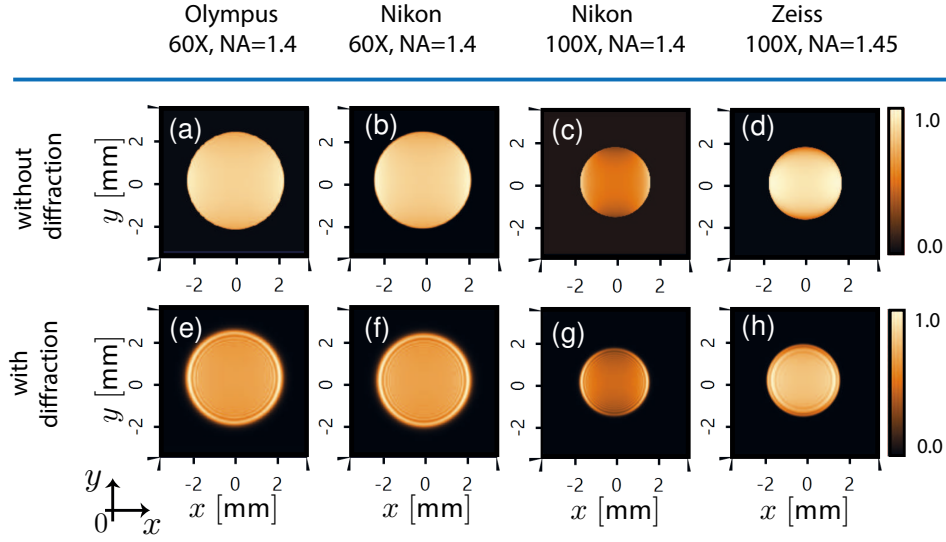


Figure 52: The images at the Fourier plane with different commercial lenses, with  $\mathbf{p} = [0, 1, 0]$ . (a)-(d) are without inclusion of diffraction from the commercial lens systems: (e)-(h) The corresponding images with diffraction from the apertures of the objective lenses.

is the difference in the sizes of the Fourier images, a characteristic which is related to the numerical aperture and the magnification of the objective lens by  $D = 2f^{\text{Ber}}\text{NA}/M$ , where  $f^{\text{Ber}}$  is the focal length of the Bertrand lens and  $M$  is the magnification. In order to compare the images from the different Fourier microscopy systems as well as that of the ideal lens, the profiles are extracted at the center position of Fig. 52, as shown in Fig. 53. As can be seen, the simulated image at the Fourier plane obtained by the system with one of the objective lenses, the Nikon 100X NA=1.4, is closest to the back focal plane image of the ideal lens. The reason is that the design of this lens makes the local incident angles through all of the surfaces of the objective lens small. Therefore, the transmittance, which is governed by Fresnel coefficients [98, 230], is distributed relatively evenly for small local incident angles. Following this logic, we can deduce that all of the above-mentioned objective lenses would perform closer to the ideal lens if well-performed anti-reflection coatings are applied. However, the well-performed anti-reflection coatings for large angular and spectral range and for all the polarizations are difficult to be realized both technically and economically.

### 5.3.3 Propagation through photonic crystal

In what follows the emission pattern of a single molecule in front of the 1D PhC structure is studied shown in Fig. 48 (c). In the simulation a single molecule with two possible dipole moment orientations is considered: parallel and perpendicular to the PhC lines. The results are shown in Fig. 54 and Fig. 55 for the two different orientations respectively. In the model the location of the fluorescent molecule is assumed on the optical

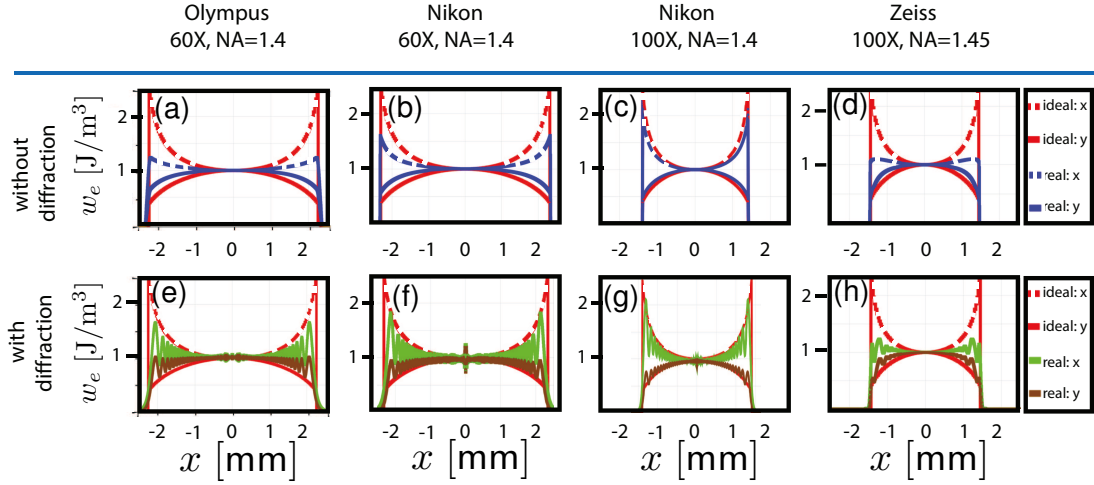


Figure 53: (a)-(d). The energy density profiles at the center position corresponding to Fig. 52 (a)-(d) with dashed and solid blue curves in  $x$  and  $y$  directions. The profiles corresponding to the ideal lens (Fig. 50 (c)) are also added for comparison. (e)-(h). The energy density profiles at the center position of Fig. 52 (e)-(h).

axis ( $z$  axis) and 110 nm in front of the PhC. The PhC is a 1D wire grating which is invariant in  $y$  and periodic in  $x$  with a period of 300 nm. It is made of chromium with a thickness of 15 nm. The duty cycle is 50%. The chromium layer is directly deposited on a glass substrate without any adhesion (intermediate) layer. The Fourier microscopy system is the one based on the Nikon system with an objective of 100X and NA=1.4, the one found to perform closest to the ideal lens, but for the Fourier plane image the effective NAs are chosen to be 1.3 and 0.9 in order to be in accordance with the configurations used in [227]. In order to analyze the imaging of the PhC by the illumination of the emission field of the dipole, only the  $\pm 1$  diffraction orders of the PhC are used. By interference of these two orders, the image of the photonic crystal is formed at the image plane as shown in Fig 48 (c).

The images shown in Fig. 54 in different columns correspond to different values of NA (decreasing from left to right): with evanescent waves, without evanescent waves for NA=1.3 and NA=0.9. It is obvious that decreasing the NA results in loss of detail as well as a decrease in the contrast as shown in first and third rows. The images for NA=1.3 and 0.9 at the image plane are 100X magnified images of the one at the front focal plane (in the near field) of the objective. The direct correspondence to the energy density with evanescent wave is more obvious compared with the images resulting from the molecule orientation perpendicular to the PhC lines as shown in Fig. 55 first row. This could be related to the plasmonic effects leading to a strong longitudinal component and surface plasmon polaritons propagating along the surface and dissipating most of the energy, and therefore not coupling to radiative modes, which would be collected by the objective lens. This idea is supported by the Fourier domain image calculated with evanescent waves (Fig. 55 first in the second row): it shows that the energy

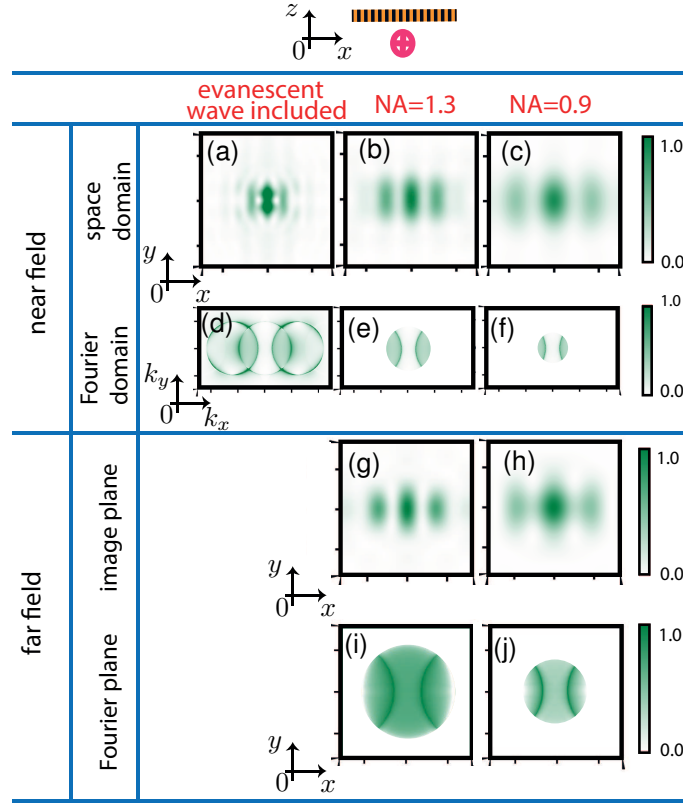


Figure 54: The images, in the near and far field, are for an illuminating molecule with orientation parallel to the PhC lines.

is concentrated mostly outside of the central ring, that is at large  $k$  vectors, whereas in case of parallel orientation (Fig. 54 first in the second row), most of the energy is in the central ring, thus mostly radiative modes.

The PhC structure can strongly modify the emission pattern of the single molecule; in addition to that, the real Fourier microscopy system can also introduce artifacts. Thus by interpreting the Fourier plane image that corresponds to the back focal plane image, in other words the angular distribution of the emission pattern collected by the objective, one has to carefully analyze all the steps to spot the artifacts and understand the relationship between the energy in the Fourier domain in the near field and the emission pattern at the Fourier plane in the far field.

#### 5.4 ANGULAR-SPECTRAL ANALYSIS OF PHOTONIC CRYSTAL

As it is seen in the previous section, a PhC influences the emission pattern of a single molecule via the interaction of the light emitted by the molecule with the photonic properties of the PhC. This interaction depends on the properties of the single molecule (such as the dipole moment orientation, emission wavelength, distance between single molecule and PhC), as well as on the spectral properties of the PhC. Said spectral proper-

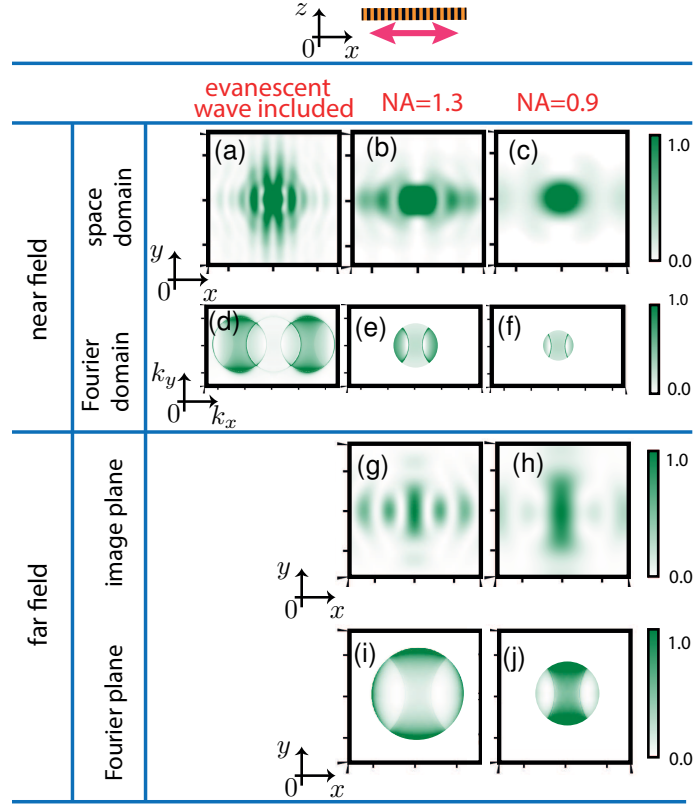


Figure 55: The corresponding results to Fig. 54 with the orientation of the illuminating molecule perpendicular to the PhC lines.

ties are described by the dispersion relation: energy dependence on wave-vector, which can be translated as energy dependence on wavelength. For the spectral analysis (measuring the dispersion relation) of the PhC, the Fourier microscope is connected to an imaging spectrometer with a camera detector at the output. In this case, the complexity of the system increases, since optical elements with dispersive and diffractive properties are involved in the light path, e.g. spectrometer diffraction grating.

In order to understand the influence of the dispersive and diffractive effects of the sample and the lens system separately, the whole system is modeled step by step by assuming, first, the PhC as an ideal optical component (meaning the reflectance is the same for the entire range of incident angles and across the entire spectral range under investigation). The spectrometer is not included. These assumptions allow us in the first step to observe solely the influence of the Fourier microscope system on the final image. In the second step, the real spectrometer is put into the beam path by considering mainly the diffraction grating with different efficiencies for TM and TE polarizations. In the third step, the ideal PhC is replaced with a real one, which means its reflectance is modeled with FMM, taking into account its physical parameters. Thus in this final step the entire system is modeled with real components.

In order to evaluate our simulation results considering the real lenses, the simulation

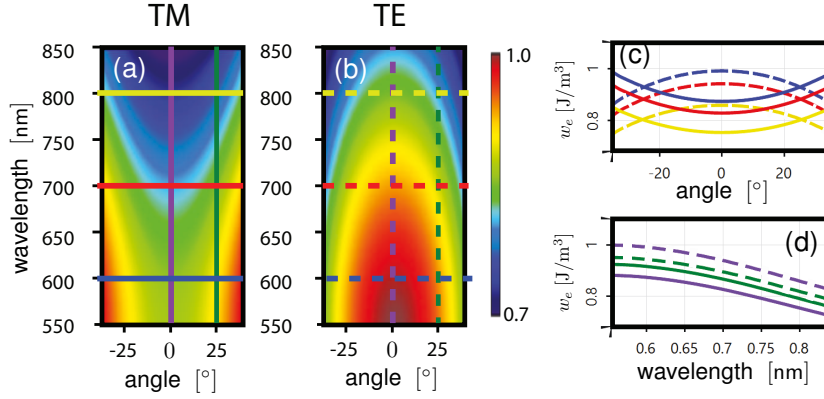


Figure 56: (a)-(b). The energy density at the Fourier plane for TM- and TE-polarized incidence. (c). The horizontal cross-sections of the 2D plots (a) and (b), representing the angle dependence of the real lens system for TM and TE. (d). The vertical cross-sections of the 2D plots (a) and (b) representing the wavelength dependence of the real lens system for TM and TE.

results are compared with experimental data published in [82]. Consequently, the experimental conditions used in the reference 8s followed: the incident beam is a plane wave with incident angles from  $-36^\circ$  to  $36^\circ$ , the wavelengths range from 550 nm to 850 nm. The PhC is a 1D wire grating made of palladium deposited on a gold mirror with thickness of 200 nm with a 35 nm  $\text{Al}_2\text{O}_3$  spacer in between, whose refractive index is 1.75 [82]. The period of the palladium grating is 300 nm in  $x$  direction, the wire width is 85 nm and the height 30 nm. The whole structure is on a glass substrate. The objective lens is not exactly the one used in [82] for lack of lens data. Instead, Nikon 20X with  $\text{NA}=0.75$  (US patent 5729391) with a Nikon tube lens is chosen. The Bertrand lens is from Thorlabs: a double achromat with 200 mm focal length (AC254-200-B). The spectrometer grating is made of silver and blazed with an angle of  $17^\circ$  and has a period of 920.15 nm. In the simulation the illumination is assumed to be a plane wave impinging from the objective lens on a sample. The reflected (or back-scattered) light is collected by the same objective lens, propagates through the optical system and is imaged onto a spectrometer camera detector. The incident angle is scanned in the range of  $(-36^\circ, +36^\circ)$ ; the scanning direction is in the incident plane. The incident plane is perpendicular to the PhC (the palladium grating).

To achieve such an illumination experimentally, one can focus the beam at the back focal plane of the objective lens and scan the focus point along the line in the back focal plane similar to total internal reflection (TIRF).

#### 5.4.1 Fourier microscope

The results of the first step, where the PhC has uniform reflection across the entire angular and spectral range, are shown in Fig. 56 (a) and (b): for TM and TE polarized incident beams respectively. TM polarization is that the electric field is contained in

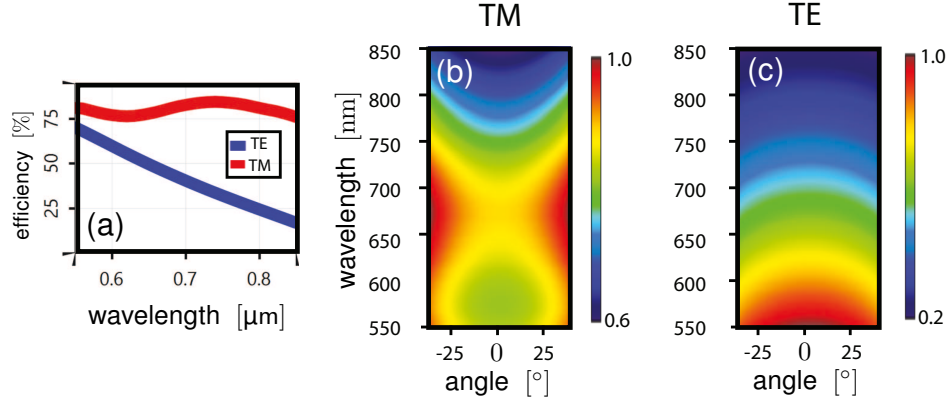


Figure 57: (a). The diffraction efficiency of the real grating of the spectrometer. (b)-(c). The energy density at the detector of the spectrometer for TM- and TE-polarized incident light.

the plane of incidence. The uneven distribution over the incident angles, as shown in Fig. 56 (c), originates from the different Fresnel coefficients at the optical surfaces of the lenses, for different angles and different polarizations. The uneven distribution over the wavelengths, as shown in Fig. 56 (d), is caused by the chromatic aberration of the lens system. In this step the angular and spectral characteristics solely of the Fourier microscope is determined.

#### 5.4.2 Fourier microscope and spectrometer

In the second step the effects of the spectrometer is included by assuming a blazed grating in the spectrometer with different diffraction efficiencies (Fig. 57 (a)) for +1 order of TE and TM polarizations. The unevenness of the energy densities at the detector of the spectrometer is further increased by the influence of the grating of the spectrometer (Fig. 57 (b) and (c)). It can be interpreted simply that the results are obtained via multiplication of Fig. 56 (a) and (b) with the diffraction efficiency of the blazed grating.

#### 5.4.3 Entire system

Finally, in the third step polarization and the angular-spectral dependence of the PhC reflectance are included. The calculation of the reflectance is shown in Fig. 58 (a) and (e). The results for TM and TE polarizations are shown in the upper and lower rows, respectively, in Fig. 58. Here, again, it is advanced step by step: first calculating the reflectance of the PhC (Fig. 58 (a) and (e)), then propagating through the Fourier microscope without including the spectrometer (Fig. 58 (b) and (f)). Afterwards the real diffraction grating in the spectrometer (Fig. 58 (c) and (g)) is included and finally the sample is tilted by 5° about the  $y$  axis, which is along the PhC lines (Fig. 58 (d) and (h)). By comparing Fig. 58 (a) and (b), it is seen that the energy density experiences an obvious decrease over wavelengths of approximately 780 nm indicated in the black

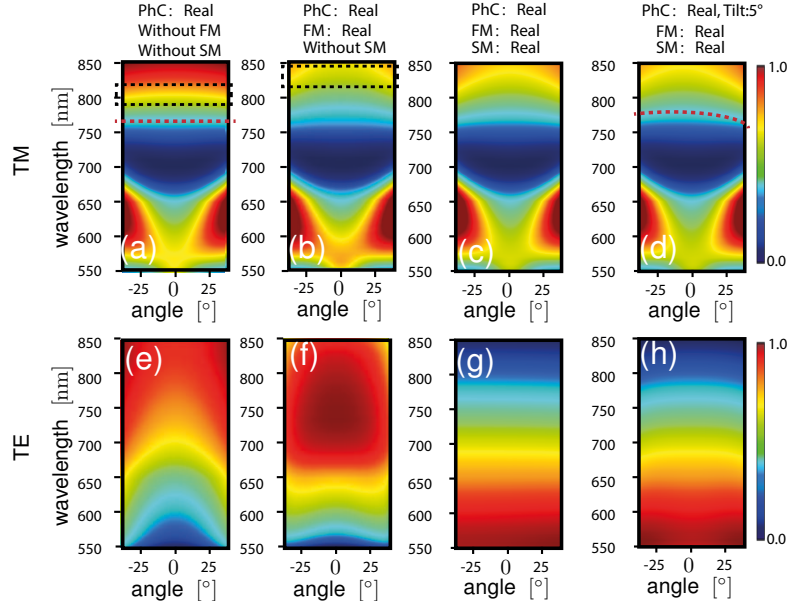


Figure 58: (a). The reflectance of the real PhC. (b) The energy density at Fourier plane. (c). The energy density on the detector of the spectrometer including the effect from the real grating. (d). The misalignment of the sample (PhC) by rotation  $5^\circ$ . (e)-(h). The corresponding results to (a)-(d) in the case of TE polarization. FM: Fourier Microscopy and SM: Spectrometer.

dashed-line box, caused by the chromatic aberration observed in Fig. 56 (a) and (d). The comparison of Fig. 58 (b) and (c) demonstrates the small influence of the diffraction efficiency of the grating for TM polarization. The influence of the diffraction grating is pronounced for TE polarization, as evidenced by comparison of Fig. 58 (f) and (g): the energy density decreases with increasing wavelength. When the PhC is tilted by  $5^\circ$  about the  $y$  axis, the energy density also changes slightly and becomes asymmetric indicated by the red dashed curve (Fig. 58 (d) and (h)).

In order to evaluate our simulation results, they are compared with the experimental results reported in [82]. By comparison of Fig. 59 (a) and (b), the decrease in the energy density for wavelengths over 780 nm is demonstrated both by the simulation result and the experimental results, as shown in the black dashed-line boxes. The asymmetries of the distribution of the energy density are demonstrated both by the simulation and the experimental results as shown by the tilted red dashed curves. They are in good agreement.

## 5.5 SUMMARY AND CONCLUSION

The fully vectorial physical-optics modeling of entire Fourier microscopy systems is modeled based on real lenses for the first time in literature. The rigorous modeling of the samples, which are nanoscale structures, is included in the real lens system, which is also a novel result. The modeling to two typical applications are performed: observation



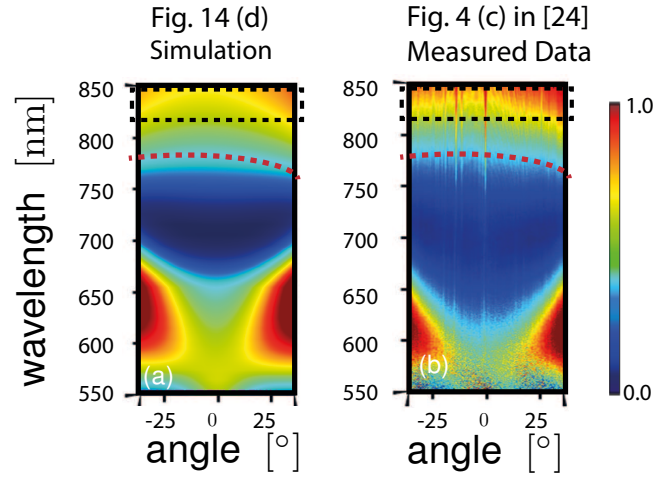


Figure 59: Comparison of the results with those in [82]. (a). The same figure as Fig. 58 (d) to show the results including the effects from the Fourier microscopy, spectrometer and the misalignment of the sample. (b) shows the experimental result adapted from [82].

of the emission diagram of a single molecule and angular-spectral analysis of a photonic crystal. The influence of the samples and the real lens systems on the final results are analyzed separately and combined at our own discretion.

By simulating the beam propagation with various kinds of polarizations through the optical system, it determines the complete angular and spectral characteristics of the system. The different physical effects which arise experimentally can be assigned to their cause simply by, in the simulation, idealizing all the components in the system except one, thus isolating that specific physical phenomenon and correlating it to the component which causes it. Therefore, the simulation results can be correlated with the measured results on demand to guide the setting of the experimental setup or analyze the experimental results.





## 6.1 INTRODUCTION

As it was mentioned in chapter 1, the Structured Illumination Microscopy (SIM) [38, 40, 41, 231] is one of the widely used techniques in life science which provides high resolution, by shifting the higher spatial frequency information into the bandpass of the lens system.

It was first proposed by Heintzmann et al. [40] and Gustafsson [41] for imaging high-resolution two-dimensional (2D) structure with One-Photon Excited Fluorescence (OPEF). The improvement of the lateral resolution is by a factor of 2 with linearly excitation between the energy densities of the excitation light and the emitted light. Please note that energy density is often referred to intensity in the life science community. Alternatively, by the non-linear excitation between the energy densities of the excitation light and the emitted light, the improvement of lateral resolution is unlimited in theory [232, 233]. Later on, it was extended to three-dimensional (3D) structure with OPEF in the linear excitation case which improves both of the resolutions in lateral and axial directions [234–236].

However it still suffers from the low signal-to-noise ratio when imaging the thick samples. This issue is solved as the advances of the Multi-Photon Excited Fluorescence (MPEF) [52, 237–239], usually Two-Photon Excited Fluorescence (TPEF) in practice, with the inherently advantages: 1) deep penetration depth for imaging thick samples, 2) lower out-of-focus excitation. It allows the imaging of deep biographic sample with higher signal-to-noise ratio. The excitation light of the MPEF is often pulsed laser with temporal focusing in practice in order to provided sufficient energy for the excitation [240–245].

Therefore, the combination of SIM and MPEF can make full use of the advantages of both techniques with higher resolution as well as deep penetration and high signal-to-noise ratio. The temporal focusing and the spatially structured illumination are achieved at the focal plane. The temporal spectral is generated by a grating or Digital Micromirror Device (DMD) and recombined by the objective lens at the focal plane [246–250]. The two-dimensional structured illumination is generated by projecting two-beam-interference pattern at the focal plane from the perpendicular direction to the temporal focusing [246, 247]. The three-dimensional structured illumination is generated following an analogous logic [246, 251–253], with the purpose of improving the axial resolution.

In both OPEF and TPEF cases, the reconstruction algorithm in the post computing often assumes the structured illumination as a perfect interference pattern, i.e., via the interference of coherent plane waves in the focal plane. However, the real experimental system, which possesses a complex configuration (Fig. 60) in OPEF-2D-SIM case, depends on several effects, such as the polarization of the field, the diffraction from an aperture, the inclined incidence on the blazed grating. These effects can cause the low

contrast and inhomogeneity of the illumination pattern.

More complex configurations (Fig. 61 and Fig. 62) are applied in TPEF 3D-SIM. Besides

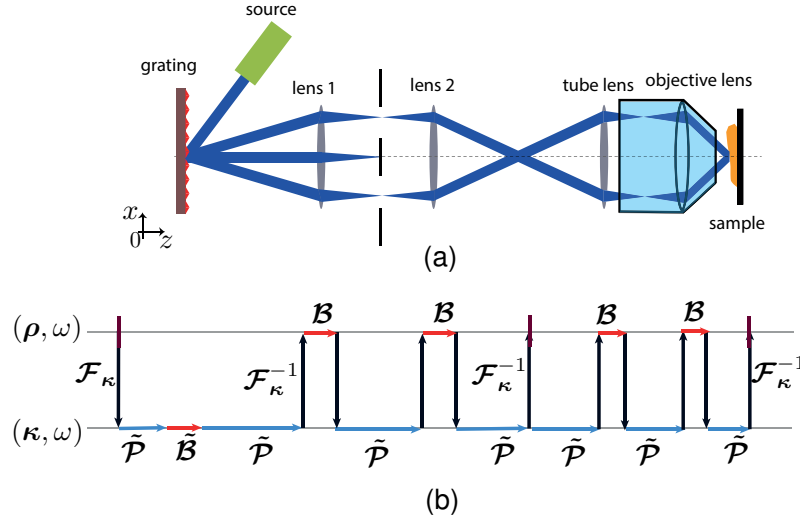


Figure 60: (a). Schematic of the configuration of microscopy system with structured illumination. (b). The corresponding field tracing diagram.

the above mentioned physical effects, the temporal focusing effect, the aberration from the lens system, the misalignment of the lens system, etc., also have an influence of the contrast and the inhomogeneity of the structured illumination pattern. Therefore, they should be analysed and accounted for properly.

In this chapter, the two cases are considered, OPEF 2D-SIM and TPEF 3D-SIM. And all the above mentioned physical effects, which influence the contrast and inhomogeneity of the illumination pattern, are analyzed by fully vectorial physical-optics modeling of the entire system.

The chapter is organized in the following: In Sec. 6.2, the modeling tasks and techniques are demonstrated. In Sec. 6.3, the modeling results with influences from the polarization, diffraction from an aperture and inclined incidence on the blazed grating in OPEF-2D-SIM case are presented and analyzed. In Sec. 6.4, the modeling results with influences from the misalignment of the system, on the 3D illumination pattern and the temporal focusing in TPEF-3D-SIM case are presented and analyzed. Sec. 6.5 summaries and concludes this chapter.

## 6.2 MODELING TASKS AND TECHNIQUES

In Fig. 60 (a), the schematic for OPEF 2D-SIM is shown. The structured illumination is achieved via interfering two coherent beams in the focal region. The two beams are generated by a grating illuminated by a plane wave. The period of the grating is chosen so that demanded period of the illumination pattern at sample plane can be obtained. Then the diffracted light goes through one lens and the 0th order is blocked at the back focal plane by a mask. Then the  $\pm 1$  orders propagate through a second lens and inter-

ferre with each other at the back focal plane of the second lens to form an intermediate image. Then the intermediate image is demagnified by the 4-f setup consists of the tube

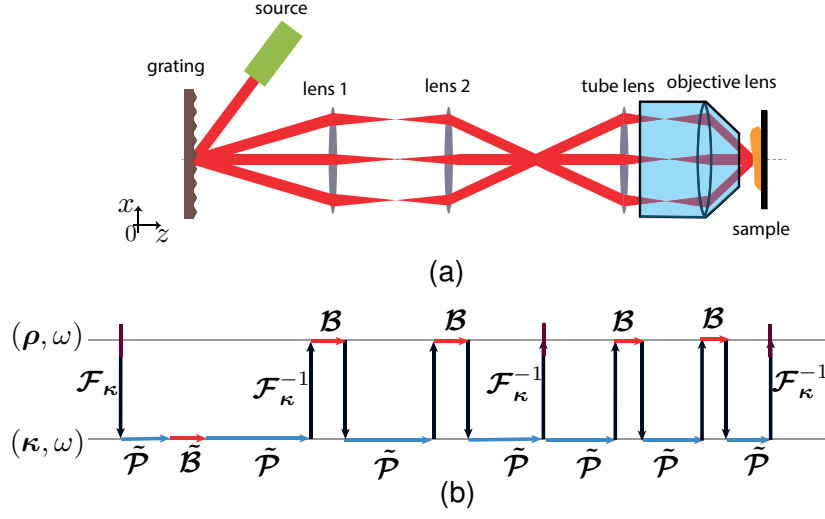


Figure 61: (a). Schematic of the microscopy system with 3D-structured illumination. (b). The corresponding field tracing diagram.

lens and high-NA objective lens to form the illumination pattern at the sample plane. The quality of the illumination pattern, e.g. contrast, inhomogeneity, will be investigated versus polarization, diffraction and the inclined incidence on the blazed grating.

In the case of TPEF 3D-SIM, the 3D-structured illumination and the temporal focusing are investigated separately. The schematic of 3D-structured illumination is shown in Fig. 61 (a). A laser illuminates the grating and three orders are generated. Then they propagate through first, second, tube and objectives lenses. The structured illumination is achieved via interfering the three coherent beams in the focal region. The interference pattern will be investigated when there is a lateral misalignment of the objective lens.

The schematic of the temporal focusing is shown in Fig. 62 (a). A pulsed laser illuminates the gratings, then the +1 diffraction order of the temporal spectrum is separated. Then the separated spectrum propagates through the lens system and is focused at the focal plane. The focused field in time space and the Full Width at Half Maximum (FWHM) of the averaged energy density will be investigated, when a lateral misalignment of the objective lens occurs.

Following the analogous procedure as the example in Sec. 2.1, the field tracing techniques is demonstrated via the field tracing diagrams shown in Fig. 60 (b), Fig. 61 (b) and Fig. 62 (b). The whole modeling procedures are summarized briefly in Tab.5:

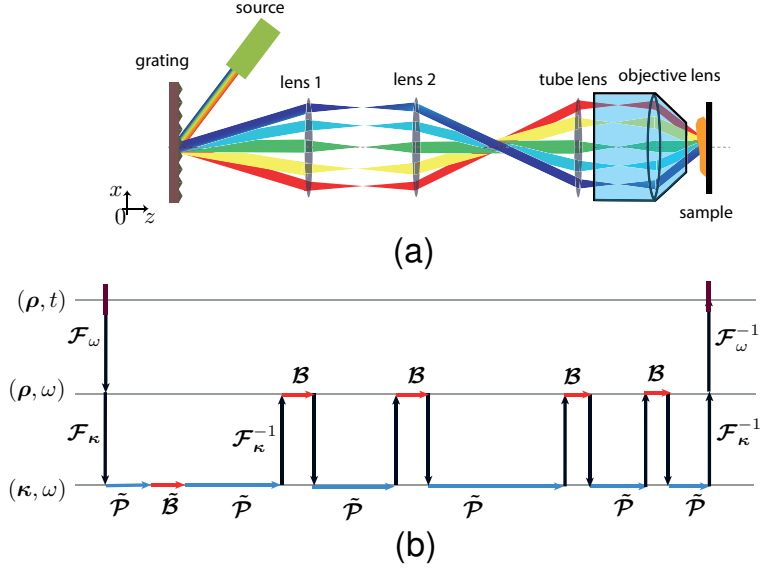


Figure 62: (a). Schematic of the microscopy system with temporal focusing. Collimated pulsed laser is applied to for illumination. (b). The corresponding field tracing diagram.

### 6.3 ONE PHOTON AND TWO DIMENSIONAL

#### 6.3.1 Polarization

The illumination pattern of SIM is highly influenced by the vectorial effects, i.e. polarization, because of the high-NA objective lens. In order to decouple the polarization effect from the inclined illumination on the blazed grating, a transmitting rectangular grating is used with the period  $26.5 \mu\text{m}$  which is invariant in  $y$ -direction with normal incidence as shown in Fig. 63 (a). The diffraction efficiencies of the  $\pm 1$  orders are assumed equal, achieved by an ideal grating. The wavelength of a linearly polarized incident plane wave is  $473 \text{ nm}$  which is a very typical wavelength in OPEF SIM for the excitation. The polarization angle is defined as:  $\alpha = \arctan(\frac{E_y}{E_x})$ . Lens 1 and lens 2 (Thorlab AC254) are double achromatic lenses. Nikon tube lens which has an effective focal lens  $200 \text{ mm}$  is used. The objective lens (Nikon: US patent 6519092B2) is apochromatic with magnification 60X and maximum numerical aperture 1.4 [56]. Its original immersion medium is oil ( $n = 1.515$ ) with a glass coverslip ( $n = 1.522$ ). For the experiment imaging the life cell, water immersion is very often used. Therefore, in the following, the mismatched immersion medium of water ( $n = 1.333$ ) without the coverslip is assumed for the investigation. How the mismatched immersion medium influences the quality of the illumination pattern is under the investigation.

Fig. 63 (b)-(i) shows parts of the structured illumination patterns at the sample plane. They are obtained within several seconds. The inhomogeneities of the whole structured illumination patterns are all below  $\sigma \approx 0.3\%$ . It means that the aberrations of the lens system, even if the mismatched immersion medium is used, nearly have no influence

Table 5: Summary of the applications of field tracing techniques.

		$\mathcal{B}$	$\tilde{\mathcal{B}}$	$\mathcal{F}_\kappa \& \mathcal{F}_\kappa^{-1}$	$\mathcal{F}_\omega \& \mathcal{F}_\omega^{-1}$
OPEF 2D	polarization	real	ideal	HFT&IHFT	no&no
	diffraction	real	ideal	HFT&IHFT but IFFT for the last one	no&no
	inclined incidence	real	real	HFT&IHFT	no&no
TPEF 3D	spatial	ideal lens	ideal	HFT&IHFT	FFT&IFFT
		real lens	real	HFT&IHFT	FFT&IFFT
	temporal	ideal lens	ideal	HFT&IHFT	FFT&IFFT
		real lens	real	HFT&IHFT	FFT&IFFT

on the inhomogeneity.

In the original immersion medium, the contrast of the illumination pattern, labeled in Fig. 63 (b)-(e), decreases significantly as the polarization angle decreases from  $90^\circ$  to  $0^\circ$ . The reason behind is that when the polarization angle decreases, there is an increased longitudinal component  $E_z$ . It has a half-period lateral shift with respect to  $E_x$  and  $E_y$ , thus making the energy density with less contrast. Therefore, it is concluded that  $y$  polarization, which means TE polarization, should be used for the structured illumination in order to have the best contrast. In the real-life experiment, a mask with linear polariser should be applied.

In the case of the mismatched immersion medium, the contrast decreases first and then increases as the polarization angle decreases from  $90^\circ$  to  $0^\circ$ . The reason also comes from the longitudinal component  $E_z$ . When the square of the amplitude of  $E_z$  becomes closest to the summed one of  $E_x$  and  $E_y$ , the contrast has the minimum value.

In order to view the contrast more obviously in the cases of original and mismatched media, the profiles across the  $x$  direction of Fig. 63 (b)-(e) and (f)-(i) are plotted in Fig. 64 (a) and (b) respectively. A scan of the polarization angle is performed with the obtained contrast plotted in Fig. 64 (c). It shows that the contrast decreases more rapidly in the mismatched-immersion-medium case. In other words, the contrast is more sensitive to the polarization in the mismatched-immersion-medium case compared to the original-immersion-medium case. The reason is that the focusing angle is larger in the mismatched-immersion-medium case.

### 6.3.2 Diffraction

In the real-life experiment, there is always an aperture on the grating. Therefore, the diffraction effect from the aperture is also essential for decreasing the quality of the illumination pattern. The modeling of such effect is performed as follows. The aperture of the grating is assumed to be circular with the diameter denoted by  $D^a$ . In this case, TE polarization is used for investigation. The same grating and incident wave param-

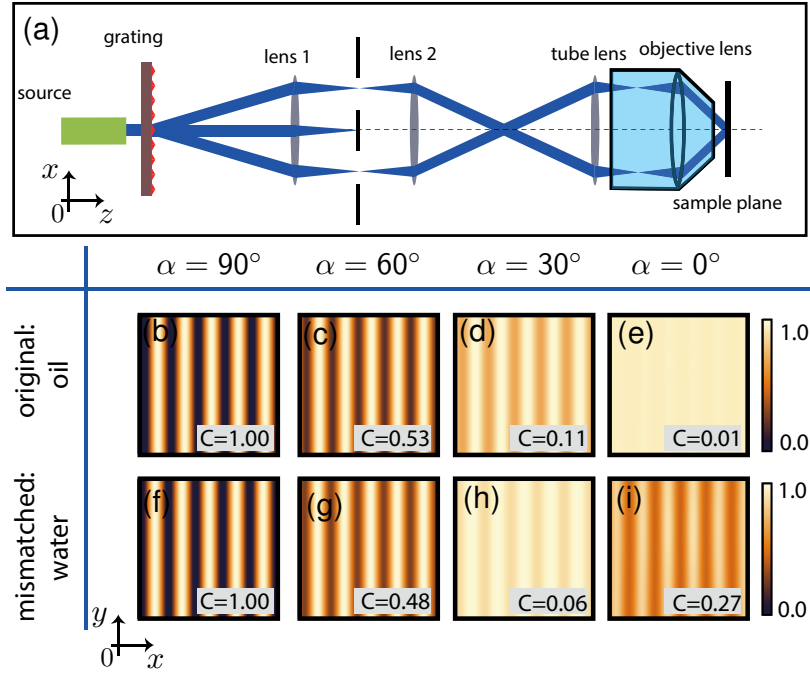


Figure 63: (a). The schematic of the structured illumination microscopy. (b)-(e) show the structured illumination pattern with changing the polarization angle for original immersion medium. (f)-(i) show the structured illumination pattern with changing the polarization angle for mismatched the immersion medium.

eters as previous subsection are used. In order to observe the diffraction effect clearly, the energy density of  $+1$  order at the sample plane is shown in Fig. 65 (a)-(d). When the diameter decreases to  $D^a = 3$  mm, strong diffraction pattern appears which is an important reason for strong inhomogeneity of the illumination pattern. Please note that the size scaling is not the same for different diameters.

The structured illumination pattern with the inhomogeneity obtained by the interference of  $\pm 1$  orders as shown in Fig. 65 (e)-(f). The subsets in the figures show the inhomogeneity visually, which are of  $\sigma = 8\%$ ,  $15\%$ ,  $21\%$ ,  $37\%$ . Therefore, it is concluded that, the diameter of the aperture should be larger than 4 mm if the inhomogeneity of  $\sigma < 0.2$  is desired.

### 6.3.3 Inclined incidence

In real-life experiment, DMD is often used because it is programmable and the switching between different grating patterns is fast and easy to control. Here, it is modeled by a blazed grating made of silver, which has a blazed angle  $12^\circ$  and a period of  $26.5 \mu\text{m}$ . In the usual setup, the blazed grating is perpendicular to the optical axis of the lens system, as indicated in Fig. 66 (a) with  $\theta_3 = 0^\circ$ . And the incident angle is  $\theta_1 = 24^\circ$ . In order to analyze the influence of the inclined incidence on the DMD, the incident angle is scanned from  $\theta = 22^\circ$  to  $\theta = 27^\circ$ . The diffraction efficiency and diffraction angle  $\theta_2$

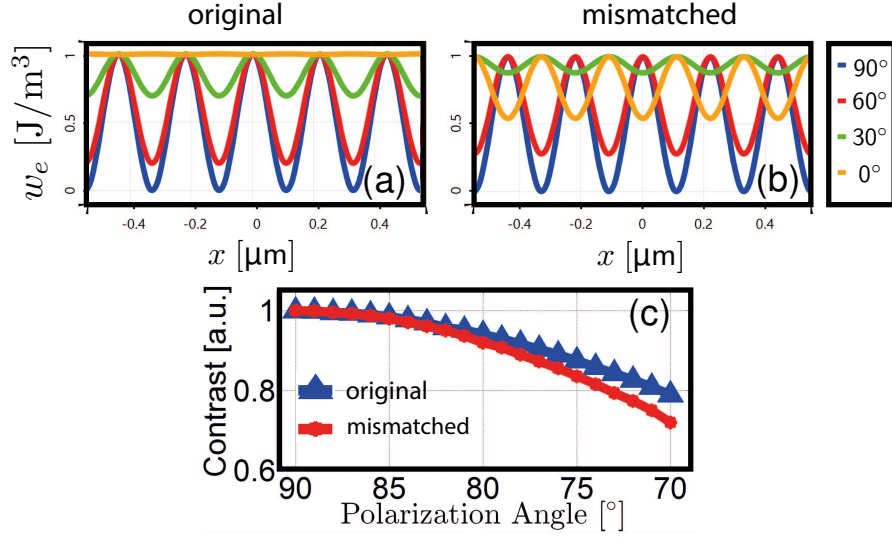


Figure 64: (a) shows the extracted profiles from (b)-(e) in Fig. 63. (b) shows the extracted profiles from (f)-(i) in Fig. 63. (c) plots the contrast vs. polarization angle for original and mismatched media.

are plotted in Fig. 66 (b) and (c). It is shown that when the incident angle is  $24^\circ$ , the diffraction angle of the  $\pm 1$  orders are symmetric about the optical axis as indicated by the first arrow in Fig. 66 (c). But unfortunately, the diffraction efficiencies of the  $\pm 1$  orders are different as indicated by the first arrow in Fig. 66 (b). It makes the interference at the sample plane by two orders with different energies. Therefore, the contrast is influenced by the asymmetric distribution of the energies of the two orders.

In order to compensate the asymmetry of the diffraction efficiencies of the two orders, a larger incident angle should be used as indicated by the second arrow in Fig. 66 (b). In this way, the diffraction angles becomes asymmetric as indicated by the second arrow in Fig. 66 (c). In order to compensate the asymmetry of the diffraction angles, the grating should be tilted by  $\theta_3 \approx 1^\circ$ . From Fig. 66 (b) and (c), it is known that the diffraction efficiency and angles are very sensitive to the incident angle. It should be carefully handled in the experiment.

Finally, the contrast of the illumination pattern is calculated to be  $c = 1.0$  improved from the original one  $c = 0.90$  by around 10%.

## 6.4 TWO PHOTON AND THREE DIMENSIONAL

### 6.4.1 Spatial distribution

The 3D-structured illumination pattern requires the interference of three diffraction orders. Therefore, the quality of the illumination pattern is more sensitive to the misalignment of the lens system compared to the 2D case. A plane wave, polarized in  $y$  direction, with the wavelength of 780nm, illuminates an ideal grating with period of



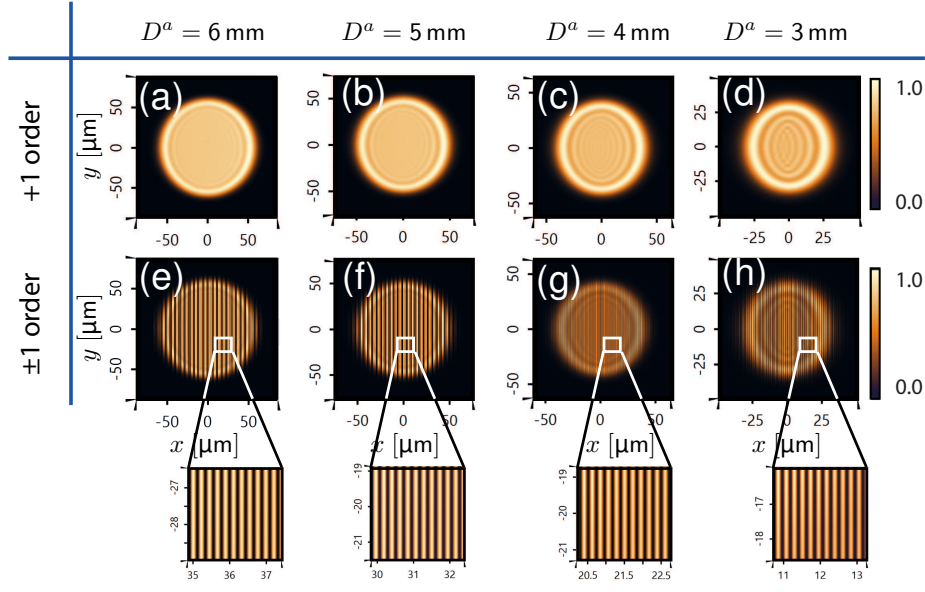


Figure 65: (a)-(d) show the diffraction effects from the apertures: 6 mm, 5 mm, 4 mm and 3 mm for only +1 diffraction order. (e)-(h) show the corresponding results to (a)-(d) for  $\pm 1$  order interference pattern. The subsets indicate the inhomogeneity.

42  $\mu\text{m}$  with equal diffraction efficiencies for all the three orders. Firstly, the illumination pattern is calculated as a reference shown in Fig. 67 (a), by assuming the ideal lens system ( $\text{NA}=1.2$ , water immersion, 60X). The inhomogeneities of the illumination pattern at different planes in the sample region are  $\sigma = 0\%$  as expected. Secondly, the real lenses are used instead of the ideal one. The lens 1,2 and tube lens are from Thorlab (AC254-200-B). The objective lens is water immersion from Nikon (US Patent: 7889433B2). The 3D-structured illumination patterns are shown in Fig. 67 (b). By comparing with the ideal case, the inhomogeneities of the illumination pattern at different planes in the sample region are also around  $\sigma = 0\%$ . It means the real lens system does not influence the quality of the 3D-structured illumination pattern in the term of inhomogeneity, when it is perfectly aligned. Unfortunately, it is not always true in the real-life experiment where the lateral misalignment of the objective lens appears very often. Therefore, the distorted 3D-structured illumination patterns are obtained with a misalignment of the objective lens of 450  $\mu\text{m}$  shown in Fig. 67 (c). The inhomogeneities of the illumination pattern with the lateral size 40  $\mu\text{m}$  are calculated, when the lateral misalignment of the objective lens occurs, to show its tolerance in Fig. 67 (d).

#### 6.4.2 Temporal distribution

The two-photon 3D SIM applies a pulsed laser for the illumination in order to have a temporal focusing. Therefore, the question raises that whether the real lens system has an influence of the pulsed laser on the temporal focusing. To address this issue, a pulsed laser polarized in  $y$  direction, with the center wavelength of 780 nm with 100 fs

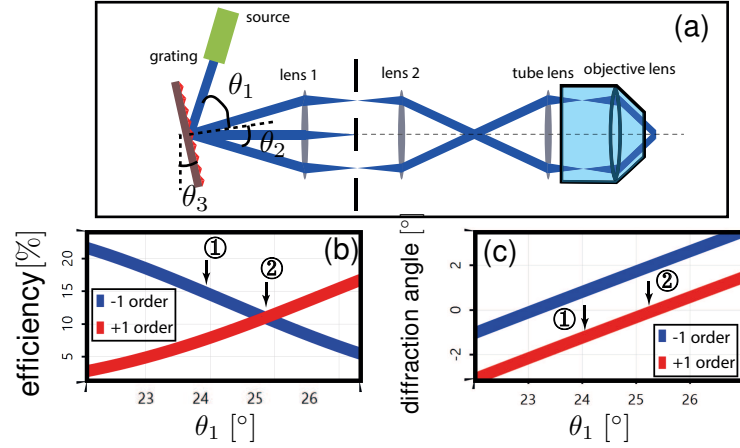


Figure 66: (a). The schematic to show the tilt of the grating. (b) shows the diffraction efficiencies of the  $\pm 1$  orders.

as temporal width, is used as incident wave. The lens and grating are the same as the

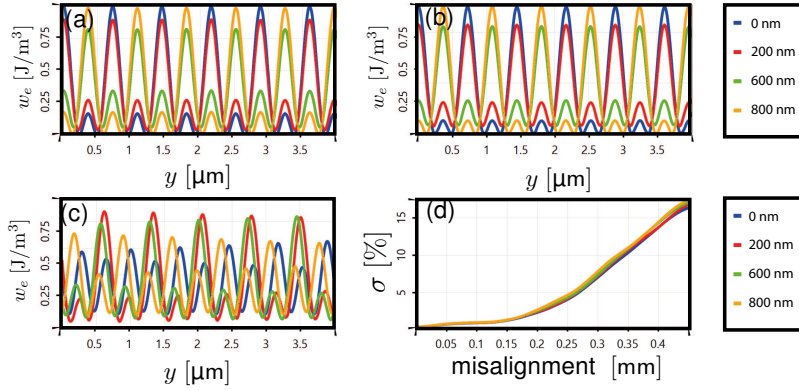


Figure 67: (a). The interference pattern assuming an ideal system. (b). The interference pattern by the real lens with perfect alignment. (c). The interference pattern by the real lens with lateral misalignment of the objective lens of  $450 \mu\text{m}$ . (d) shows the increasing of the inhomogeneity when the lateral misalignment of the objective lens increases. Note that different colors represent different defocused distance.

ones used in the previous subsection.

First, the amplitude of the  $y$  component of the electric field, at the center of the lateral position, is calculated in space-time domain as shown in Fig. 68 (a) by assuming a ideal lens system. The temporal focusing is clearly shown. The corresponding time averaged energy density is shown in Fig. 68 (d) from which the FWHM is calculated as  $\sim 4.5 \mu\text{m}$ . For comparison, the counterpart obtained by using the real lens system is shown in Fig. 68 (b). The corresponding time averaged energy density is shown in Fig. 68 (e). The FWHM is calculated as  $\sim 5.4 \mu\text{m}$ . It is slightly enlarged. It means that in real-life experiment the out-of-focus-noise elimination is around  $\sim 5.4 \mu\text{m}$ , which is

larger than the theoretical prediction by assuming the ideal lens. The reason comes from the fact that more energy is lost when the focusing angel is larger because of Fresnel effects of the curved surfaces of the real lenses. When the objective lens has a lateral misalignment, e.g. 1.5 mm, the amplitude of the electric field as well as the corresponding time-averaged energy density is distorted. It results an even larger FWHM which is around  $\sim 7.5 \mu\text{m}$ . The tolerance on the FWHM based on the lateral misalignment of the objective lens is investigated. The result indicates the increase of the FWHM as the increase of the misalignment shown in Fig. 68 (g).

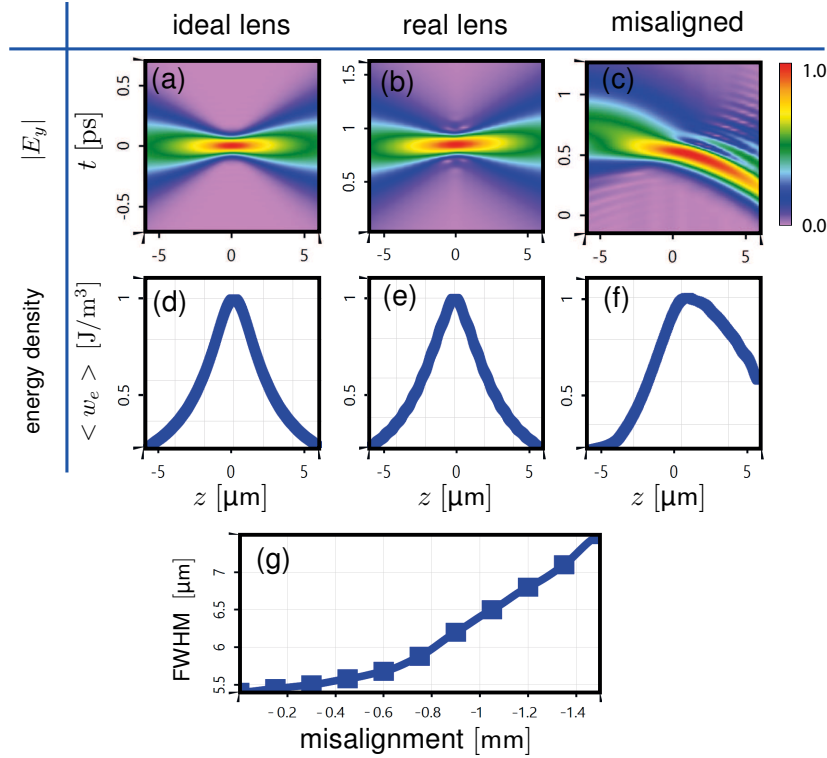


Figure 68: (a-c). The field in the focal region at the center point by ideal lens, real lens with perfect alignment and real lens with lateral misalignment of the objective lens of 1.5 mm respectively. (d-f). The corresponding intensity to Fig.68 (a-c). (g) shows the FWHM increases as the lateral misalignment of the objective lens increases.

## 6.5 SUMMARY AND CONCLUSION

The complexity of microscopy system with structured illumination makes it vulnerable to the undesired effects, which cause low contrast and high inhomogeneity of the illumination pattern. The FWHM of the temporal focusing is also easily influenced by the complex system. These effects should be analyzed and taken into account in the image reconstruction algorithm. In case of deep tissue imaging with the two-photon 3D illumination pattern, adaptive optics can be applied further to compensate the undesired effects.

## CONCLUSION AND OUTLOOK

---

From the introduction to the modeling techniques in the framework of field tracing and then to the numerical results of the different applications, it is concluded that the efficient vectorial physical-optics modeling of an entire optical microscopy system is achieved by connecting different solvers of Maxwell's equations. The solvers for both real and ideal lenses are formulated and unified as the local boundary solvers. The connection of the idealized aplanatic lens with the well-known Debye-Wolf integral is established. After careful investigation of the solvers for the lens system and the micro-/nano-structure, the modeling of different microscopy systems in material science and life science is performed. The modeling technique as a whole is very essential to analyze the physical effects of the entire microscopy system, e.g., the samples and the lenses. It is important to predict the difference between the real and ideal cases when there are imperfections of the entire system, in order to guide the real-life experiment.

The modeling techniques in the framework of field tracing is straightforward to be interpreted and implemented. They are versatile and applicable to model nearly all the optical systems, to which the vectorial physical optics is important, e.g. the augmented reality devices which include the subwavelength gratings, hybrid systems which include both diffractive optical elements or metasurfaces and lens system, interferometers which include micro-/nano-structured samples, etc.

The modeling techniques are the base for the parametric optimization which designs optical systems. Combining with the emerging artificial intelligence technique, it has a huge potential for designing complex and advanced optical system, such as super-resolution microscopes, augmented reality devices, dots projection systems, ultra-thin hybrid imaging lens system, etc.



## APPENDIX: FRESNEL COEFFICIENTS DERIVATION

---

The derivation is directly started from the curl equations of Maxwell's equations of non-magnetic, isotropic and homogeneous medium in spatial frequency domain. And the time harmonic fields are assumed.

$$\nabla \times \mathbf{E}(\mathbf{r}) = i\omega\mu_0\mathbf{H}(\mathbf{r}), \quad (.1a)$$

$$\nabla \times \mathbf{H}(\mathbf{r}) = -i\omega\epsilon\mathbf{E}(\mathbf{r}), \quad (.1b)$$

where  $\epsilon = \epsilon_0\epsilon_r$  is the permittivity of the structure.  $\epsilon_0$  is the permittivity in vacuum.  $\epsilon_r$  is the relative permittivity.

Following the analogous procedure as shown in chapter 2, section 2.3.2 as assuming the electromagnetic field and the structure to be 2D, e.g.  $y$ -invariant. The Transverse Magnetic (TM) and Transverse Electric (TE) cases are obtained as:

$$\frac{\partial E_x(x, z)}{\partial z} - \frac{\partial E_z(x, z)}{\partial x} = i\omega\mu_0 H_y(x, z), \quad (.2a)$$

$$-\frac{\partial H_y(x, z)}{\partial z} = -i\omega\epsilon_0\epsilon_r E_x(x, z), \quad (.2b)$$

$$\frac{\partial H_y(x, z)}{\partial x} = -i\omega\epsilon_0\epsilon_r E_z(x, z), \quad (.2c)$$

and

$$-\frac{\partial E_y(x, z)}{\partial z} = i\omega\mu_0 H_x(x, z), \quad (.3a)$$

$$\frac{\partial E_y(x, z)}{\partial x} = i\omega\mu_0 H_z(x, z), \quad (.3b)$$

$$\frac{\partial H_x(x, z)}{\partial z} - \frac{\partial H_z(x, z)}{\partial x} = -i\omega\epsilon_0\epsilon_r E_y(x, z). \quad (.3c)$$

The above equations are analogous to Eq. 2.74 and Eq. 2.75 in chapter 2. They are called TM case and TE case respectively.

### TE CASE

The TE case is taken for example for further derivation. Substituting  $\omega = \frac{k_0}{\sqrt{\epsilon_0\mu_0}}$  and eliminating  $H_z(x, z)$ , the following equation is obtained from Eq. 3 as:

$$H_x(x, z) = -\frac{i}{k_0} \sqrt{\frac{\epsilon_0}{\mu_0}} \frac{\partial E_y(x, z)}{\partial z}, \quad (.4a)$$

$$\frac{\partial H_x(x, z)}{\partial z} - \frac{i}{k_0} \sqrt{\frac{\epsilon_0}{\mu_0}} \frac{\partial^2 E_y(x, z)}{\partial^2 x} = -\frac{i}{k_0} \sqrt{\frac{\epsilon_0}{\mu_0}} \epsilon_r E_y(x, z). \quad (.4b)$$

Furthermore, by eliminating  $H_x(x, z)$ , the following equation is obtained:

$$\frac{\partial^2 E_y(x, z)}{\partial^2 z} + \frac{\partial^2 E_y(x, z)}{\partial^2 x} + k_0^2 \epsilon_r E_y(x, z) = 0. \quad (.5)$$

It is the wave equation in TE case. The following Ansatz is used as the general solution:

$$E_y(x, z) = A \exp(-i(k_x x + k_z z)), \quad (.6)$$

where  $k_x$  and  $k_z$  are the  $x$  and  $z$  components of the wavevector. Therefore, the incident, reflected and transmitted electric fields are:

$$E_y^{\text{in}}(x, z) = \exp(-i(k_x x + k_{z,I} z)), \quad (.7a)$$

$$E_y^r(x, z) = r_{\text{TE}} \exp(-i(k_x x - k_{z,I} z)), \quad (.7b)$$

$$E_y^t(x, z) = t_{\text{TE}} \exp(-i(k_x x + k_{z,II} z)), \quad (.7c)$$

where  $r_{\text{TE}}$  and  $t_{\text{TE}}$  are the Fresnel coefficients of the reflected and transmitted fields respectively.  $k_{z,I}$  and  $k_{z,II}$  are the  $z$  components of the wavevector in incident and transmitted regions respectively.

By .4a, the incident, reflected and transmitted magnetic fields are obtained as:

$$H_x^{\text{in}}(x, z) = -\frac{i}{k_0} \sqrt{\frac{\epsilon_0}{\mu_0}} (-ik_{z,I}) \exp(-i(k_x x + k_{z,I} z)), \quad (.8a)$$

$$H_x^r(x, z) = -\frac{i}{k_0} \sqrt{\frac{\epsilon_0}{\mu_0}} (ik_{z,I}) r_{\text{TE}} \exp(-i(k_x x - k_{z,I} z)), \quad (.8b)$$

$$H_x^t(x, z) = -\frac{i}{k_0} \sqrt{\frac{\epsilon_0}{\mu_0}} (-ik_{z,II}) t_{\text{TE}} \exp(-i(k_x x + k_{z,II} z)). \quad (.8c)$$

From the boundary condition which states that the transverse components of the electromagnetic field is continuous, the following equations are obtained:

$$E_y^{\text{in}} + E_y^r = E_y^t, \quad (.9a)$$

$$H_x^{\text{in}} + H_x^r = H_x^t. \quad (.9b)$$

By further derivation, the Fresnel coefficients for the TE case are obtained as:

$$r_{\text{TE}} = \frac{-k_{z,II} + k_{z,I}}{k_{z,II} + k_{z,I}}, \quad (.10a)$$

$$t_{\text{TE}} = \frac{2k_{z,I}}{k_{z,II} + k_{z,I}}. \quad (.10b)$$

Since there is only  $y$  component of the electric field, the Fresnel coefficients are directly written:

$$r_{E_y} = r_{\text{TE}} = \frac{-k_{z,II} + k_{z,I}}{k_{z,II} + k_{z,I}}, \quad (.11a)$$

$$t_{E_y} = t_{\text{TE}} = \frac{2k_{z,I}}{k_{z,II} + k_{z,I}}, \quad (.11b)$$

where  $r_{E_y}$  and  $t_{E_y}$  denote the Fresnel coefficients of the  $y$  components of the reflected and transmitted electric fields respectively.

## TM CASE

Following the analogous procedure to the TE case, the wave equation in TM case is obtained as:

$$\frac{\partial^2 H_y(x, z)}{\partial^2 z} + \frac{\partial^2 H_y(x, z)}{\partial^2 x} + k_0^2 \epsilon_r H_y(x, z) = 0. \quad (.12)$$

The same form of Ansatz equation is used as the general solution:

$$H_y(x, z) = A \exp(-i(k_x x + k_z z)). \quad (.13)$$

Analogously to the TE case, the incident, reflected and transmitted magnetic field are:

$$H_y^{\text{in}}(x, z) = \exp(-i(k_x x + k_{z,I} z)), \quad (.14a)$$

$$H_y^r(x, z) = r_{\text{TM}} \exp(-i(k_x x - k_{z,I} z)), \quad (.14b)$$

$$H_y^t(x, z) = t_{\text{TM}} \exp(-i(k_x x + k_{z,II} z)). \quad (.14c)$$

By .2b, the  $x$  component of the electric field is obtained as:

$$E_x^{\text{in}}(x, z) = -\frac{i}{k_0 \epsilon_I} \sqrt{\frac{\mu_0}{\epsilon_0}} (-ik_{z,I}) \exp(-i(k_x x + k_{z,I} z)), \quad (.15a)$$

$$E_x^r(x, z) = -\frac{i}{k_0 \epsilon_I} \sqrt{\frac{\epsilon_0}{\mu_0}} (ik_{z,I}) r_{\text{TM}} \exp(-i(k_x x - k_{z,I} z)), \quad (.15b)$$

$$E_x^t(x, z) = -\frac{i}{k_0 \epsilon_{II}} \sqrt{\frac{\epsilon_0}{\mu_0}} (-ik_{z,II}) t_{\text{TM}} \exp(-i(k_x x + k_{z,II} z)). \quad (.15c)$$

The boundary condition states that the transverse components of the electromagnetic field are continuous:

$$H_y^{\text{in}} + H_y^r = H_y^t, \quad (.16a)$$

$$E_x^{\text{in}} + E_x^r = E_x^t. \quad (.16b)$$

By further derivation, the Fresnel coefficients for the magnetic field equation is obtained:

$$r_{\text{TM}} = \frac{-\frac{k_{z,II}}{\epsilon_{II}} + \frac{k_{z,I}}{\epsilon_I}}{\frac{k_{z,II}}{\epsilon_{II}} + \frac{k_{z,I}}{\epsilon_I}} \quad (.17a)$$

$$t_{\text{TM}} = \frac{\frac{2k_{z,I}}{\epsilon_I}}{\frac{k_{z,II}}{\epsilon_{II}} + \frac{k_{z,I}}{\epsilon_I}}. \quad (.17b)$$

Then, from Eq. .2b, the Fresnel coefficients of the  $x$  components are obtained as:

$$r_{E_x} = -r_{\text{TM}} = \frac{\frac{k_{z,II}}{\epsilon_{II}} - \frac{k_{z,I}}{\epsilon_I}}{\frac{k_{z,II}}{\epsilon_{II}} + \frac{k_{z,I}}{\epsilon_I}} = \frac{\epsilon_I k_{z,II} - \epsilon_{II} k_{z,I}}{\epsilon_I k_{z,II} + \epsilon_{II} k_{z,I}} \quad (.18a)$$

$$t_{E_x} = \frac{k_{z,II}}{\epsilon_{II}} / \frac{k_{z,I}}{\epsilon_I} t_{\text{TM}} = \frac{\frac{2k_{z,II}}{\epsilon_{II}}}{\frac{k_{z,II}}{\epsilon_{II}} + \frac{k_{z,I}}{\epsilon_I}} = \frac{2\epsilon_I k_{z,II}}{\epsilon_I k_{z,II} + \epsilon_{II} k_{z,I}}, \quad (.18b)$$

where  $r_{E_x}$  and  $t_{E_x}$  denote the Fresnel coefficients for the  $x$  components of the reflected and transmitted electric field respectively.





## BIBLIOGRAPHY

---

- [1] D Brocksch. "In memory of Ernst Abbe." In: *Innovation, The Magazine from Carl Zeiss* 15 (2005), pp. 3–23.
- [2] Mohamadreza G. Banaee, M. Selim nl, and Bennett B. Goldberg. "Sub-lambda/10 spot size in semiconductor solid immersion lens microscopy." In: *Optics Communications* 315 (2014), pp. 108 –111. ISSN: 0030-4018. DOI: <https://doi.org/10.1016/j.optcom.2013.11.005>. URL: <http://www.sciencedirect.com/science/article/pii/S0030401813010420>.
- [3] HH Hopkins and PM Barham. "The influence of the condenser on microscopic resolution." In: *Proceedings of the Physical Society. Section B* 63.10 (1950), p. 737.
- [4] Tony Wilson et al. *Confocal microscopy*. Vol. 426. Academic press London, 1990.
- [5] Gordon S Kino and Timothy R Corle. *Confocal scanning optical microscopy and related imaging systems*. Academic Press, 1996.
- [6] James B Pawley. "Fundamental limits in confocal microscopy." In: *Handbook of biological confocal microscopy*. Springer, 2006, pp. 20–42.
- [7] R. Dorn, S. Quabis, and G. Leuchs. "Sharper Focus for a Radially Polarized Light Beam." In: *Phys. Rev. Lett.* 91 (23 2003), p. 233901. DOI: [10.1103/PhysRevLett.91.233901](https://doi.org/10.1103/PhysRevLett.91.233901). URL: <https://link.aps.org/doi/10.1103/PhysRevLett.91.233901>.
- [8] Peiwen Meng, Sylvania Pereira, and Paul Urbach. "Confocal microscopy with a radially polarized focused beam." In: *Opt. Express* 26.23 (2018), pp. 29600–29613. DOI: [10.1364/OE.26.029600](https://doi.org/10.1364/OE.26.029600). URL: <http://www.opticsexpress.org/abstract.cfm?URI=oe-26-23-29600>.
- [9] Qiwen Zhan. "Cylindrical vector beams: from mathematical concepts to applications." In: *Adv. Opt. Photon.* 1.1 (2009), pp. 1–57. DOI: [10.1364/AOP.1.000001](https://doi.org/10.1364/AOP.1.000001). URL: <http://aop.osa.org/abstract.cfm?URI=aop-1-1-1>.
- [10] Mengxue Wu, Rui Chen, Jinzhong Ling, Zaichun Chen, Xudong Chen, Rong Ji, and Minghui Hong. "Creation of a longitudinally polarized photonic nanojet via an engineered microsphere." In: *Opt. Lett.* 42.7 (2017), pp. 1444–1447. DOI: [10.1364/OL.42.001444](https://doi.org/10.1364/OL.42.001444). URL: <http://ol.osa.org/abstract.cfm?URI=ol-42-7-1444>.
- [11] Hui Yang, Rapha?l Trouillon, Gergely Huszka, and Martin A. M. Gijs. "Super-Resolution Imaging of a Dielectric Microsphere Is Governed by the Waist of Its Photonic Nanojet." In: *Nano Letters* 16.8 (2016). PMID: 27398718, pp. 4862–4870. DOI: [10.1021/acs.nanolett.6b01255](https://doi.org/10.1021/acs.nanolett.6b01255). eprint: <http://dx.doi.org/10.1021/acs.nanolett.6b01255>. URL: <http://dx.doi.org/10.1021/acs.nanolett.6b01255>.

- [12] Zengbo Wang, Wei Guo, Lin Li, Boris Luk'yanchuk, Ashfaq Khan, Zhu Liu, Zaichun Chen, and Minghui Hong. "Optical virtual imaging at 50 nm lateral resolution with a white-light nanoscope." In: *Nature Communications* 2 (Mar. 2011), pp. 218–. URL: <http://dx.doi.org/10.1038/ncomms1211>.
- [13] Seoungjun Lee, Lin Li, Yacob Ben-Aryeh, Zengbo Wang, and Wei Guo. "Overcoming the diffraction limit induced by microsphere optical nanoscopy." In: *Journal of Optics* 15.12 (2013), p. 125710. URL: <http://stacks.iop.org/2040-8986/15/i=12/a=125710>.
- [14] Haie Zhu, Bing Yan, Shuxue Zhou, Zengbo Wang, and Limin Wu. "Synthesis and super-resolution imaging performance of a refractive-index-controllable microsphere superlens." In: *J. Mater. Chem. C* 3 (41 2015), pp. 10907–10915. DOI: [10.1039/C5TC02310F](https://doi.org/10.1039/C5TC02310F). URL: <http://dx.doi.org/10.1039/C5TC02310F>.
- [15] Darshan B. Desai, Daniel Dominguez, Ayrton A. Bernussi, and Luis Grave de Peralta. "Ultra-thin condensers for optical subwavelength resolution microscopy." In: *Journal of Applied Physics* 115.9 (2014), p. 093103. DOI: [10.1063/1.4867295](https://doi.org/10.1063/1.4867295). eprint: <https://doi.org/10.1063/1.4867295>. URL: <https://doi.org/10.1063/1.4867295>.
- [16] Eric Betzig, A Lewis, A Harootunian, M Isaacson, and E Kratschmer. "Near field scanning optical microscopy (NSOM): development and biophysical applications." In: *Biophysical journal* 49.1 (1986), pp. 269–279.
- [17] A Harootunian, E Betzig, M Isaacson, and A Lewis. "Super-resolution fluorescence near-field scanning optical microscopy." In: *Applied Physics Letters* 49.11 (1986), pp. 674–676.
- [18] Peter Török and Fu-Jen Kao. *Optical imaging and microscopy: techniques and advanced systems*. Vol. 87. Springer, 2007.
- [19] Frits Zernike. "How I discovered phase contrast." In: *Science* 121.3141 (1955), pp. 345–349.
- [20] Frits Zernike. "Phase contrast, a new method for the microscopic observation of transparent objects." In: *Physica* 9.7 (1942), pp. 686–698.
- [21] Nomarski Georges. *Interferential polarizing device for study of phase objects*. US Patent 2,924,142. 1960.
- [22] Moritz Esslinger and Herbert Gross. "Simulation of differential interference contrast microscopy and influence of aberrations." In: *Journal of Microscopy* 259.1 (2015), pp. 59–65.
- [23] Timo Mappes, Norbert Jahr, Andrea Csaki, Nadine Vogler, Juergen Popp, and Wolfgang Fritzsche. "The invention of immersion ultramicroscopy in 1912 the birth of nanotechnology?" In: *Angewandte Chemie International Edition* 51.45 (2012), pp. 11208–11212.
- [24] M. A. Lieb, J. M. Zavislan, and L. Novotny. "Single-Molecule Orientations Determined by Direct Emission Pattern Imaging." In: *J. Opt. Soc. Am. B* 21 (2004), p. 1210.

- [25] K. G. Lee, X. W. Chen, H. Eghlidi, P. Kukura, R. Lettow, A. Renn, V. Sandogh-dar, and S. G?tzinger. "A planar dielectric antenna for directional single-photon emission and near-unity collection efficiency." In: *Nature Photonics* 5 (Jan. 2011), pp. 166–. URL: <http://dx.doi.org/10.1038/nphoton.2010.312>.
- [26] Rebecca Wagner, Lars Heerklotz, Nikolai Kortenbruck, and Frank Cichos. "Back focal plane imaging spectroscopy of photonic crystals." In: *Applied Physics Letters* 101.8 (2012), p. 081904. DOI: [10.1063/1.4746251](https://doi.org/10.1063/1.4746251). eprint: <https://doi.org/10.1063/1.4746251>. URL: <https://doi.org/10.1063/1.4746251>.
- [27] Jürgen Jahns and Sing H Lee. *Optical Computing Hardware: Optical Computing*. Academic press, 1994.
- [28] Jürgen Jahns, Karl-Heinz Brenner, et al. *Microoptics: from technology to applications*. Springer Science & Business Media, 2004.
- [29] Stefan Sinzinger and Jürgen Jahns. *Microoptics*. John Wiley & Sons, 2006.
- [30] Jürgen Jahns and Stefan Helfert. *Introduction to micro-and nanooptics*. John Wiley & Sons, 2012.
- [31] M Blattmann, S Kretschmer, S Thiele, C Ataman, H Zappe, A Herkommer, and A Seifert. "Bimodal endoscopic probe combining white-light microscopy and optical coherence tomography." In: *Applied optics* 55.15 (2016), pp. 4261–4269.
- [32] Sarah Fischbach, Alexander Schlehahn, Alexander Thoma, Nicole Srocka, Timo Gissibl, Simon Ristok, Simon Thiele, Arsenty Kaganskiy, Andre Strittmatter, Tobias Heindel, et al. "Single quantum dot with microlens and 3D-printed micro-objective as integrated bright single-photon source." In: *ACS photonics* 4.6 (2017), pp. 1327–1332.
- [33] Partha Pratim Mondal and Alberto Diaspro. *Fundamentals of fluorescence microscopy: exploring life with light*. Springer Science & Business Media, 2013.
- [34] Guoan Zheng, Roarke Horstmeyer, and Changhuei Yang. "Wide-field, high-resolution Fourier ptychographic microscopy." In: *Nature photonics* 7.9 (2013), p. 739.
- [35] Daniel Dominguez, Nouf Alharbi, Mdhaoui Alhusain, Ayrton A Bernussi, and Luis Grave de Peralta. "Fourier plane imaging microscopy." In: *Journal of Applied Physics* 116, 103102 (2014).
- [36] Jeff W Lichtman and Jos-Angel Conchello. "Fluorescence microscopy." In: *Nature Methods* 2 (Nov. 2005), pp. 910–. URL: <http://dx.doi.org/10.1038/nmeth817>.
- [37] Xiang Lu, Olga Rodenko, Yueqian Zhang, and Herbert Gross. "Efficient simulation of autofluorescence effects in microscope lenses." In: *Applied optics* 58.13 (2019), pp. 3589–3596.
- [38] Kai Wicker and Rainer Heintzmann. "Resolving a misconception about structured illumination." In: *Nature Photonics* 8 (Apr. 2014), pp. 342–. URL: <https://doi.org/10.1038/nphoton.2014.88>.

- [39] Stefan W. Hell and Jan Wichmann. "Breaking the diffraction resolution limit by stimulated emission: stimulated-emission-depletion fluorescence microscopy." In: *Opt. Lett.* 19.11 (1994), pp. 780–782. DOI: [10.1364/OL.19.000780](https://doi.org/10.1364/OL.19.000780). URL: <http://ol.osa.org/abstract.cfm?URI=ol-19-11-780>.
- [40] Rainer Heintzmann and Christoph G. Cremer. "Laterally modulated excitation microscopy: improvement of resolution by using a diffraction grating." In: vol. 3568. 1999, pp. 3568–3568–12. DOI: [10.1117/12.336833](https://doi.org/10.1117/12.336833). URL: <https://doi.org/10.1117/12.336833>.
- [41] M. G. L. Gustafsson. "Surpassing the lateral resolution limit by a factor of two using structured illumination microscopy." In: *Journal of Microscopy* (2000).
- [42] Florian Ströhl and Clemens F. Kaminski. "Frontiers in structured illumination microscopy." In: *Optica* 3.6 (2016), pp. 667–677. DOI: [10.1364/OPTICA.3.000667](https://doi.org/10.1364/OPTICA.3.000667). URL: <http://www.osapublishing.org/optica/abstract.cfm?URI=optica-3-6-667>.
- [43] Eric Betzig, George H. Patterson, Rachid Sougrat, O. Wolf Lindwasser, Scott Olenych, Juan S. Bonifacio, Michael W. Davidson, Jennifer Lippincott-Schwartz, and Harald F. Hess. "Imaging Intracellular Fluorescent Proteins at Nanometer Resolution." In: *Science* 313.5793 (2006), pp. 1642–1645. ISSN: 0036-8075. DOI: [10.1126/science.1127344](https://doi.org/10.1126/science.1127344). eprint: <http://science.sciencemag.org/content/313/5793/1642.full.pdf>. URL: <http://science.sciencemag.org/content/313/5793/1642>.
- [44] Bo Huang, Hazen Babcock, and Xiaowei Zhuang. "Breaking the Diffraction Barrier: Super-Resolution Imaging of Cells." In: *Cell* 143.7 (Dec. 2010), pp. 1047–1058. ISSN: 0092-8674. DOI: [10.1016/j.cell.2010.12.002](https://doi.org/10.1016/j.cell.2010.12.002). URL: <http://dx.doi.org/10.1016/j.cell.2010.12.002>.
- [45] S. W. Hell, S. Lindek, C. Cremer, and E. H. K. Stelzer. "Measurement of the 4Pi-confocal point spread function proves 75 nm axial resolution." In: *Applied Physics Letters* 64.11 (1994), pp. 1335–1337. DOI: [10.1063/1.111926](https://doi.org/10.1063/1.111926). eprint: <http://dx.doi.org/10.1063/1.111926>. URL: <http://dx.doi.org/10.1063/1.111926>.
- [46] André Junker and Karl-Heinz Brenner. "Two-sided illumination in rigorous coupled-wave analysis applied to the 4pi-microscope." In: *J. Opt. Soc. Am. A* 34.10 (2017), pp. 1769–1775. DOI: [10.1364/JOSAA.34.001769](https://doi.org/10.1364/JOSAA.34.001769). URL: <http://josaa.osa.org/abstract.cfm?URI=josaa-34-10-1769>.
- [47] Uros Krzic, Stefan Gunther, Timothy E Saunders, Sebastian J Streichan, and Lars Hufnagel. "Multiview light-sheet microscope for rapid in toto imaging." In: *Nature methods* 9.7 (2012), p. 730.
- [48] Raju Tomer, Khaled Khairy, Fernando Amat, and Philipp J Keller. "Quantitative high-speed imaging of entire developing embryos with simultaneous multiview light-sheet microscopy." In: *Nature methods* 9.7 (2012), p. 755.
- [49] Philipp J Keller, Annette D Schmidt, Joachim Wittbrodt, and Ernst HK Stelzer. "Reconstruction of zebrafish early embryonic development by scanned light sheet microscopy." In: *science* 322.5904 (2008), pp. 1065–1069.

- [50] Gael Moneron and Stefan W Hell. "Two-photon excitation STED microscopy." In: *Optics express* 17.17 (2009), pp. 14567–14573.
- [51] Peter W. Winter, Andrew G. York, Damian Dalle Nogare, Maria Ingaramo, Ryan Christensen, Ajay Chitnis, George H. Patterson, and Hari Shroff. "Two-photon instant structured illumination microscopy improves the depth penetration of super-resolution imaging in thick scattering samples." In: *Optica* 1.3 (2014), pp. 181–191. DOI: [10.1364/OPTICA.1.000181](https://doi.org/10.1364/OPTICA.1.000181). URL: <http://www.osapublishing.org/optica/abstract.cfm?URI=optica-1-3-181>.
- [52] W Denk, JH Strickler, and WW Webb. "Two-photon laser scanning fluorescence microscopy." In: *Science* 248.4951 (1990), pp. 73–76. ISSN: 0036-8075. DOI: [10.1126/science.2321027](https://doi.org/10.1126/science.2321027). eprint: <http://science.sciencemag.org/content/248/4951/73.full.pdf>. URL: <http://science.sciencemag.org/content/248/4951/73>.
- [53] Lord Rayleigh. "XXXI. Investigations in optics, with special reference to the spectroscope." In: *The London, Edinburgh, and Dublin Philosophical Magazine and Journal of Science* 8.49 (1879), pp. 261–274.
- [54] Robert T Kester, Tomasz S Tkaczyk, Michael R Descour, Todd Christenson, and Rebecca Richards-Kortum. "High numerical aperture microendoscope objective for a fiber confocal reflectance microscope." In: *Optics express* 15.5 (2007), pp. 2409–2420.
- [55] G. Seward. *Optical Design of Microscopes*. SPIE tutorial texts. SPIE Press, 2010. ISBN: 9780819480958. URL: <https://books.google.de/books?id=sid8RAACAAJ>.
- [56] Jonathan A. Kurvits, Mingming Jiang, and Rashid Zia. "Comparative analysis of imaging configurations and objectives for Fourier microscopy." In: *J. Opt. Soc. Am. A* 32.11 (2015), pp. 2082–2092. DOI: [10.1364/JOSAA.32.002082](https://doi.org/10.1364/JOSAA.32.002082). URL: <http://josaa.osa.org/abstract.cfm?URI=josaa-32-11-2082>.
- [57] Yueqian Zhang and Herbert Gross. "Systematic design of microscope objectives. Part I: System review and analysis." In: *Advanced Optical Technologies* 8.5 (2019), pp. 313–347.
- [58] Yueqian Zhang and Herbert Gross. "Systematic design of microscope objectives. Part II: Lens modules and design principles." In: *Advanced Optical Technologies* 8.5 (2019), pp. 349–384.
- [59] Yueqian Zhang and Herbert Gross. "Systematic design of microscope objectives. Part III: miscellaneous design principles and system synthesis: Systematic design of microscope objectives. Part I/II/III." In: *Advanced Optical Technologies* 8.5 (2019), pp. 385–402.
- [60] Zemax. OpticStudio combines complex physics and interactive visuals so you can analyze, simulate, and optimize optics, lighting and illumination systems, and laser systems, all within tolerance specifications. <https://www.zemax.com/>.
- [61] CodeV. CODE V optical design software is a computer aided design software used to model, analyze, optimize, and provide fabrication support for the development of optical systems for diverse application. <https://www.synopsys.com/optical-solutions/codev.html>.

- [62] B. Richards and E. Wolf. "Electromagnetic Diffraction in Optical Systems. II. Structure of the Image Field in an Aplanatic System." In: *Proceedings of the Royal Society of London A: Mathematical, Physical and Engineering Sciences* 253.1274 (1959), pp. 358–379. ISSN: 0080-4630. DOI: [10.1098/rspa.1959.0200](https://doi.org/10.1098/rspa.1959.0200). eprint: <http://rspa.royalsocietypublishing.org/content/253/1274/358.full.pdf>. URL: <http://rspa.royalsocietypublishing.org/content/253/1274/358>.
- [63] E. Wolf. "Electromagnetic Diffraction in Optical Systems. I. An Integral Representation of the Image Field." In: *Proceedings of the Royal Society of London A: Mathematical, Physical and Engineering Sciences* 253.1274 (1959), pp. 349–357. ISSN: 0080-4630. DOI: [10.1098/rspa.1959.0199](https://doi.org/10.1098/rspa.1959.0199). eprint: <http://rspa.royalsocietypublishing.org/content/253/1274/349.full.pdf>. URL: <http://rspa.royalsocietypublishing.org/content/253/1274/349>.
- [64] Jacob.J Stamnes. *Waves in Focal Regions*. Taylor & Francis Group, 1986.
- [65] Lukas Novotny and Bert Hecht. *Principles of Nano-Optics*. Cambridge University Press, 2006. DOI: [10.1017/CB09780511813535](https://doi.org/10.1017/CB09780511813535).
- [66] Matthew R. Foreman and Peter Török. "Computational methods in vectorial imaging." In: *Journal of Modern Optics* 58.5-6 (2011), pp. 339–364. DOI: [10.1080/09500340.2010.525668](https://doi.org/10.1080/09500340.2010.525668). eprint: <http://dx.doi.org/10.1080/09500340.2010.525668>. URL: <http://dx.doi.org/10.1080/09500340.2010.525668>.
- [67] K. S. Youngworth and T. G Brown. "Focusing of high numerical aperture cylindrical-vector beams." In: *Opt. Express* 7.2 (2000), pp. 77–87. DOI: [10.1364/OE.7.000077](https://doi.org/10.1364/OE.7.000077). URL: <http://www.opticsexpress.org/abstract.cfm?URI=oe-7-2-77>.
- [68] Jeongmin Kim, Yuan Wang, and Xiang Zhang. "Calculation of vectorial diffraction in optical systems." In: *J. Opt. Soc. Am. A* 35.4 (2018), pp. 526–535. DOI: [10.1364/JOSAA.35.000526](https://doi.org/10.1364/JOSAA.35.000526). URL: <http://josaa.osa.org/abstract.cfm?URI=josaa-35-4-526>.
- [69] Marcel Leutenegger, Ramachandra Rao, Rainer A. Leitgeb, and Theo Lasser. "Fast focus field calculations." In: *Opt. Express* 14.23 (2006), pp. 11277–11291. DOI: [10.1364/OE.14.011277](https://doi.org/10.1364/OE.14.011277). URL: <http://www.opticsexpress.org/abstract.cfm?URI=oe-14-23-11277>.
- [70] Adam S. Backer and W. E. Moerner. "Extending Single-Molecule Microscopy Using Optical Fourier Processing." In: *The Journal of Physical Chemistry B* 118.28 (2014). PMID: 24745862, pp. 8313–8329. DOI: [10.1021/jp501778z](https://doi.org/10.1021/jp501778z). eprint: <https://doi.org/10.1021/jp501778z>. URL: <https://doi.org/10.1021/jp501778z>.
- [71] P. Török, P. Varga, Z. Laczik, and G. R. Booker. "Electromagnetic diffraction of light focused through a planar interface between materials of mismatched refractive indices: an integral representation." In: *J. Opt. Soc. Am. A* 12.2 (1995), pp. 325–332. DOI: [10.1364/JOSAA.12.000325](https://doi.org/10.1364/JOSAA.12.000325). URL: <http://josaa.osa.org/abstract.cfm?URI=josaa-12-2-325>.
- [72] S.H. Wiersma and T.D. Visser. "Defocusing of a converging electromagnetic wave by a plane dielectric interface." In: *Journal of the Optical Society of America, Part A: Optics and Image Science* 13.2 (1996). DOI: [10.1364/JOSAA.13.000320](https://doi.org/10.1364/JOSAA.13.000320).



- [73] P. Török and P. Varga. “Electromagnetic diffraction of light focused through a stratified medium.” In: *Appl. Opt.* 36.11 (1997), pp. 2305–2312. DOI: [10.1364/AO.36.002305](https://doi.org/10.1364/AO.36.002305). URL: <http://ao.osa.org/abstract.cfm?URI=ao-36-11-2305>.
- [74] Peter Török. “Focusing of electromagnetic waves through a dielectric interface by lenses of finite Fresnel number.” In: *J. Opt. Soc. Am. A* 15.12 (1998), pp. 3009–3015. DOI: [10.1364/JOSAA.15.003009](https://doi.org/10.1364/JOSAA.15.003009). URL: <http://josaa.osa.org/abstract.cfm?URI=josaa-15-12-3009>.
- [75] David P Biss and Thomas G Brown. “Cylindrical vector beam focusing through a dielectric interface.” In: *Optics Express* 9.10 (2001), pp. 490–497.
- [76] Olivier Haeblerlé, Mehdi Ammar, Hiromitsu Furukawa, Koji Tenjimabayashi, and Peter Török. “Point spread function of optical microscopes imaging through stratified media.” In: *Optics Express* 11.22 (2003), pp. 2964–2969.
- [77] Hanming Guo, Songlin Zhuang, Jiabi Chen, and Zhongcheng Liang. “Imaging theory of an aplanatic system with a stratified medium based on the method for a vector coherent transfer function.” In: *Opt. Lett.* 31.20 (2006), pp. 2978–2980. DOI: [10.1364/OL.31.002978](https://doi.org/10.1364/OL.31.002978). URL: <http://ol.osa.org/abstract.cfm?URI=ol-31-20-2978>.
- [78] Ingo Gregor and Jörg Enderlein. “Focusing astigmatic Gaussian beams through optical systems with a high numerical aperture.” In: *Opt. Lett.* 30.19 (2005), pp. 2527–2529. DOI: [10.1364/OL.30.002527](https://doi.org/10.1364/OL.30.002527). URL: <http://ol.osa.org/abstract.cfm?URI=ol-30-19-2527>.
- [79] Rakesh Kumar Singh, P. Senthilkumaran, and Kehar Singh. “Tight focusing of vortex beams in presence of primary astigmatism.” In: *J. Opt. Soc. Am. A* 26.3 (2009), pp. 576–588. DOI: [10.1364/JOSAA.26.000576](https://doi.org/10.1364/JOSAA.26.000576). URL: <http://josaa.osa.org/abstract.cfm?URI=josaa-26-3-576>.
- [80] Joseph Braat and Peter Török. *Imaging optics*. Cambridge University Press, 2019.
- [81] Herbert Gross, Fritz Blechinger, and Bertram Aichtner. *Handbook of optical systems*. Vol. 1. Wiley Online Library, 2005.
- [82] Andreas Tittl, Moshe G. Harats, Ramon Walter, Xinghui Yin, Martin Schaeferling, Na Liu, Ronen Rapaport, and Harald Giessen. “Quantitative Angle-Resolved Small-Spot Reflectance Measurements on Plasmonic Perfect Absorbers: Impedance Matching and Disorder Effects.” In: *ACS Nano* 8.10 (2014). PMID: 25251075, pp. 10885–10892. DOI: [10.1021/nn504708t](https://doi.org/10.1021/nn504708t). eprint: <https://doi.org/10.1021/nn504708t>. URL: <https://doi.org/10.1021/nn504708t>.
- [83] Ran Ye, Yong-Hong Ye, Hui Feng Ma, Lingling Cao, Jun Ma, Frank Wyrowski, Rui Shi, and Jia-Yu Zhang. “Experimental imaging properties of immersion microscale spherical lenses.” In: *Scientific Reports* 4 (Jan. 2014), pp. 3769–. URL: <http://dx.doi.org/10.1038/srep03769>.
- [84] Liyang Yue, Bing Yan, and Zengbo Wang. “Photonic nanojet of cylindrical metalens assembled by hexagonally arranged nanofibers for breaking the diffraction limit.” In: *Opt. Lett.* 41.7 (2016), pp. 1336–1339. DOI: [10.1364/OL.41.001336](https://doi.org/10.1364/OL.41.001336). URL: <http://ol.osa.org/abstract.cfm?URI=ol-41-7-1336>.



- [85] Vijay M. Sundaram and Sy-Bor Wen. "Analysis of deep sub-micron resolution in microsphere based imaging." In: *Applied Physics Letters* 105.20 (2014), p. 204102. DOI: [10.1063/1.4902247](https://doi.org/10.1063/1.4902247). eprint: <http://dx.doi.org/10.1063/1.4902247>. URL: <http://dx.doi.org/10.1063/1.4902247>.
- [86] F. Wyrowski and M. Kuhn. "Introduction to field tracing." In: *Journal of Modern Optics* 58.5-6 (2011), pp. 449–466. DOI: [10.1080/09500340.2010.532237](https://doi.org/10.1080/09500340.2010.532237). eprint: <http://dx.doi.org/10.1080/09500340.2010.532237>. URL: <http://dx.doi.org/10.1080/09500340.2010.532237>.
- [87] Michael Kuhn, Frank Wyrowski, and Christian Hellmann. "Non-sequential Optical Field Tracing." In: *Advanced Finite Element Methods and Applications*. Ed. by Thomas Apel and Olaf Steinbach. Vol. 66. Lecture Notes in Applied and Computational Mechanics. Springer Berlin Heidelberg, 2013, pp. 257–273. ISBN: 978-3-642-30315-9. DOI: [10.1007/978-3-642-30316-6\\_12](https://doi.org/10.1007/978-3-642-30316-6_12). URL: [http://dx.doi.org/10.1007/978-3-642-30316-6\\_12](http://dx.doi.org/10.1007/978-3-642-30316-6_12).
- [88] P. Török, P. D. Higdon, and T. Wilson. "Theory for confocal and conventional microscopes imaging small dielectric scatterers." In: *Journal of Modern Optics* 45.8 (1998), pp. 1681–1698. DOI: [10.1080/09500349808230662](https://doi.org/10.1080/09500349808230662). eprint: <http://dx.doi.org/10.1080/09500349808230662>. URL: <http://dx.doi.org/10.1080/09500349808230662>.
- [89] P. Toeroek, P.D. Higdon, R. Juskaitis, and T. Wilson. "Optimising the image contrast of conventional and confocal optical microscopes imaging finite sized spherical gold scatterers." In: *Optics Communications* 155.4 (1998), pp. 335–341. DOI: [doi:10.1016/S0030-4018\(98\)00384-8](https://doi.org/10.1016/S0030-4018(98)00384-8). URL: <http://www.ingentaconnect.com/content/els/00304018/1998/00000155/00000004/art00384>.
- [90] Ryan L. Coe and Eric J. Seibel. "Computational modeling of optical projection tomographic microscopy using the finite difference time domain method." In: *J. Opt. Soc. Am. A* 29.12 (2012), pp. 2696–2707. DOI: [10.1364/JOSAA.29.002696](https://doi.org/10.1364/JOSAA.29.002696). URL: <http://josaa.osa.org/abstract.cfm?URI=josaa-29-12-2696>.
- [91] Rui Chen, Krishna Agarwal, Yu Zhong, Colin J. R. Sheppard, Jacob C. H. Phang, and Xudong Chen. "Complete modeling of subsurface microscopy system based on aplanatic solid immersion lens." In: *J. Opt. Soc. Am. A* 29.11 (2012), pp. 2350–2359. DOI: [10.1364/JOSAA.29.002350](https://doi.org/10.1364/JOSAA.29.002350). URL: <http://josaa.osa.org/abstract.cfm?URI=josaa-29-11-2350>.
- [92] Rui Chen, Krishna Agarwal, Colin J. R. Sheppard, Jacob C. H. Phang, and Xudong Chen. "A complete and computationally efficient numerical model of aplanatic solid immersion lens scanning microscope." In: *Opt. Express* 21.12 (2013), pp. 14316–14330. DOI: [10.1364/OE.21.014316](https://doi.org/10.1364/OE.21.014316). URL: <http://www.opticsexpress.org/abstract.cfm?URI=oe-21-12-14316>.
- [93] E. Popov. *Gratings: Theory and Numeric Applications*. Ed. by E. Popov. Popov, Institut Fresnel, 2014. ISBN: 9782853998604. URL: <https://books.google.de/books?id=BMnOUX05v94C>.

- [94] Site Zhang, Daniel Asoubar, Christian Hellmann, and Frank Wyrowski. "Propagation of electromagnetic fields between non-parallel planes: a fully vectorial formulation and an efficient implementation." In: *Appl. Opt.* 55.3 (2016), pp. 529–538. DOI: [10.1364/AO.55.000529](https://doi.org/10.1364/AO.55.000529). URL: <http://ao.osa.org/abstract.cfm?URI=ao-55-3-529>.
- [95] Daniel Asoubar, Site Zhang, Frank Wyrowski, and Michael Kuhn. "Parabasal field decomposition and its application to non-paraxial propagation." In: *Opt. Express* 20.21 (2012), pp. 23502–23517. DOI: [10.1364/OE.20.023502](https://doi.org/10.1364/OE.20.023502). URL: <http://www.opticsexpress.org/abstract.cfm?URI=oe-20-21-23502>.
- [96] Albrecht v. Pfeil, Frank Wyrowski, Andreas Drauschke, and Harald Aagedal. "Analysis of Optical Elements with the Local Plane-Interface Approximation." In: *Appl. Opt.* 39.19 (2000), pp. 3304–3313. DOI: [10.1364/AO.39.003304](https://doi.org/10.1364/AO.39.003304). URL: <http://ao.osa.org/abstract.cfm?URI=ao-39-19-3304>.
- [97] Rui Shi, Christian Hellmann, and Frank Wyrowski. "Physical-optics propagation through curved surfaces." In: *J. Opt. Soc. Am. A* 36.7 (2019), pp. 1252–1260. DOI: [10.1364/JOSAA.36.001252](https://doi.org/10.1364/JOSAA.36.001252). URL: <http://josaa.osa.org/abstract.cfm?URI=josaa-36-7-1252>.
- [98] Rui Shi and Frank Wyrowski. "Comparison of aplanatic and real lens focused spots in the framework of the local plane interface approximation." In: *J. Opt. Soc. Am. A* 36.10 (2019), pp. 1801–1809. DOI: [10.1364/JOSAA.36.001801](https://doi.org/10.1364/JOSAA.36.001801). URL: <http://josaa.osa.org/abstract.cfm?URI=josaa-36-10-1801>.
- [99] R. Shi, S. Zhang, C. Hellmann, and F. Wyrowski. "Fast-physical optics modeling of two-photon fluorescence microscopy with 3D-structured illumination." In: *Proc. DGO* (2019).
- [100] Eric Silberstein, Philippe Lalanne, Jean-Paul Hugonin, and Qing Cao. "Use of grating theories in integrated optics." In: *J. Opt. Soc. Am. A* 18.11 (2001), pp. 2865–2875. DOI: [10.1364/JOSAA.18.002865](https://doi.org/10.1364/JOSAA.18.002865). URL: <http://josaa.osa.org/abstract.cfm?URI=josaa-18-11-2865>.
- [101] Olga Baladron-Zorita, Zongzhao Wang, Christian Hellmann, and Frank Wyrowski. "Isolating the Gouy phase shift in a full physical-optics solution to the propagation problem." In: *J. Opt. Soc. Am. A* 36.9 (2019), pp. 1551–1558. DOI: [10.1364/JOSAA.36.001551](https://doi.org/10.1364/JOSAA.36.001551). URL: <http://josaa.osa.org/abstract.cfm?URI=josaa-36-9-1551>.
- [102] Zongzhao Wang, Olga Baladron-Zorita, Christian Hellmann, and Frank Wyrowski. "Theory and algorithm of the homeomorphic Fourier transform for optical simulations." In: *Opt. Express* 28.7 (2020), pp. 10552–10571. DOI: [10.1364/OE.388022](https://doi.org/10.1364/OE.388022). URL: <http://www.opticsexpress.org/abstract.cfm?URI=oe-28-7-10552>.
- [103] F. Wyrowski and C. Hellmann. "The geometric Fourier transform." In: *Proc. DGO* (2017).

- [104] Zongzhao Wang, Site Zhang, Olga Baladron-Zorita, Christian Hellmann, and Frank Wyrowski. "Application of the semi-analytical Fourier transform to electromagnetic modeling." In: *Opt. Express* 27.11 (2019), pp. 15335–15350. DOI: [10.1364/OE.27.015335](https://doi.org/10.1364/OE.27.015335). URL: <http://www.opticsexpress.org/abstract.cfm?URI=oe-27-11-15335>.
- [105] Rui Shi, Norik Janunts, Rainer Heintzmann, Christian Hellmann, and Frank Wyrowski. "Fast-physical optics modeling of microscopy system with structured illumination." In: vol. 10694. 2018, pp. 10694–10694–9. DOI: [10.1117/12.2315842](https://doi.org/10.1117/12.2315842). URL: <https://doi.org/10.1117/12.2315842>.
- [106] Gaid Moulin, François Goudail, Pierre Chavel, and Dengfeng Kuang. "Heuristic models for diffraction by some simple micro-objects." In: *J. Opt. Soc. Am. A* 26.4 (2009), pp. 767–775. DOI: [10.1364/JOSAA.26.000767](https://doi.org/10.1364/JOSAA.26.000767). URL: <http://josaa.osa.org/abstract.cfm?URI=josaa-26-4-767>.
- [107] Gaurav Bose, Heikki J. Hyvärinen, Jani Tervo, and Jari Turunen. "Geometrical optics in the near field: local plane-interface approach with evanescent waves." In: *Opt. Express* 23.1 (2015), pp. 330–339. DOI: [10.1364/OE.23.000330](https://doi.org/10.1364/OE.23.000330). URL: <http://www.opticsexpress.org/abstract.cfm?URI=oe-23-1-330>.
- [108] J. A. Stratton and L. J. Chu. "Diffraction Theory of Electromagnetic Waves." In: *Phys. Rev.* 56 (1 1939), pp. 99–107. DOI: [10.1103/PhysRev.56.99](https://link.aps.org/doi/10.1103/PhysRev.56.99). URL: <https://link.aps.org/doi/10.1103/PhysRev.56.99>.
- [109] A. Couairon, O. G. Kosareva, N. A. Panov, D. E. Shipilo, V. A. Andreeva, V. Jukna, and F. Nesa. "Propagation equation for tight-focusing by a parabolic mirror." In: *Opt. Express* 23.24 (2015), pp. 31240–31252. DOI: [10.1364/OE.23.031240](https://doi.org/10.1364/OE.23.031240). URL: <http://www.opticsexpress.org/abstract.cfm?URI=oe-23-24-31240>.
- [110] C.J.R. Sheppard and Min Gu. "Imaging by a High Aperture Optical System." In: *Journal of Modern Optics* 40.8 (1993), pp. 1631–1651. DOI: [10.1080/09500349314551641](https://doi.org/10.1080/09500349314551641). eprint: <https://doi.org/10.1080/09500349314551641>. URL: <https://doi.org/10.1080/09500349314551641>.
- [111] Justin B. Judkins and Richard W. Ziolkowski. "Finite-difference time-domain modeling of nonperfectly conducting metallic thin-film gratings." In: *J. Opt. Soc. Am. A* 12.9 (1995), pp. 1974–1983. DOI: [10.1364/JOSAA.12.001974](https://doi.org/10.1364/JOSAA.12.001974). URL: <http://josaa.osa.org/abstract.cfm?URI=josaa-12-9-1974>.
- [112] A. Taflové and S. C. Hagness. *Computational Electrodynamics: The Finite-Difference Time-Domain Method*. English. 3rd. Artech House, 2005.
- [113] Kane Yee. "Numerical solution of initial boundary value problems involving maxwell's equations in isotropic media." In: *IEEE Transactions on Antennas and Propagation* 14.3 (1966), pp. 302–307. ISSN: 0018-926X. DOI: [10.1109/TAP.1966.1138693](https://doi.org/10.1109/TAP.1966.1138693).

- [114] Dennis W. Prather and Shouyuan Shi. "Formulation and application of the finite-difference time-domain method for the analysis of axially symmetric diffractive optical elements." In: *J. Opt. Soc. Am. A* 16.5 (1999), pp. 1131–1142. DOI: [10.1364/JOSAA.16.001131](https://doi.org/10.1364/JOSAA.16.001131). URL: <http://josaa.osa.org/abstract.cfm?URI=josaa-16-5-1131>.
- [115] Lumerical. FDTD Solutions: 3D/2D Maxwell's solver for nanophotonic devices <https://www.lumerical.com/tcad-products/fdtd/>.
- [116] CST. CST-Computer Simulation Technology <https://www.cst.com/>.
- [117] Peter Monk. "A finite element method for approximating the time-harmonic Maxwell equations." In: *Numerische Mathematik* 63.1 (1992), pp. 243–261. ISSN: 0945-3245. DOI: [10.1007/BF01385860](https://doi.org/10.1007/BF01385860). URL: <https://doi.org/10.1007/BF01385860>.
- [118] P. Monk, P.M. Peter Monk, P.H. Department of Mathematics Sciences Peter Monk, and Oxford University Press. *Finite Element Methods for Maxwell's Equations*. Numerical Analysis and Scienti. Clarendon Press, 2003. ISBN: 9780198508885. URL: <https://books.google.de/books?id=tLbmCwAAQBAJ>.
- [119] P. Šolín. *Partial Differential Equations and the Finite Element Method*. Pure and Applied Mathematics: A Wiley Series of Texts, Monographs and Tracts. Wiley, 2005. ISBN: 9780471764090. URL: <https://books.google.de/books?id=AgWFqIKbeBUC>.
- [120] J.M. Jin. *The Finite Element Method in Electromagnetics*. Wiley - IEEE. Wiley, 2015. ISBN: 9781118842027. URL: <https://books.google.de/books?id=DFi-BgAAQBAJ>.
- [121] Comsol <https://www.comsol.com/>.
- [122] JCMWave. JCMSUITE - SOFTWARE SOLUTIONS FOR NANOOPTICS <https://jcmwave.com/>.
- [123] P Lalanne et al. "Numerical analysis of a slit-groove diffraction problem." In: *Journal of the European Optical Society - Rapid publications* 2.0 (2007). ISSN: 1990-2573. URL: [http://www.jeos.org/index.php/jeos\\_rp/article/view/07022](http://www.jeos.org/index.php/jeos_rp/article/view/07022).
- [124] A. Dereux, C. Girard, and O. J. F. Martin. "Iterative Scheme For Computing Exactly The Total Field Propagating In Dielectric Structures Of Arbitrary Shape." In: *Journal Of The Optical Society Of America A-Optics Image Science And Vision* 11 (1994), pp. 1073–1080.
- [125] A S van de Nes, J J M Braat, and S F Pereira. "High-density optical data storage." In: *Reports on Progress in Physics* 69.8 (2006), p. 2323. URL: <http://stacks.iop.org/0034-4885/69/i=8/a=R02>.
- [126] D. Maystre. "Sur la diffraction d'une onde plane electromagnetique par un reseau metallique." In: *Optics Communications* 8.3 (1973), pp. 216–219. ISSN: 0030-4018. DOI: [https://doi.org/10.1016/0030-4018\(73\)90130-2](https://doi.org/10.1016/0030-4018(73)90130-2). URL: <http://www.sciencedirect.com/science/article/pii/0030401873901302>.
- [127] Daniel Maystre. "Photonic crystal diffraction gratings." In: *Opt. Express* 8.3 (2001), pp. 209–216. DOI: [10.1364/OE.8.000209](https://doi.org/10.1364/OE.8.000209). URL: <http://www.opticsexpress.org/abstract.cfm?URI=oe-8-3-209>.

- [128] Leonid I. Goray and Gunther Schmidt. "Solving conical diffraction grating problems with integral equations." In: *J. Opt. Soc. Am. A* 27.3 (2010), pp. 585–597. DOI: [10.1364/JOSAA.27.000585](https://doi.org/10.1364/JOSAA.27.000585). URL: <http://josaa.osa.org/abstract.cfm?URI=josaa-27-3-585>.
- [129] Gunther Schmidt. "On the Diffraction by Biperiodic Anisotropic Structures." In: *Applicable Analysis* 82.1 (2003), pp. 75–92. DOI: [10.1080/0003681031000068275](https://doi.org/10.1080/0003681031000068275). eprint: <https://doi.org/10.1080/0003681031000068275>. URL: <https://doi.org/10.1080/0003681031000068275>.
- [130] Gunther Schmidt and Bernd H. Kleemann. "Integral equation methods from grating theory to photonics: an overview and new approaches for conical diffraction." In: *Journal of Modern Optics* 58.5-6 (2011), pp. 407–423. DOI: [10.1080/09500340.2010.538734](https://doi.org/10.1080/09500340.2010.538734). eprint: <https://doi.org/10.1080/09500340.2010.538734>. URL: <https://doi.org/10.1080/09500340.2010.538734>.
- [131] PCGrate. PCGrate: by International Intellectual Group Inc, <http://pcgrate.com>.
- [132] WIAS-DiPoG. WIAS-DiPoG: Direct and Inverse Problems for Optical Gratings, <https://www.wias-berlin.de/software/DIPOG/>.
- [133] Physical optics simulation and design software "Wyrowski VirtualLab Fusion", developed by Wyrowski Photonics GmbH, distributed by **LightTrans International UG**, Jena, Germany.
- [134] GSolver: Rigorous Diffraction Grating Analysis, <http://www.gsolver.com/>.
- [135] RSoft: Powerful, accurate design solutions for photonic components, circuit and systems, <https://www.synopsys.com/optical-solutions/rsoft>.
- [136] K. Knop. "Rigorous diffraction theory for transmission phase gratings with deep rectangular grooves." In: *J. Opt. Soc. Am.* 68.9 (1978), pp. 1206–1210. DOI: [10.1364/JOSA.68.001206](https://doi.org/10.1364/JOSA.68.001206). URL: <http://www.opticsinfobase.org/abstract.cfm?URI=josa-68-9-1206>.
- [137] M. G. Moharam and T. K. Gaylord. "Rigorous coupled-wave analysis of planar-grating diffraction." In: *J. Opt. Soc. Am.* 71.7 (1981), pp. 811–818. DOI: [10.1364/JOSA.71.000811](https://doi.org/10.1364/JOSA.71.000811). URL: <http://www.opticsinfobase.org/abstract.cfm?URI=josa-71-7-811>.
- [138] M. G. Moharam and T. K. Gaylord. "Rigorous coupled-wave analysis of grating diffraction— E-mode polarization and losses." In: *J. Opt. Soc. Am.* 73.4 (1983), pp. 451–455. DOI: [10.1364/JOSA.73.000451](https://doi.org/10.1364/JOSA.73.000451). URL: <http://www.osapublishing.org/abstract.cfm?URI=josa-73-4-451>.
- [139] Elias N. Glytsis and Thomas K. Gaylord. "Three-dimensional (vector) rigorous coupled-wave analysis of anisotropic grating diffraction." In: *J. Opt. Soc. Am. A* 7.8 (1990), pp. 1399–1420. DOI: [10.1364/JOSAA.7.001399](https://doi.org/10.1364/JOSAA.7.001399). URL: <http://josaa.osa.org/abstract.cfm?URI=josaa-7-8-1399>.
- [140] Eero Noponen and Jari Turunen. "Eigenmode method for electromagnetic synthesis of diffractive elements with three-dimensional profiles." In: *J. Opt. Soc. Am. A* 11.9 (1994), pp. 2494–2502. DOI: [10.1364/JOSAA.11.002494](https://doi.org/10.1364/JOSAA.11.002494). URL: <http://josaa.osa.org/abstract.cfm?URI=josaa-11-9-2494>.



- [141] Lifeng Li. "New formulation of the Fourier modal method for crossed surface-relief gratings." In: *J. Opt. Soc. Am. A* 14.10 (1997), pp. 2758–2767. DOI: [10.1364/JOSAA.14.002758](https://doi.org/10.1364/JOSAA.14.002758). URL: <http://josaa.osa.org/abstract.cfm?URI=josaa-14-10-2758>.
- [142] Lifeng Li. "Reformulation of the fourier modal method for surface-relief gratings made with anisotropic materials." In: *Journal of Modern Optics* 45.7 (1998), pp. 1313–1334. DOI: [10.1080/09500349808230632](https://doi.org/10.1080/09500349808230632). eprint: <http://dx.doi.org/10.1080/09500349808230632>. URL: <http://dx.doi.org/10.1080/09500349808230632>.
- [143] Lifeng Li. "Fourier modal method for crossed anisotropic gratings with arbitrary permittivity and permeability tensors." In: *Journal of Optics A: Pure and Applied Optics* 5.4 (2003), p. 345. URL: <http://stacks.iop.org/1464-4258/5/i=4/a=307>.
- [144] Lifeng Li. "A Modal Analysis of Lamellar Diffraction Gratings in Conical Mountings." In: *Journal of Modern Optics* 40.4 (1993), pp. 553–573. DOI: [10.1080/09500349314550631](https://doi.org/10.1080/09500349314550631). eprint: <http://dx.doi.org/10.1080/09500349314550631>. URL: <http://dx.doi.org/10.1080/09500349314550631>.
- [145] D. M. Pai and K. A. Awada. "Analysis of dielectric gratings of arbitrary profiles and thicknesses." In: *J. Opt. Soc. Am. A* 8.5 (1991), pp. 755–762. DOI: [10.1364/JOSAA.8.000755](https://doi.org/10.1364/JOSAA.8.000755). URL: <http://josaa.osa.org/abstract.cfm?URI=josaa-8-5-755>.
- [146] Lifeng Li. "Multilayer modal method for diffraction gratings of arbitrary profile, depth, and permittivity." In: *J. Opt. Soc. Am. A* 10.12 (1993), pp. 2581–2591. DOI: [10.1364/JOSAA.10.002581](https://doi.org/10.1364/JOSAA.10.002581). URL: <http://josaa.osa.org/abstract.cfm?URI=josaa-10-12-2581>.
- [147] F. Montiel and M. Neviere. "Differential theory of gratings: extension to deep gratings of arbitrary profile and permittivity through the R-matrix propagation algorithm." In: *J. Opt. Soc. Am. A* 11.12 (1994), pp. 3241–3250. DOI: [10.1364/JOSAA.11.003241](https://doi.org/10.1364/JOSAA.11.003241). URL: <http://josaa.osa.org/abstract.cfm?URI=josaa-11-12-3241>.
- [148] D. Y. K. Ko and J. R. Sambles. "Scattering matrix method for propagation of radiation in stratified media: attenuated total reflection studies of liquid crystals." In: *J. Opt. Soc. Am. A* 5.11 (1988), pp. 1863–1866. DOI: [10.1364/JOSAA.5.001863](https://doi.org/10.1364/JOSAA.5.001863). URL: <http://josaa.osa.org/abstract.cfm?URI=josaa-5-11-1863>.
- [149] Lifeng Li. "Formulation and comparison of two recursive matrix algorithms for modeling layered diffraction gratings." In: *J. Opt. Soc. Am. A* 13.5 (1996), pp. 1024–1035. DOI: [10.1364/JOSAA.13.001024](https://doi.org/10.1364/JOSAA.13.001024). URL: <http://josaa.osa.org/abstract.cfm?URI=josaa-13-5-1024>.
- [150] Lifeng Li. "Note on the S-matrix propagation algorithm." In: *J. Opt. Soc. Am. A* 20.4 (2003), pp. 655–660. DOI: [10.1364/JOSAA.20.000655](https://doi.org/10.1364/JOSAA.20.000655). URL: <http://josaa.osa.org/abstract.cfm?URI=josaa-20-4-655>.
- [151] Lifeng Li. "Bremmer series, R-matrix propagation algorithm, and numerical modeling of diffraction gratings." In: *J. Opt. Soc. Am. A* 11.11 (1994), pp. 2829–2836. DOI: [10.1364/JOSAA.11.002829](https://doi.org/10.1364/JOSAA.11.002829). URL: <http://josaa.osa.org/abstract.cfm?URI=josaa-11-11-2829>.

- [152] M. G. Moharam, Drew A. Pommet, Eric B. Grann, and T. K. Gaylord. "Stable implementation of the rigorous coupled-wave analysis for surface-relief gratings: enhanced transmittance matrix approach." In: *J. Opt. Soc. Am. A* 12.5 (1995), pp. 1077–1086. DOI: [10.1364/JOSAA.12.001077](https://doi.org/10.1364/JOSAA.12.001077). URL: <http://josaa.osa.org/abstract.cfm?URI=josaa-12-5-1077>.
- [153] Eng Leong Tan. "Note on formulation of the enhanced scattering- (transmittance-) matrix approach." In: *J. Opt. Soc. Am. A* 19.6 (2002), pp. 1157–1161. DOI: [10.1364/JOSAA.19.001157](https://doi.org/10.1364/JOSAA.19.001157). URL: <http://josaa.osa.org/abstract.cfm?URI=josaa-19-6-1157>.
- [154] M. G. Moharam, Eric B. Grann, Drew A. Pommet, and T. K. Gaylord. "Formulation for stable and efficient implementation of the rigorous coupled-wave analysis of binary gratings." In: *J. Opt. Soc. Am. A* 12.5 (1995), pp. 1068–1076. DOI: [10.1364/JOSAA.12.001068](https://doi.org/10.1364/JOSAA.12.001068). URL: <http://josaa.osa.org/abstract.cfm?URI=josaa-12-5-1068>.
- [155] Song Peng and G. Michael Morris. "Efficient implementation of rigorous coupled-wave analysis for surface-relief gratings." In: *J. Opt. Soc. Am. A* 12.5 (1995), pp. 1087–1096. DOI: [10.1364/JOSAA.12.001087](https://doi.org/10.1364/JOSAA.12.001087). URL: <http://josaa.osa.org/abstract.cfm?URI=josaa-12-5-1087>.
- [156] G. Granet and B. Guizal. "Efficient implementation of the coupled-wave method for metallic lamellar gratings in TM polarization." In: *J. Opt. Soc. Am. A* 13.5 (1996), pp. 1019–1023. DOI: [10.1364/JOSAA.13.001019](https://doi.org/10.1364/JOSAA.13.001019). URL: <http://josaa.osa.org/abstract.cfm?URI=josaa-13-5-1019>.
- [157] Philippe Lalanne and G. Michael Morris. "Highly improved convergence of the coupled-wave method for TM polarization." In: *J. Opt. Soc. Am. A* 13.4 (1996), pp. 779–784. DOI: [10.1364/JOSAA.13.000779](https://doi.org/10.1364/JOSAA.13.000779). URL: <http://josaa.osa.org/abstract.cfm?URI=josaa-13-4-779>.
- [158] Lifeng Li. "Use of Fourier series in the analysis of discontinuous periodic structures." In: *J. Opt. Soc. Am. A* 13.9 (1996), pp. 1870–1876. DOI: [10.1364/JOSAA.13.001870](https://doi.org/10.1364/JOSAA.13.001870). URL: <http://josaa.osa.org/abstract.cfm?URI=josaa-13-9-1870>.
- [159] B. Chernov, M. Neviere, and E. Popov. "Fast Fourier factorization method applied to modal analysis of slanted lamellar diffraction gratings in conical mountings." In: *Optics Communications* 194.4 (2001), pp. 289–297. ISSN: 0030-4018. DOI: [https://doi.org/10.1016/S0030-4018\(01\)01309-8](https://doi.org/10.1016/S0030-4018(01)01309-8). URL: <http://www.sciencedirect.com/science/article/pii/S0030401801013098>.
- [160] Evgeni Popov and Michel Nevrière. "Grating theory: new equations in Fourier space leading to fast converging results for TM polarization." In: *J. Opt. Soc. Am. A* 17.10 (2000), pp. 1773–1784. DOI: [10.1364/JOSAA.17.001773](https://doi.org/10.1364/JOSAA.17.001773). URL: <http://josaa.osa.org/abstract.cfm?URI=josaa-17-10-1773>.
- [161] Philippe Lalanne and Eric Silberstein. "Fourier-modal methods applied to waveguide computational problems." In: *Opt. Lett.* 25.15 (2000), pp. 1092–1094. DOI: [10.1364/OL.25.001092](https://doi.org/10.1364/OL.25.001092). URL: <http://ol.osa.org/abstract.cfm?URI=ol-25-15-1092>.

- [162] Jean Paul Hugonin and Philippe Lalanne. "Perfectly matched layers as nonlinear coordinate transforms: a generalized formalization." In: *J. Opt. Soc. Am. A* 22.9 (2005), pp. 1844–1849. DOI: [10.1364/JOSAA.22.001844](https://doi.org/10.1364/JOSAA.22.001844). URL: <http://josaa.osa.org/abstract.cfm?URI=josaa-22-9-1844>.
- [163] Jean-Pierre Berenger. "A Perfectly Matched Layer for the Absorption of Electromagnetic Waves." In: *J. Comput. Phys.* 114.2 (Oct. 1994), pp. 185–200. ISSN: 0021-9991. DOI: [10.1006/jcph.1994.1159](https://doi.org/10.1006/jcph.1994.1159). URL: <http://dx.doi.org/10.1006/jcph.1994.1159>.
- [164] Weng Cho Chew and William H. Weedon. "A 3D perfectly matched medium from modified maxwell's equations with stretched coordinates." In: *Microwave and Optical Technology Letters* 7.13 (1994), pp. 599–604. ISSN: 1098-2760. DOI: [10.1002/mop.4650071304](https://doi.org/10.1002/mop.4650071304). URL: <http://dx.doi.org/10.1002/mop.4650071304>.
- [165] Maxim Pisarenco, Joseph Maubach, Irwan Setija, and Robert Mattheij. "Aperiodic Fourier modal method in contrast-field formulation for simulation of scattering from finite structures." In: *J. Opt. Soc. Am. A* 27.11 (2010), pp. 2423–2431. DOI: [10.1364/JOSAA.27.002423](https://doi.org/10.1364/JOSAA.27.002423). URL: <http://josaa.osa.org/abstract.cfm?URI=josaa-27-11-2423>.
- [166] Maxim Pisarenco, Joseph Maubach, Irwan Setija, and Robert Mattheij. "Modified S-matrix algorithm for the aperiodic Fourier modal method in contrast-field formulation." In: *J. Opt. Soc. Am. A* 28.7 (2011), pp. 1364–1371. DOI: [10.1364/JOSAA.28.001364](https://doi.org/10.1364/JOSAA.28.001364). URL: <http://josaa.osa.org/abstract.cfm?URI=josaa-28-7-1364>.
- [167] M. Pisarenco, J.M.L. Maubach, I.D. Setija, and R.M.M. Mattheij. "Efficient solution of Maxwells equations for geometries with repeating patterns by an exchange of discretization directions in the aperiodic Fourier modal method." In: *Journal of Computational Physics* 231.24 (2012), pp. 8209–8228. ISSN: 0021-9991. DOI: [http://dx.doi.org/10.1016/j.jcp.2012.07.049](https://doi.org/10.1016/j.jcp.2012.07.049). URL: <http://www.sciencedirect.com/science/article/pii/S0021999112004378>.
- [168] Davide Bucci, Bruno Martin, and Alain Morand. "Application of the three-dimensional aperiodic Fourier modal method using arc elements in curvilinear coordinates." In: *J. Opt. Soc. Am. A* 29.3 (2012), pp. 367–373. DOI: [10.1364/JOSAA.29.000367](https://doi.org/10.1364/JOSAA.29.000367). URL: <http://josaa.osa.org/abstract.cfm?URI=josaa-29-3-367>.
- [169] Ying Li, Haitao Liu, Hongwei Jia, Fang Bo, Guoquan Zhang, and Jingjun Xu. "Fully vectorial modeling of cylindrical microresonators with aperiodic Fourier modal method." In: *J. Opt. Soc. Am. A* 31.11 (2014), pp. 2459–2466. DOI: [10.1364/JOSAA.31.002459](https://doi.org/10.1364/JOSAA.31.002459). URL: <http://josaa.osa.org/abstract.cfm?URI=josaa-31-11-2459>.
- [170] Evgeny Popov, Michel Nevière, Boris Gralak, and Gérard Tayeb. "Staircase approximation validity for arbitrary-shaped gratings." In: *J. Opt. Soc. Am. A* 19.1 (2002), pp. 33–42. DOI: [10.1364/JOSAA.19.000033](https://doi.org/10.1364/JOSAA.19.000033). URL: <http://josaa.osa.org/abstract.cfm?URI=josaa-19-1-33>.



- [171] Thomas Schuster, Johannes Ruoff, Norbert Kerwien, Stephan Rafler, and Wolfgang Osten. "Normal vector method for convergence improvement using the RCWA for crossed gratings." In: *J. Opt. Soc. Am. A* 24.9 (2007), pp. 2880–2890. DOI: [10.1364/JOSAA.24.002880](https://doi.org/10.1364/JOSAA.24.002880). URL: <http://josaa.osa.org/abstract.cfm?URI=josaa-24-9-2880>.
- [172] Benfeng Bai and Lifeng Li. "Group-theoretic approach to enhancing the Fourier modal method for crossed gratings with square symmetry." In: *J. Opt. Soc. Am. A* 23.3 (2006), pp. 572–580. DOI: [10.1364/JOSAA.23.000572](https://doi.org/10.1364/JOSAA.23.000572). URL: <http://josaa.osa.org/abstract.cfm?URI=josaa-23-3-572>.
- [173] Benfeng Bai and Lifeng Li. "Group-theoretic approach to the enhancement of the Fourier modal method for crossed gratings: C<sub>2</sub> symmetry case." In: *J. Opt. Soc. Am. A* 22.4 (2005), pp. 654–661. DOI: [10.1364/JOSAA.22.000654](https://doi.org/10.1364/JOSAA.22.000654). URL: <http://josaa.osa.org/abstract.cfm?URI=josaa-22-4-654>.
- [174] Benfeng Bai and Lifeng Li. "Reduction of computation time for crossed-grating problems: a group-theoretic approach." In: *J. Opt. Soc. Am. A* 21.10 (2004), pp. 1886–1894. DOI: [10.1364/JOSAA.21.001886](https://doi.org/10.1364/JOSAA.21.001886). URL: <http://josaa.osa.org/abstract.cfm?URI=josaa-21-10-1886>.
- [175] J. Defrance, M. Schäferling, and T. Weiss. "Modeling of second-harmonic generation in periodic nanostructures by the Fourier modal method with matched coordinates." In: *Opt. Express* 26.11 (2018), pp. 13746–13758. DOI: [10.1364/OE.26.013746](https://doi.org/10.1364/OE.26.013746). URL: <http://www.opticsexpress.org/abstract.cfm?URI=oe-26-11-13746>.
- [176] Benfeng Bai and Jari Turunen. "Fourier modal method for the analysis of second-harmonic generation in two-dimensionally periodic structures containing anisotropic materials." In: *J. Opt. Soc. Am. B* 24.5 (2007), pp. 1105–1112. DOI: [10.1364/JOSAB.24.001105](https://doi.org/10.1364/JOSAB.24.001105). URL: <http://josab.osa.org/abstract.cfm?URI=josab-24-5-1105>.
- [177] Gérard Granet. "Reformulation of the lamellar grating problem through the concept of adaptive spatial resolution." In: *J. Opt. Soc. Am. A* 16.10 (1999), pp. 2510–2516. DOI: [10.1364/JOSAA.16.002510](https://doi.org/10.1364/JOSAA.16.002510). URL: <http://josaa.osa.org/abstract.cfm?URI=josaa-16-10-2510>.
- [178] Jens Küchenmeister. "Three-dimensional adaptive coordinate transformations for the Fourier modal method." In: *Opt. Express* 22.2 (2014), pp. 1342–1349. DOI: [10.1364/OE.22.001342](https://doi.org/10.1364/OE.22.001342). URL: <http://www.opticsexpress.org/abstract.cfm?URI=oe-22-2-1342>.
- [179] Jens Küchenmeister. "Generalization and modularization of two-dimensional adaptive coordinate transformations for the Fourier modal method." In: *Opt. Express* 22.8 (2014), pp. 9404–9412. DOI: [10.1364/OE.22.009404](https://doi.org/10.1364/OE.22.009404). URL: <http://www.opticsexpress.org/abstract.cfm?URI=oe-22-8-9404>.
- [180] Sabine Essig and Kurt Busch. "Generation of adaptive coordinates and their use in the Fourier Modal Method." In: *Opt. Express* 18.22 (2010), pp. 23258–23274. DOI: [10.1364/OE.18.023258](https://doi.org/10.1364/OE.18.023258). URL: <http://www.opticsexpress.org/abstract.cfm?URI=oe-18-22-23258>.

- [181] Thomas Weiss, Gérard Granet, Nikolay A. Gippius, Sergei G. Tikhodeev, and Harald Giessen. "Matched coordinates and adaptive spatial resolution in the Fourier modal method." In: *Opt. Express* 17.10 (2009), pp. 8051–8061. DOI: [10.1364/OE.17.008051](https://doi.org/10.1364/OE.17.008051). URL: <http://www.opticsexpress.org/abstract.cfm?URI=oe-17-10-8051>.
- [182] Site Zhang, Frank Wyrowski, and Jani Tervo. "Efficient grating simulation for general incident beam." In: vol. 8977. 2014, pp. 8977–8977–12. DOI: [10.1117/12.2039961](https://doi.org/10.1117/12.2039961). URL: <https://doi.org/10.1117/12.2039961>.
- [183] Maximilian Auer and Karl-Heinz Brenner. "Localized input fields in rigorous coupled-wave analysis." In: *J. Opt. Soc. Am. A* 31.11 (2014), pp. 2385–2393. DOI: [10.1364/JOSAA.31.002385](https://doi.org/10.1364/JOSAA.31.002385). URL: <http://josaa.osa.org/abstract.cfm?URI=josaa-31-11-2385>.
- [184] CenterSpace. CenterSpace: Save time. Easy to use. High quality. Great performance, <https://www.centerspace.net>.
- [185] Huiying Zhong, Site Zhang, Rui Shi, Christian Hellmann, and Frank Wyrowski. "Fast propagation of electromagnetic fields through graded-index media." In: *J. Opt. Soc. Am. A* 35.4 (2018), pp. 661–668. DOI: [10.1364/JOSAA.35.000661](https://doi.org/10.1364/JOSAA.35.000661). URL: <http://josaa.osa.org/abstract.cfm?URI=josaa-35-4-661>.
- [186] Huiying Zhong, Site Zhang, Olga Baladron-Zorita, Rui Shi, Christian Hellmann, and Frank Wyrowski. "k-domain method for the fast calculation of electromagnetic fields propagating in graded-index media." In: *Opt. Express* 28.8 (2020), pp. 11074–11084. DOI: [10.1364/OE.388376](https://doi.org/10.1364/OE.388376). URL: <http://www.opticsexpress.org/abstract.cfm?URI=oe-28-8-11074>.
- [187] Ronald Rook, Maxim Pisarenko, and Irwan D. Setija. "Near- to far-field transformation in the aperiodic Fourier modal method." In: *Appl. Opt.* 52.28 (2013), pp. 6962–6968. DOI: [10.1364/AO.52.006962](https://doi.org/10.1364/AO.52.006962). URL: <http://ao.osa.org/abstract.cfm?URI=ao-52-28-6962>.
- [188] Jan Pomplun, Sven Burger, Lin Zschiedrich, and Frank Schmidt. "Adaptive finite element method for simulation of optical nano structures." In: *phys. stat. sol. (b)* 244.10 (Oct. 2007), pp. 3419–3434. ISSN: 0370-1972. DOI: [10.1002/pssb.200743192](https://doi.org/10.1002/pssb.200743192). URL: <https://doi.org/10.1002/pssb.200743192>.
- [189] Sven Burger, Lin Zschiedrich, Jan Pomplun, and Frank Schmidt. "JCMsuite: An Adaptive FEM Solver for Precise Simulations in Nano-Optics." In: *Integrated Photonics and Nanophotonics Research and Applications*. Optical Society of America, 2008, ITuE4. DOI: [10.1364/IPNRA.2008.ITuE4](https://doi.org/10.1364/IPNRA.2008.ITuE4). URL: <http://www.osapublishing.org/abstract.cfm?URI=IPNRA-2008-ITuE4>.
- [190] M. Fertig and K.-H. Brenner. "Vector wave propagation method." In: *J. Opt. Soc. Am. A* 27.4 (2010), pp. 709–717. DOI: [10.1364/JOSAA.27.000709](https://doi.org/10.1364/JOSAA.27.000709). URL: <http://josaa.osa.org/abstract.cfm?URI=josaa-27-4-709>.

- [191] S. Schmidt, T. Tiess, S. Schröter, R. Hambach, M. Jäger, H. Bartelt, A. Tünnermann, and H. Gross. "Wave-optical modeling beyond the thin-element-approximation." In: *Opt. Express* 24.26 (2016), pp. 30188–30200. DOI: [10.1364/OE.24.030188](https://doi.org/10.1364/OE.24.030188). URL: <http://www.opticsexpress.org/abstract.cfm?URI=oe-24-26-30188>.
- [192] S. Schmidt, S. Thiele, A. Herkommer, A. Tünnermann, and H. Gross. "Rotationally symmetric formulation of the wave propagation method-application to the straylight analysis of diffractive lenses." In: *Opt. Lett.* 42.8 (2017), pp. 1612–1615. DOI: [10.1364/OL.42.001612](https://doi.org/10.1364/OL.42.001612). URL: <http://ol.osa.org/abstract.cfm?URI=ol-42-8-1612>.
- [193] K. Brenner. "A high-speed version of the wave propagation method applied to micro-optics." In: *2017 16th Workshop on Information Optics (WIO)*. 2017, pp. 1–3. DOI: [10.1109/WIO.2017.8038108](https://doi.org/10.1109/WIO.2017.8038108).
- [194] S. Quabis, R. Dorn, M. Eberler, O. Gloeckl, and G. Leuchs. "Focusing light to a tighter spot." In: *Optics Communications* 179.1 (2000), pp. 1–7. ISSN: 0030-4018. DOI: [https://doi.org/10.1016/S0030-4018\(99\)00729-4](https://doi.org/10.1016/S0030-4018(99)00729-4). URL: <http://www.sciencedirect.com/science/article/pii/S0030401899007294>.
- [195] P. Marchenko, S. Orlov, C. Huber, P. Banzer, S. Quabis, U. Peschel, and G. Leuchs. "Interaction of highly focused vector beams with a metal knife-edge." In: *Opt. Express* 19.8 (2011), pp. 7244–7261. DOI: [10.1364/OE.19.007244](https://doi.org/10.1364/OE.19.007244). URL: <http://www.opticsexpress.org/abstract.cfm?URI=oe-19-8-7244>.
- [196] C. Huber, S. Orlov, P. Banzer, and G. Leuchs. "Influence of the substrate material on the knife-edge based profiling of tightly focused light beams." In: *Opt. Express* 24.8 (2016), pp. 8214–8227. DOI: [10.1364/OE.24.008214](https://doi.org/10.1364/OE.24.008214). URL: <http://www.opticsexpress.org/abstract.cfm?URI=oe-24-8-8214>.
- [197] Liangxin Yang, Xiangsheng Xie, Sicong Wang, and Jianying Zhou. "Minimized spot of annular radially polarized focusing beam." In: *Opt. Lett.* 38.8 (2013), pp. 1331–1333. DOI: [10.1364/OL.38.001331](https://doi.org/10.1364/OL.38.001331). URL: <http://ol.osa.org/abstract.cfm?URI=ol-38-8-1331>.
- [198] Gilad M. Lerman and Uriel Levy. "Effect of radial polarization and apodization on spot size under tight focusing conditions." In: *Opt. Express* 16.7 (2008), pp. 4567–4581. DOI: [10.1364/OE.16.004567](https://doi.org/10.1364/OE.16.004567). URL: <http://www.opticsexpress.org/abstract.cfm?URI=oe-16-7-4567>.
- [199] Heikki J. Hyvärinen, Shakil Rehman, Jani Tervo, Jari Turunen, and Colin J. R. Sheppard. "Limitations of superoscillation filters in microscopy applications." In: *Opt. Lett.* 37.5 (2012), pp. 903–905. DOI: [10.1364/OL.37.000903](https://doi.org/10.1364/OL.37.000903). URL: <http://ol.osa.org/abstract.cfm?URI=ol-37-5-903>.
- [200] M. V. Berry and S. Popescu. "Evolution of quantum superoscillations and optical superresolution without evanescent waves." In: *Journal of Physics A: Mathematical and General* 39.22 (May 2006), pp. 6965–6977. DOI: [10.1088/0305-4470/39/22/011](https://doi.org/10.1088/0305-4470/39/22/011). URL: <https://doi.org/10.1088/0305-4470/39/22/011>.

- [201] Fu Min Huang and Nikolay I. Zheludev. "Super-Resolution without Evanescent Waves." In: *Nano Lett.* 9.3 (Mar. 2009), pp. 1249–1254. ISSN: 1530-6984. DOI: [10.1021/nl9002014](https://doi.org/10.1021/nl9002014). URL: <https://doi.org/10.1021/nl9002014>.
- [202] Greg Gbur. "Using superoscillations for superresolved imaging and subwavelength focusing." In: *Nanophotonics* 8.2 (2018), pp. 205–225. DOI: <https://doi.org/10.1515/nanoph-2018-0112>. URL: <https://www.degruyter.com/view/journals/nanoph/8/2/article-p205.xml>.
- [203] Gang Chen, Zhong-Quan Wen, and Cheng-Wei Qiu. "Superoscillation: from physics to optical applications." In: *Light: Science & Applications* 8.1 (June 2019), p. 56. ISSN: 2047-7538. URL: <https://doi.org/10.1038/s41377-019-0163-9>.
- [204] Seoungjun Lee, Lin Li, Zengbo Wang, Wei Guo, Yinzhou Yan, and Tao Wang. "Immersed transparent microsphere magnifying sub-diffraction-limited objects." In: *Appl. Opt.* 52.30 (2013), pp. 7265–7270. DOI: [10.1364/AO.52.007265](https://doi.org/10.1364/AO.52.007265). URL: <http://ao.osa.org/abstract.cfm?URI=ao-52-30-7265>.
- [205] Colin J. R. Sheppard. "Aberrations in high aperture conventional and confocal imaging systems." In: *Appl. Opt.* 27.22 (1988), pp. 4782–4786. DOI: [10.1364/AO.27.004782](https://doi.org/10.1364/AO.27.004782). URL: <http://ao.osa.org/abstract.cfm?URI=ao-27-22-4782>.
- [206] Rui Shi, Zongzhao Wang, Shih-Te Hung, Christian Hellmann, and Frank Wyrowski. "Numerical analysis of tiny-focal-spot generation by focusing linearly, circularly, and radially polarized beams through a micro/nanoparticle." In: *Opt. Express* 29.2 (2021), pp. 2332–2347. DOI: [10.1364/OE.415576](https://doi.org/10.1364/OE.415576). URL: <http://www.opticsexpress.org/abstract.cfm?URI=oe-29-2-2332>.
- [207] Hendrik Christoffel Hulst and Hendrik C van de Hulst. *Light scattering by small particles*. Courier Corporation, 1981.
- [208] Julius Adams Stratton. *Electromagnetic theory*. Vol. 33. John Wiley & Sons, 2007.
- [209] Ralf Dorn, Susanne Quabis, and Gerd Leuchs. "The focus of light linear polarization breaks the rotational symmetry of the focal spot." In: *Journal of Modern Optics* 50.12 (2003), pp. 1917–1926. DOI: [10.1080/09500340308235246](https://doi.org/10.1080/09500340308235246). eprint: <https://doi.org/10.1080/09500340308235246>. URL: <https://doi.org/10.1080/09500340308235246>.
- [210] Haifeng Wang, Luping Shi, Boris Lukyanchuk, Colin Sheppard, and Chong Tow Chong. "Creation of a needle of longitudinally polarized light in vacuum using binary optics." In: *Nature Photonics* 2.8 (2008), p. 501.
- [211] Lambert J Danner. *Six-component microscope objective*. US Patent 4,384,765. 1983.
- [212] Nicolai Hartmann, Dawid Piatkowski, Richard Ciesielski, Sebastian Mackowski, and Achim Hartschuh. "Radiation Channels Close to a Plasmonic Nanowire Visualized by Back Focal Plane Imaging." In: *ACS Nano* 7.11 (2013), pp. 10257–10262. DOI: [10.1021/nn404611q](https://doi.org/10.1021/nn404611q). eprint: <https://doi.org/10.1021/nn404611q>. URL: <https://doi.org/10.1021/nn404611q>.

- [213] Rebecca Wagner and Frank Cichos. “Fast measurement of photonic stop bands by back focal plane imaging.” In: *Phys. Rev. B* 87 (16 2013), p. 165438. DOI: [10.1103/PhysRevB.87.165438](https://doi.org/10.1103/PhysRevB.87.165438). URL: <https://link.aps.org/doi/10.1103/PhysRevB.87.165438>.
- [214] Nils Calander. “Theory and Simulation of Surface Plasmon-Coupled Directional Emission from Fluorophores at Planar Structures.” In: *Analytical Chemistry* 76.8 (2004). PMID: 15080724, pp. 2168–2173. DOI: [10.1021/ac049925d](https://doi.org/10.1021/ac049925d). eprint: <https://doi.org/10.1021/ac049925d>. URL: <https://doi.org/10.1021/ac049925d>.
- [215] Ignacy Gryczynski, Joanna Malicka, Zygmunt Gryczynski, and Joseph R. Lakowicz. “Surface Plasmon-Coupled Emission with Gold Films.” In: *J. Phys. Chem. B* 108.33 (Aug. 2004), pp. 12568–12574. ISSN: 1520-6106. DOI: [10.1021/jp040221h](https://doi.org/10.1021/jp040221h). URL: <https://doi.org/10.1021/jp040221h>.
- [216] D. G. Zhang, K. J. Moh, and X.-C. Yuan. “Surface plasmon-coupled emission from shaped PMMA films doped with fluorescence molecules.” In: *Opt. Express* 18.12 (2010), pp. 12185–12190. DOI: [10.1364/OE.18.012185](http://www.opticsexpress.org/abstract.cfm?URI=oe-18-12-12185). URL: <http://www.opticsexpress.org/abstract.cfm?URI=oe-18-12-12185>.
- [217] Palash Bharadwaj, Alexandre Bouhelier, and Lukas Novotny. “Electrical Excitation of Surface Plasmons.” In: *Phys. Rev. Lett.* 106 (22 2011), p. 226802. DOI: [10.1103/PhysRevLett.106.226802](https://link.aps.org/doi/10.1103/PhysRevLett.106.226802). URL: <https://link.aps.org/doi/10.1103/PhysRevLett.106.226802>.
- [218] Pierre Boher, Thierry Leroux, Vincent Leroux, Thibault Bignon, and Veronique Collomb-Patton. “New generation of Fourier optics viewing angle measurement systems.” In: vol. 10126. 2017, pp. 10126 –10126 –12. DOI: [10.1117/12.2256125](https://doi.org/10.1117/12.2256125). URL: <https://doi.org/10.1117/12.2256125>.
- [219] Zbigniew Sikorski and Lloyd M. Davis. “Engineering the collected field for single-molecule orientation determination.” In: *Opt. Express* 16.6 (2008), pp. 3660–3673. DOI: [10.1364/OE.16.003660](http://www.opticsexpress.org/abstract.cfm?URI=oe-16-6-3660). URL: <http://www.opticsexpress.org/abstract.cfm?URI=oe-16-6-3660>.
- [220] Adam S. Backer, Mikael P. Backlund, Matthew D. Lew, and W. E. Moerner. “Single-molecule orientation measurements with a quadrated pupil.” In: *Opt. Lett.* 38.9 (2013), pp. 1521–1523. DOI: [10.1364/OL.38.001521](http://ol.osa.org/abstract.cfm?URI=ol-38-9-1521). URL: <http://ol.osa.org/abstract.cfm?URI=ol-38-9-1521>.
- [221] Jon A. Schuller, Sinan Karaveli, Theanne Schiros, Keliang He, Shyuan Yang, Ioannis Kymissis, Jie Shan, and Rashid Zia. “Orientation of luminescent excitons in layered nanomaterials.” In: *Nature Nanotechnology* 8 (Mar. 2013), pp. 271–. URL: <https://doi.org/10.1038/nnano.2013.20>.
- [222] R. Rodriguez, C. J. Regan, A. Ruiz-Columbié, W. Agutu, A. A. Bernussi, and L. Grave de Peralta. “Study of plasmonic crystals using Fourier-plane images obtained with plasmon tomography far-field superlenses.” In: *Journal of Applied Physics* 110, 083109 (2011).



- [223] Charles J. Regan, Robier Rodriguez, Shivkumar C. Gourshetty, Luis Grave de Peralta, and Ayrton A. Bernussi. "Imaging nanoscale features with plasmon-coupled leakage radiation far-field superlenses." In: *Opt. Express* 20.19 (2012), pp. 20827–20834. DOI: [10.1364/OE.20.020827](https://doi.org/10.1364/OE.20.020827). URL: <http://www.opticsexpress.org/abstract.cfm?URI=oe-20-19-20827>.
- [224] C. J. Regan, O. Thiabgoh, L. Grave de Peralta, and A.A. Bernussi. "Probing photonic Bloch wavefunctions with plasmon-coupled leakage radiation." In: *Opt. Express* 20.8 (2012), pp. 8658–8666. DOI: [10.1364/OE.20.008658](https://doi.org/10.1364/OE.20.008658). URL: <http://www.opticsexpress.org/abstract.cfm?URI=oe-20-8-8658>.
- [225] Charles J. Regan, Daniel Dominguez, Luis Grave de Peralta, and Ayrton A. Bernussi. "Far-field optical superlenses without metal." In: *Journal of Applied Physics* 113, 183105 (2013).
- [226] Roberto Lopez-Boada, Charles J. Regan, Daniel Dominguez, Ayrton. A. Bernussi, and Luis Grave de Peralta. "Fundamentals of optical far-field subwavelength resolution based on illumination with surface waves." In: *Opt. Express* 21.10 (2013), pp. 11928–11942. DOI: [10.1364/OE.21.011928](https://doi.org/10.1364/OE.21.011928). URL: <http://www.opticsexpress.org/abstract.cfm?URI=oe-21-10-11928>.
- [227] Luis Grave de Peralta. "Metal slab superlens negative refractive index versus inclined illumination: discussion." In: *J. Opt. Soc. Am. A* 32.9 (2015), pp. 1729–1735. DOI: [10.1364/JOSAA.32.001729](https://doi.org/10.1364/JOSAA.32.001729). URL: <http://josaa.osa.org/abstract.cfm?URI=josaa-32-9-1729>.
- [228] Rui Shi, Norik Janunts, Christian Hellmann, and Frank Wyrowski. "Vectorial physical-optics modeling of Fourier microscopy systems in nanooptics." In: *J. Opt. Soc. Am. A* 37.7 (2020), pp. 1193–1205. DOI: [10.1364/JOSAA.392598](https://doi.org/10.1364/JOSAA.392598). URL: <http://josaa.osa.org/abstract.cfm?URI=josaa-37-7-1193>.
- [229] Rimantas Juškaitis. "Measuring the Real Point Spread Function of High Numerical Aperture Microscope Objective Lenses." In: *Handbook Of Biological Confocal Microscopy*. Ed. by James B. Pawley. Boston, MA: Springer US, 2006, pp. 239–250. ISBN: 978-0-387-45524-2. DOI: [10.1007/978-0-387-45524-2\\_11](https://doi.org/10.1007/978-0-387-45524-2_11). URL: [https://doi.org/10.1007/978-0-387-45524-2\\_11](https://doi.org/10.1007/978-0-387-45524-2_11).
- [230] Rui Shi, Site Zhang, Christian Hellmann, and Frank Wyrowski. "Numerical Analysis of Tightly Focused Spot for Confocal Microscopy Illumination by a Real Lens System." In: *Microscopy and Microanalysis* 25.S2 (2019), pp. 1230–1231. ISSN: 1431-9276. DOI: [10.1017/s1431927619006883](https://doi.org/10.1017/s1431927619006883). URL: <https://www.cambridge.org/core/article/numerical-analysis-of-tightly-focused-spot-for-confocal-microscopy-illumination-by-a-real-lens-system/F123458FE768118540B0C9DC0D0A1C86>.
- [231] Rainer Heintzmann and Thomas Huser. "Super-Resolution Structured Illumination Microscopy." In: *Chemical Reviews* 117.23 (2017). PMID: 29125755, pp. 13890–13908. DOI: [10.1021/acs.chemrev.7b00218](https://doi.org/10.1021/acs.chemrev.7b00218). eprint: <https://doi.org/10.1021/acs.chemrev.7b00218>. URL: <https://doi.org/10.1021/acs.chemrev.7b00218>.

- [232] Rainer Heintzmann, Thomas M. Jovin, and Christoph Cremer. "Saturated patterned excitation microscopy—a concept for optical resolution improvement." In: *J. Opt. Soc. Am. A* 19.8 (2002), pp. 1599–1609. DOI: [10.1364/JOSAA.19.001599](https://doi.org/10.1364/JOSAA.19.001599). URL: <http://josaa.osa.org/abstract.cfm?URI=josaa-19-8-1599>.
- [233] Mats G. L. Gustafsson. "Nonlinear structured-illumination microscopy: Wide-field fluorescence imaging with theoretically unlimited resolution." In: *Proceedings of the National Academy of Sciences* 102.37 (2005), pp. 13081–13086. ISSN: 0027-8424. DOI: [10.1073/pnas.0406877102](https://doi.org/10.1073/pnas.0406877102). eprint: <https://www.pnas.org/content/102/37/13081.full.pdf>. URL: <https://www.pnas.org/content/102/37/13081>.
- [234] Peter M. Carlton. "Three-dimensional structured illumination microscopy and its application to chromosome structure." In: *Chromosome Research* 16.3 (2008), p. 351. ISSN: 1573-6849. DOI: [10.1007/s10577-008-1231-9](https://doi.org/10.1007/s10577-008-1231-9). URL: <https://doi.org/10.1007/s10577-008-1231-9>.
- [235] Mats G.L. Gustafsson, Lin Shao, Peter M. Carlton, C. J. Rachel Wang, Inna N. Golubovskaya, W. Zacheus Cande, David A. Agard, and John W. Sedat. "Three-Dimensional Resolution Doubling in Wide-Field Fluorescence Microscopy by Structured Illumination." In: *Biophysical Journal* 94.12 (2008), pp. 4957–4970. ISSN: 0006-3495. DOI: <https://doi.org/10.1529/biophysj.107.120345>. URL: <http://www.sciencedirect.com/science/article/pii/S0006349508703606>.
- [236] Lin Shao, Peter Kner, E Hesper Rego, and Mats G L Gustafsson. "Super-resolution 3D microscopy of live whole cells using structured illumination." In: *Nature Methods* 8 (Oct. 2011), pp. 1044–. URL: <https://doi.org/10.1038/nmeth.1734>.
- [237] Patrick Theer, Mazahir T. Hasan, and Winfried Denk. "Two-photon imaging to a depth of 1000  $\mu\text{m}$  in living brains by use of a  $\text{TiAl}_2\text{O}_3$  regenerative amplifier." In: *Opt. Lett.* 28.12 (2003), pp. 1022–1024. DOI: [10.1364/OL.28.001022](https://doi.org/10.1364/OL.28.001022). URL: <http://ol.osa.org/abstract.cfm?URI=ol-28-12-1022>.
- [238] Demirhan Kobat, Michael E. Durst, Nozomi Nishimura, Angela W. Wong, Chris B. Schaffer, and Chris Xu. "Deep tissue multiphoton microscopy using longer wavelength excitation." In: *Opt. Express* 17.16 (2009), pp. 13354–13364. DOI: [10.1364/OE.17.013354](https://doi.org/10.1364/OE.17.013354). URL: <http://www.opticsexpress.org/abstract.cfm?URI=oe-17-16-13354>.
- [239] Fritjof Helmchen and Winfried Denk. "Deep tissue two-photon microscopy." In: *Nature Methods* 2 (Nov. 2005), pp. 932–. URL: <https://doi.org/10.1038/nmeth818>.
- [240] Dan Oron, Eran Tal, and Yaron Silberberg. "Scanningless depth-resolved microscopy." In: *Opt. Express* 13.5 (2005), pp. 1468–1476. DOI: [10.1364/OPEX.13.001468](https://doi.org/10.1364/OPEX.13.001468). URL: <http://www.opticsexpress.org/abstract.cfm?URI=oe-13-5-1468>.
- [241] Guanghao Zhu, James van Howe, Michael Durst, Warren Zipfel, and Chris Xu. "Simultaneous spatial and temporal focusing of femtosecond pulses." In: *Opt. Express* 13.6 (2005), pp. 2153–2159. DOI: [10.1364/OPEX.13.002153](https://doi.org/10.1364/OPEX.13.002153). URL: <http://www.opticsexpress.org/abstract.cfm?URI=oe-13-6-2153>.

- [242] Alipasha Vaziri and Charles V. Shank. "Ultrafast widefield optical sectioning microscopy by multifocal temporal focusing." In: *Opt. Express* 18.19 (2010), pp. 19645–19655. DOI: [10.1364/OE.18.019645](https://doi.org/10.1364/OE.18.019645). URL: <http://www.opticsexpress.org/abstract.cfm?URI=oe-18-19-19645>.
- [243] Elijah Y. S. Yew, Colin J. R. Sheppard, and Peter T. C. So. "Temporally focused wide-field two-photon microscopy: Paraxial to vectorial." In: *Opt. Express* 21.10 (2013), pp. 12951–12963. DOI: [10.1364/OE.21.012951](https://doi.org/10.1364/OE.21.012951). URL: <http://www.opticsexpress.org/abstract.cfm?URI=oe-21-10-12951>.
- [244] Jenq-Nan Yih, Yvonne Yuling Hu, Yong Da Sie, Li-Chung Cheng, Chi-Hsiang Lien, and Shean-Jen Chen. "Temporal focusing-based multiphoton excitation microscopy via digital micromirror device." In: *Opt. Lett.* 39.11 (2014), pp. 3134–3137. DOI: [10.1364/OL.39.003134](https://doi.org/10.1364/OL.39.003134). URL: <http://ol.osa.org/abstract.cfm?URI=ol-39-11-3134>.
- [245] Chia-Yuan Chang, Yvonne Yuling Hu, Chun-Yu Lin, Cheng-Han Lin, Hsin-Yu Chang, Sheng-Feng Tsai, Tzu-Wei Lin, and Shean-Jen Chen. "Fast volumetric imaging with patterned illumination via digital micro-mirror device-based temporal focusing multiphoton microscopy." In: *Biomed. Opt. Express* 7.5 (2016), pp. 1727–1736. DOI: [10.1364/BOE.7.001727](https://doi.org/10.1364/BOE.7.001727). URL: <http://www.osapublishing.org/boe/abstract.cfm?URI=boe-7-5-1727>.
- [246] Heejin Choi, Elijah Y. S. Yew, Bertan Hallacoglu, Sergio Fantini, Colin J. R. Sheppard, and Peter T. C. So. "Improvement of axial resolution and contrast in temporally focused widefield two-photon microscopy with structured light illumination." In: *Biomed. Opt. Express* 4.7 (2013), pp. 995–1005. DOI: [10.1364/BOE.4.000995](https://doi.org/10.1364/BOE.4.000995). URL: <http://www.osapublishing.org/boe/abstract.cfm?URI=boe-4-7-995>.
- [247] Keisuke Isobe, Takanori Takeda, Kyohei Mochizuki, Qiyan Song, Akira Suda, Fumihiko Kannari, Hiroyuki Kawano, Akiko Kumagai, Atsushi Miyawaki, and Katsumi Midorikawa. "Enhancement of lateral resolution and optical sectioning capability of two-photon fluorescence microscopy by combining temporal-focusing with structured illumination." In: *Biomed. Opt. Express* 4.11 (2013), pp. 2396–2410. DOI: [10.1364/BOE.4.002396](https://doi.org/10.1364/BOE.4.002396). URL: <http://www.osapublishing.org/boe/abstract.cfm?URI=boe-4-11-2396>.
- [248] Li-Chung Cheng, Chi-Hsiang Lien, Yong Da Sie, Yvonne Yuling Hu, Chun-Yu Lin, Fan-Ching Chien, Chris Xu, Chen Yuan Dong, and Shean-Jen Chen. "Nonlinear structured-illumination enhanced temporal focusing multiphoton excitation microscopy with a digital micromirror device." In: *Biomed. Opt. Express* 5.8 (2014), pp. 2526–2536. DOI: [10.1364/BOE.5.002526](https://doi.org/10.1364/BOE.5.002526). URL: <http://www.osapublishing.org/boe/abstract.cfm?URI=boe-5-8-2526>.
- [249] Ziwei Li, Jia Hou, Jinli Suo, Chang Qiao, Lingjie Kong, and Qionghai Dai. "Contrast and resolution enhanced optical sectioning in scattering tissue using line-scanning two-photon structured illumination microscopy." In: *Opt. Express* 25.25 (2017), pp. 32010–32020. DOI: [10.1364/OE.25.032010](https://doi.org/10.1364/OE.25.032010). URL: <http://www.opticsexpress.org/abstract.cfm?URI=oe-25-25-32010>.



- [250] Yunlong Meng, Wei Lin, Chenglin Li, and Shih chi Chen. "Fast two-snapshot structured illumination for temporal focusing microscopy with enhanced axial resolution." In: *Opt. Express* 25.19 (2017), pp. 23109–23121. DOI: [10.1364/OE.25.023109](https://doi.org/10.1364/OE.25.023109). URL: <http://www.opticsexpress.org/abstract.cfm?URI=oe-25-19-23109>.
- [251] Keisuke Isobe, Keisuke Toda, Qiyuan Song, Fumihiko Kannari, Hiroyuki Kawano, Atsushi Miyawaki, and Katsumi Midorikawa. "Temporal focusing microscopy combined with three-dimensional structured illumination." In: *Japanese Journal of Applied Physics* 56.5 (2017), p. 052501. DOI: [10.7567/jjap.56.052501](https://doi.org/10.7567/jjap.56.052501).
- [252] Keisuke Toda, Keisuke Isobe, Kana Namiki, Hiroyuki Kawano, Atsushi Miyawaki, and Katsumi Midorikawa. "Interferometric temporal focusing microscopy using three-photon excitation fluorescence." In: *Biomed. Opt. Express* 9.4 (2018), pp. 1510–1519. DOI: [10.1364/BOE.9.001510](https://doi.org/10.1364/BOE.9.001510). URL: <http://www.osapublishing.org/boe/abstract.cfm?URI=boe-9-4-1510>.
- [253] Qiyuan Song, Keisuke Isobe, Katsumi Midorikawa, and Fumihiko Kannari. "Resistance to optical distortions in three-dimensional interferometric temporal focusing microscopy." In: *Optics Communications* 430 (2019), pp. 486 –496. ISSN: 0030-4018. DOI: <https://doi.org/10.1016/j.optcom.2018.08.075>. URL: <http://www.sciencedirect.com/science/article/pii/S0030401818307685>.

## LIST OF FIGURES

Figure 1	Basic principle of microscopy system. . . . .	3
Figure 2	A fictitious microscopy system and its field tracing diagram. . . .	10
Figure 3	Definition of contrast and inhomogeneity. . . . .	17
Figure 4	Schematic of local plane interface approximation. . . . .	19
Figure 5	Schematic of the local coordinates of the surfaces. . . . .	20
Figure 6	Schematic of propagating through a fictitious curved surface. . .	24
Figure 7	Various types of arbitrary structures. . . . .	28
Figure 8	Illustration of TE, TM and conical cases. . . . .	30
Figure 9	Demonstration of the boundary condition. . . . .	33
Figure 10	Demonstration of S matrix. . . . .	34
Figure 11	Schematic of the arbitrary 3D structure bounded by PMLs. . . .	35
Figure 12	Reference field from FEM: first example. . . . .	40
Figure 13	Comparison of LPIA and FEM: first example. . . . .	41
Figure 14	Reference field from FEM: second example. . . . .	42
Figure 15	Comparison of LPIA and FEM: second example. . . . .	42
Figure 16	Reference field from FEM: third example. . . . .	43
Figure 17	Comparison of LPIA and FEM: third example. . . . .	43
Figure 18	Demonstration of multi-reflection and refraction: first example. .	44
Figure 19	Demonstration of multi-reflection and refraction: second example.	45
Figure 20	Demonstration of internal resonance: first example. . . . .	46
Figure 21	Demonstration of internal resonance: second example. . . . .	47
Figure 22	Comparison of LPIA+FSP with FEM: first example. . . . .	48
Figure 23	Comparison of LPIA+FSP with FEM: second example. . . . .	48
Figure 24	Comparison of LPIA+FSP with WPM for propagation through two surfaces. . . . .	49
Figure 25	Comparison of LPIA+FSP with WPM for propagation through two types of focusing lenses. . . . .	49
Figure 26	Comparison of Debye-Wolf integral with the ideal lens. . . . .	50
Figure 27	Demonstration of variously-shaped apertures. . . . .	51
Figure 28	Demonstration of focusing of cylindrical vector beams. . . . .	52
Figure 29	Demonstration of the different types of the gratings. . . . .	52
Figure 30	Comparison of FMM with FEM in 2D case. . . . .	53
Figure 31	Comparison of FMM with FEM in 3D case. . . . .	55
Figure 32	Focusing through a micro-/nano-particle by ideal lens and its field tracing diagram. . . . .	58
Figure 33	Focusing through a micro-/nano-particle by real lens and its field tracing diagram. . . . .	59
Figure 34	Focal spots by only focusing by ideal lens. . . . .	60
Figure 35	Search the tiny focal spots for focusing through spherical micro- /nano-particle. . . . .	61

Figure 36	Tiny focal spots with spherical micro-/nano-particles. . . . .	61
Figure 37	Search the tiny focal spots for focusing through disk-shaped micro-/nano-particle. . . . .	62
Figure 38	Tiny focal spots with disk-shaped micro-/nano-particles. . . . .	63
Figure 39	Search the tiny focal spots for focusing through cuboid micro-/nano-particle. . . . .	64
Figure 40	Tiny focal spots with cuboid micro-/nano-particles. . . . .	65
Figure 41	Cross section of the real lens system. . . . .	65
Figure 42	Focal spots by only focusing by the real lens. . . . .	66
Figure 43	Comparison of the focal spots obtained via simulation and experiment. . . . .	66
Figure 44	Focal spots by only focusing by misaligned real lens. . . . .	67
Figure 45	Distorted focal spots by focusing through the spherical micro-/nano-particle. . . . .	67
Figure 46	Distorted focal spots by focusing through the disk-shaped micro-/nano-particle. . . . .	68
Figure 47	Distorted focal spots by focusing through the cuboid micro-/nano-particle. . . . .	69
Figure 48	Fourier microscopy system: first application. . . . .	72
Figure 49	Fourier microscopy system: second application. . . . .	73
Figure 50	Energy density of a dipole without a lens, by ideal or real lens. . . . .	76
Figure 51	Comparison of the simulation results with the experimental results. . . . .	77
Figure 52	The images at the Fourier plane with different commercial lenses. . . . .	78
Figure 53	Profiles of the images at the Fourier plane with different commercial lenses . . . . .	79
Figure 54	The images for an illuminating molecule with orientation parallel to the PhC lines. . . . .	80
Figure 55	The images for an illuminating molecule with orientation perpendicular to the PhC lines. . . . .	81
Figure 56	The energy density at the Fourier plane only with Fourier microscope. . . . .	82
Figure 57	The energy density with the Fourier microscope combined with the spectrometer. . . . .	83
Figure 58	The energy density at the Fourier plane with the entire system. . . . .	84
Figure 59	Comparison of the simulation result with the experiment result. . . . .	85
Figure 60	Schematic of structured illumination microscopy and its field tracing diagram. . . . .	88
Figure 61	Schematic of 3D-structured illumination microscopy and its field tracing diagram. . . . .	89
Figure 62	Schematic of the microscopy system with temporal focusing and its field tracing diagram. . . . .	90
Figure 63	Polarization investigation of structured illumination microscopy. . . . .	92
Figure 64	Profiles and contrast of the polarization investigation of the structured illumination microscopy . . . . .	93

Figure 65	Diffraction effects investigation of the structured illumination microscopy. . . . .	94
Figure 66	Inclined incidence investigation of the structured illumination microscopy. . . . .	95
Figure 67	Misaligned real lens system investigation for 3D-structured illumination microscopy. . . . .	95
Figure 68	Misaligned real lens system investigation for temporal focusing of 3D-structured illumination microscopy. . . . .	96

## LIST OF TABLES

---

Table 1	Summary of the quantities in Maxwell's equations. . . . .	11
Table 2	Diffraction Efficiencies (DE) and calculation time for different types of 2D grating by different methods . . . . .	54
Table 3	Summary of the applications of field tracing techniques. . . . .	59
Table 4	Summary of the applications of field tracing techniques. SG: Spectrometer Grating . . . . .	74
Table 5	Summary of the applications of field tracing techniques. . . . .	91

## LIST OF ABBREVIATIONS

---

NA	Numerical Aperture
DIC	Differential Interference Contrast
STED	SaTurated-Emission-Depletion
PALM	PhotoActivated Localization Microscopy
STORM	STochastic Optical Reconstruction Microscopy
FDTD	Finite Difference Time Domain
FEM	Finite Element Method
MoM	Method of Moment
FMM	Fourier Modal Method
LPIA	Local Plane Interface Approximation
FT	Fourier Transform
HFT	Homeomorphic Fourier Transform
IHFT	Inverse Homeomorphic Fourier Transform
FFT	Fast Fourier Transform
IFFT	Inverse Fast Fourier Transform
VIM	Volume Integral Method
IM	Integral Method
RCWA	Rigorous Coupled Wave Analysis
PMLs	Perfectly Matched Layers
AFMM	Aperiodic Fourier Modal Method
TM	Transverse Magnetic
TE	Transverse Electric
LPWA	Local Plane Wave Approximation
WPM	wave propagation method
FSP	Free-Space Propagation
2D	two-dimensional
3D	three-dimensional
SIM	Structured Illumination Microscopy
OPEF	One-Photon Excited Fluorescence
MPEF	Multi-Photon Excited Fluorescence

TPEF	Two-Photon Excited Fluorescenc
DMD	Digital Micromirror Devicee
FWHM	Full Width at Half Maximum

## ACKNOWLEDGEMENTS

---

First of all, I would like to give great thanks to my supervisor, Prof. Frank Wyrowski. He provides me the opportunity to study in Jena, where the optical valley of Germany locates. He leads me to the fantastic world of physical-optics modeling, which I enjoy a lot. His enthusiasm, passion and creation influence me a lot both in life and research. Very importantly, his knowledgeable, logical and efficient way of doing research is always the thing that I am learning about.

I also would like to express my gratitude to my colleagues, Christian Hellmann who always gives me the efficient and direct help when it is needed; Dr. Site Zhang with whose discussion inspires me a lot; Huiying Zhong, Zongzhao Wang, Irfan Ahmad Badar, Liangxin Yang and Dominik kühn who always gives me fruitful discussion; especially, Olga Baladron-Zorita who helps me to write decent English; and of course many others, such as Michael Höschel, Dr. Hagen Schweitzer, Dr. Stefan Steiner, Hartwig Crailsheim, Dr. Yueqian Zhang, ect.

My special acknowledgment goes to Dr. Norik Janunts with who I discuss a lot. Good ideals always come naturally after our discussion.

Due to the encouragement and help from my friends, I can live happily in Germany for many years. I would like to thank them all, like Ralph Tandetzky, Ian Jackson, Eleen Hammer, Pedro Rosales, Rene Burges, Josephine Platzke, Alexander Krause, Christoph Freitag, Dr. Dingxi Li, Qi Liu, Xiaoyan Yu, Shih-Te Hung, Ping Zhou, Yichen Liu, Linghe Xiong, Di Wu, Xunyu Li, Huaiyu Chen, Liying Zhang, Zhishuai Liu and many others.

I also like to take this opportunity to thank my parents and sisters. They always give me full of love and support me spiritually and financially.

Last but not least, I would like to express my gratefulness and love to my fiancée, He Chen. She always gives me full of love and support in many years. The encouragement from her helps me to overcome lots of difficulties both in life and research.





## EHRENWÖRTLICHE ERKLÄRUNG

---

Ich erkläre hiermit ehrenwörtlich, dass ich die vorliegende Arbeit selbständig, ohne unzulässige Hilfe Dritter und ohne Benutzung anderer als der angegebenen Hilfsmittel und Literatur angefertigt habe. Die aus anderen Quellen direkt oder indirekt übernommenen Daten und Konzepte sind unter Angabe der Quelle gekennzeichnet.

Bei der Auswahl und Auswertung folgenden Materials haben mir die nachstehend aufgeführten Personen in der jeweils beschriebenen Weise unentgeltlich geholfen:

Prof. Dr. Frank Wyrowski als Betreuer dieser Arbeit.

Weitere Personen waren an der inhaltlich-materiellen Erstellung der vorliegenden Arbeit nicht beteiligt. Insbesondere habe ich hierfür nicht die entgeltliche Hilfe von Vermittlungs- bzw. Beratungsdiensten (Promotionsberater oder andere Personen) in Anspruch genommen.

Niemand hat von mir unmittelbar oder mittelbar geldwerte Leistungen für Arbeiten ergalten, die im Zusammenhang mit dem Inhalt der vorgelegten Dissertation stehen.

Die Arbeit wurde bisher weder im In- noch im Ausland in gleicher oder ähnlicher Form einer anderen Prüfungsbehörde vorgelegt.

Die geltende Promotionsordnung der Physikalisch-Astronomischen Fakultät ist mir bekannt.

Ich versichere ehrenwörtlich, dass ich nach bestem Wissen die reine Wahrheit gesagt und nichts verschwiegen habe.

*Ort, Datum*

---

Unterschrift



## PUBLICATIONS

---

### JOURNAL ARTICLES

1. **Rui Shi**, Christian Hellmann, and Frank Wyrowski. Physical-optics propagation through curved surfaces. *J. Opt. Soc. Am. A*, 36(7):1252–1260, Jul 2019.
2. **Rui Shi** and Frank Wyrowski. Comparison of aplanatic and real lens focused spots in the framework of the local plane interface approximation. *J. Opt. Soc. Am. A*, 36(10):1801–1809, Oct 2019.
3. **Rui Shi**, Norik Janunts, Christian Hellmann, and Frank Wyrowski. Vectorial physical-optics modeling of Fourier microscopy systems in nanooptics. *J. Opt. Soc. Am. A*, 37(7):1193–1205, Jul 2020.
4. **Rui Shi**, Zongzhao Wang, Shih-Te Hung, Christian Hellmann, and Frank Wyrowski. Numerical analysis of tiny-focal-spot generation by focusing linearly, circularly, and radially polarized beams through a micro/nanoparticle. *Opt. Express* 2, 9: 2332–2347, Jan 2021
5. Ran Ye, Yong-Hong Ye, Hui Feng Ma, Lingling Cao, Jun Ma, Frank Wyrowski, **Rui Shi**, and Jia-Yu Zhang. Experimental imaging properties of immersion microscale spherical lenses. *Scientific Reports*, 4:3769–, January 2014.
6. Huiying Zhong, Site Zhang, **Rui Shi**, Christian Hellmann, and Frank Wyrowski. Fast propagation of electromagnetic fields through graded-index media. *J. Opt. Soc. Am. A*, 35(4):661–668, Apr 2018.
7. Huiying Zhong, Site Zhang, Olga Baladron-Zorita, **Rui Shi**, Christian Hellmann, and Frank Wyrowski. k-domain method for the fast calculation of electromagnetic fields propagating in graded-index media. *Opt. Express*, 28(8):11074–11084, Apr 2020.

### CONFERENCE PROCEEDINGS

1. **Rui Shi**, Norik Janunts, Rainer Heintzmann, Christian Hellmann, and Frank Wyrowski. Fast-physical optics modeling of microscopy system with structured illumination. *Proc. SPIE*, volume 10694, 2018.
2. **Rui Shi**, Site Zhang, Christian Hellmann, and Frank Wyrowski. Fast-physical optics modeling of two-photon fluorescence microscopy with 3d-structured illumination. *Proc. DGaO*, 2019.

3. **Rui Shi**, Site Zhang, Christian Hellmann, and Frank Wyrowski. Numerical analysis of tightly focused spot for confocal microscopy illumination by a real lens system. *Microscopy and Microanalysis*, 25(S2):1230–1231, 2019.

#### ORAL PRESENTATION

1. **Rui Shi**, and Frank Wyrowski. Efficient connection of particle scattering and objective lens imaging *SPIE Photonics Europe*, Brussels, Belgium, 2016.
2. **Rui Shi**, Site Zhang, Christian Hellmann, and Frank Wyrowski. Numerical analysis of tightly focused spot for confocal microscopy illumination by a real lens system. *SPIE Optical Systems Design*, Frankfurt am Main, Germany, 2018.
3. **Rui Shi**, Site Zhang, Christian Hellmann, and Frank Wyrowski. Fast physical-optics modeling of advanced microscopy systems 120. *DGaO-Jahrestagung*, Darmstadt, Germany, 2019.
4. **Rui Shi**, Site Zhang, Christian Hellmann, and Frank Wyrowski. Fast Physical-Optics Modeling of Two-Photon Fluorescence Microscopy with 3D Structured Illumination *Imaging and Applied Optics-OSA*, Munich, Germany, 2019.
5. **Rui Shi**, Site Zhang, Christian Hellmann, and Frank Wyrowski. Confocal Microscopy Illumination by Real Lens Systems *Microscopy and MicroAnalysis*, Portland, USA, 2019.
6. **Rui Shi**, Christian Hellmann, and Frank Wyrowski. Connection of Field Solvers: Lenses and Microstructures *EOS Topical Meeting on Diffractive Optics*, Jena, Germany, 2019.
7. **Rui Shi**, Christian Hellmann, and Frank Wyrowski. Numerical Analysis of Tightly Focused Beams by High-NA Objective Lenses *DokDok - 8th Doctoral Conference on Optics*, Eisenach, Germany, 2019.
8. **Rui Shi**, Christian Hellmann, and Frank Wyrowski. Vectorial physical-optics modeling of microscopy systems with inclusion of micro-/nano-structures *Global Scientist Interdisciplinary Forum at SUSTech*, Shenzhen, China, 2020.